Nanoscale Electron Transport Engineering for GaN Optoelectronic Devices

DISSERTATION

Presented in Partial Fulfillment of the Requirements for the Degree Doctor of Philosophy in the Graduate School of The Ohio State University

By

Fatih Akyol

Graduate Program in Electrical and Computer Engineering

The Ohio State University

2016

Dissertation Committee:

Professor Siddharth Rajan, Advisor

Professor Steven A. Ringel

Professor Roberto C. Myers

Abstract

This dissertation investigates the use of transport and heterostructure engineering for achieving more efficient III-Nitride optoelectronic devices. III-Nitride light emitting diodes (LEDs) have found a wide range of applications for general lighting, displays and automobile headlights. However, the efficiency of these devices drops at high current operation which limits the input power density and increases the cost of the emitter. In this work, unconventional emitters for reducing efficiency droop were designed and demonstrated using plasma-assisted molecular beam epitaxy (PA-MBE) growth. Nitrogen (N) –polar Gallium Nitride (GaN) LEDs with reversed polarization for better efficiency droop performance were investigated and the first N-polar LED emitting in the green spectrum was demonstrated. Cascading multiples of identical active regions was proposed as a method to circumvent efficiency droop. Unlike conventional single active region LEDs, electrical input power in such cascaded structures is supplied by increasing voltage, enabling high power output at relatively low current operation. MBE growth of cascaded (In)GaN LEDs was demonstrated, and the first three-junction blue LED was demonstrated with forward voltage operation of 9.1 V under 10 A/cm^2. GaN tunnel homo-junctions are investigated for improved optoelectronic device functionality, and the first GaN Esaki diode was demonstrated with repeatable I-V characteristics and negative differential

resistance with a peak forward tunneling current of 350 A/cm^2. GaN tunnel junctions were then integrated with PN thermionic diodes to demonstrate highly efficient Zener-based contacts to a PN diode.

Dedication

Dedicated to my family

Acknowledgments

I would like to thank number of people who have guided, helped and supported me during the entire PhD process.

In the first place, I thank my advisor, Prof. Siddharth Rajan for hiring me and let me work in such an amazing research group at the Ohio State University. He is a true advisor. He goes in details of the work and directs the study in the most convenient path, thus enabling the work to be performed to have a meaningful contribution to the field of the study. His suggestions for the realization of novel devices have extended my vision. He is not only a great advisor but also behaves very gentle about my personal life, understanding personal issues and supports & motivates me to carry on the study.

I thank Prof. Ringel and Prof. Myers for being on the committee. I thank Prof. Prof. Roberto Myers for his valuable inputs to this dissertation and my PhD study. His suggestions increased my understanding of these devices and made this dissertation more solid. We have collaborated to do pholuminescence measurements and some other optical characterization.

I thank Dr. Thomas Kent (Myers group) and Dr. Mahisur Laskar (Myers group) for doing the optical characterization of InGaN samples and for giving input regarding the measurement setup. I thank Dr. Emre Gur (Ringel Group) for help with electroluminescence measurements of the first N-polar LED. I thank Dr. Zheng Zhang for external quantum efficiency measurement of the solar cell. I also thank Prof. Jinwoo Hwang and Jared Johnson for TEM images of the GaN homojunction tunneling devices. I thank Golam Sarwar (Myers group) for discussions about MBE growth and device physics. I thank Mark Brenner for maintenance of the MBE system. Also I thank all OSU Nanotechwest Lab staff especially Dr. John Carlin and Dr. Derek Ditmer for providing me an excellent environment for device processing.

The Rajan group is an amazing research group probably distinct from other groups by having extensive sharing of ideas regarding individuals' research questions and problems and more importantly the solid friendship among each member. I guess everybody enjoyed the time spend in this group. I would thank Dr. Sriram Krishnamoorthy for a number of things, MBE training, device designs & plans, sharing ideas about device physics and material issues. Actually most of the devices in this thesis would not exist without the development of efficient GaN tunnel junctions. He is the one who lead the TJ work during his PhD. Similarly, I thank Dr. Digbijoy Nath for MBE training, for all the technical / non-technical discussions and the growth of the N-polar green LED. I thank Pil Sung Park for setting up all the processing recipes that I used and the help with Silvaco simulations. I thank Sanyam Bajaj for his deep patience against my supply of transistors with lots of material issues. We have been always very hopeful about the next sample. I thank Yuewei Zhang for sharing his ideas about MBE growth and tunnel junctions and calculations of band-tail states in GaN tunnel junctions. I thank Ting Hsiang Hung, Edwin Lee, Zhichao Yang, Dr. Michele Esposto, Craig Polchinski, Sadia Khandaker, Gurudatt Rao, Zhanboo Xia, Choong Hee Lee and all others.

Finally, I thank my wife Busra Akyol for everything. It is not possible to write those here. I thank my parents for their support and love. This thesis is dedicated to my advisor Prof. Siddharth Rajan and my wife Busra Akyol.

Vita

February 1985 ....Born, Corum, Turkey

2008...B.S. in Electrical & Electronics Engineering, The Gaziantep University, Turkey

2009 to 2011 ....B.S. in Electrical & Electronics Engineering, of Electrical and Computer engineering, The Ohio State University

2011 to present ....Graduate Research Associate, Department of Electrical and Computer Engineering, The Ohio State University

Publications

Journal Papers

F. Akyol, S. Krishnamoorthy, Y. Zhang and S. Rajan, "Low-resistance GaN tunnel homojunctions with 150 kA/cm^ 2 current and repeatable negative differential resistance", Appl. Phys. Lett. **108**, 131103 (2016).

Y. Zhang, A. Allerman, S. Krishnamoorthy, **F. Akyol**, M. W. Moseley, A. Armstrong, S. Rajan, "Enhanced light extraction in tunnel junction enabled top emitting UV LEDs", (Submitted) ArXiv:1512.02260v1 [cond-mat.mtrl-sci] (2015).

S Bajaj, **F Akyol**, S Krishnamoorthy, T.-H. Hung, S Rajan, "Simulation of enhancement mode GaN HEMTs with threshold >5 V using p-type buffer", (Submitted) ArXiv:1511.04438v1 [physics.ins-det] (2015).

S. Bajaj, O. F Shoron, P. S. Park, S. Krishnamoorthy, **F. Akyol**, T. H. Hung, S. Reza, E. M Chumbes, J. Khurgin, S. Rajan, "Density dependent electron transport and precise of modelling GaN high electron mobility transistors ", Appl. Phys. Lett. **107**, 153504 (2015).

S. Rajan, S. Krishnamoorthy and **F. Akyol**, "GaN based interband tunnel junctions", Gallium Nitride (GaN): Physics, Devices and Technology, 47, 299 (2015)

F. Akyol, S. Krishnamoorthy, Y. Zhang, S. Rajan "GaN based three-junction cascaded light emitting diode with low-resistance InGaN tunnel junctions" Appl. Phy, Express 8, 082103 (2015).

Y. Zhang, S. Krishnamoorthy, J. M. Johnson, **F. Akyol**, A. Allerman, M. W. Moseley, A. Armstrong, J. Hwang and S. Rajan, "Interband tunneling for hole injection in III-nitride ultraviolet emitters", Appl. Phys. Lett. 106, 141103 (2015).

Y. Zhang, S. Krishnamoorthy, JM Johnson, **F. Akyol**, A. Allerman, M. W. Mosoley, A. Armstrong, J. Hwang, S. Rajan "Interband tunneling for hole injection in III-nitride ultraviolet emitters" Applied Physics Letters 106 (14), 141103 (2015).

S. Krishnamoorthy, **F. Akyol**, S. Rajan "InGaN/GaN tunnel junctions for hole injection in GaN light emitting diodes" Applied Physics Letters, 105 (14), 141104 (2014).

Fatih Akyol, Sriram Krishnamoorthy , and Siddharth Rajan, "Tunneling-based carrier regeneration in cascaded GaN light emitting diodes to overcome efficiency droop ", Applied Physics Letters,103, 081107 (2013).

Sriram Krishnamoorthy , **Fatih Akyol**, Pil Sung Park, and Siddharth Rajan, "Low Resistance GaN/InGaN/GaN tunnel junctions ", Appl. Phys. Lett. 102, 113503 (2013).

Fatih Akyol, Digbijoy N. Nath, Sriram Krishnamoorthy, Pil Sung Park and Siddharth Rajan, "Suppression of Electron Overflow and Efficiency Droop in N-polar GaN Green LEDs", Applied Physics Letters, 100, 111118 (2012).

Fatih Akyol, Digbijoy N. Nath, Emre Gur, Pil Sung Park, Siddharth Rajan, 'N-polar III-Nitride Green (540nm) Light Emitting Diode' Japanese Journal of Applied Physics, Vol. 50, 052101 (2011).

Sriram Krishnamoorthy, Digbijoy Nath, **Fatih Akyol**, Pil Sung Park, Michele Esposto, Siddharth Rajan "Polarization engineered GaN/InGaN/GaN tunnel diodes," Applied Physics Letters,97,203502 (2010).

CONFERENCE PROCEEDINGS

S. Bajaj, T.-H. Hung, **F. Akyol**, S. Krishnamoorthy, S. Khandaker, A. Armstrong, A. Allerman, S. Rajan, "Power switching transistors based on GaN and AlGaN channels", 2015 IEEE 3rd Workshop on Wide Bandgap Power Devices and Applications (WiPDA), November 2-4 (2015).

S. Bajaj, O. F. Shoron, P. –S. Park, S. Krishnamoorthy, **F. Akyol**, T.-H. Hung, S. Reza, E. M Chumbes, J. B. Khurgin, S. Rajan "Density-dependent electron transport for accurate modeling of AlGaN/GaN HEMTs" 73rd Annual Device Research Conference (DRC) (2015).

Sriram Krishnamoorthy, **Fatih Akyol**, Siddharth Rajan, "III_nitride tunnel junctions for efficient solid state lighting (Invited)", Proc. SPIE 8986, Gallium Nitride Materials and Devices IX, 89861F (March 8, 2014); doi:10.1117/12.2039382.

Siddharth Rajan, Sriram Krishnamoorthy, **Fatih Akyol**, "III-Nitride Tunnel Junctions: Devices and Applications (Invited Paper)", International Semiconductor Device Research Symposium, Dec 11-13, 2013.

Fatih Akyol, Sriram Krishnamoorthy, Siddharth Rajan, "Overcoming Nitride Light Emitting Diode Efficiency Droop by Tunneling Based Carrier Regeneration", International Semiconductor Device Research Symposium, Dec 11-13,2013

Camelia Selcu, Santino C Carnevale, Thomas F. Kent, **Fatih Akyol**, Patrick Philips, Micheal J. Mills, Siddharth Rajan, Jonathan P. Pelz, Roberto C. Myers, 'Investigation of the electronic transport in polarization-induced nanowires using conductive atomic force microscopy (AFM)' Bulletin of the American Physical Society, 58 No:1 (2013).

Sriram Krishnamoorthy , **Fatih Akyol**, Jing Yang, Pil Sung Park, Roberto Myers, Siddharth Rajan, "Record low tunnel junction specific resistivity (< 3E-4 Ohm cm2) in GaN inter-band tunnel junctions", Device Research Conference (DRC), 2012 69th Annual , June 2012

Sriram Krishnamoorthy, **Fatih Akyol**, and Siddharth Rajan, 'III-Nitride tunnel junctions for efficiency solid state lightening' (invited paper), SPIE photonics west 2014.

CONFERENCE PRESENTATIONS

Yuewei Zhang, Sriram Krishnamoorthy, **Fatih Akyol** and Siddharth Rajan, "(Invited) Tunnel Junctions for III-Nitride Ultraviolet Optoelectronics", 42nd International Symposium on Compound Semiconductors June 28-July 2, 2015 University of California, Santa Barbara, CA, 2015.

Yuewei Zhang, Sriram Krishnamoorthy, **Fatih Akyol**, Sadia Khandaker Monika, Andrew Allerman, Michael W. Moseley, Andrew Armstrong, and Siddharth Rajan, "Polarization engineered Al0.55Ga0.45N tunnel junctions for ultraviolet emitters", 11th International Conference on Nitride Semiconductors (ICNS-11), Beijing, China (August 30th - September 4th, 2015).

S. Bajaj, T.-H. Hung, **F. Akyol**, S. Krishnamoorthy, S. Khandaker, A. Armstrong, A. Allerman and S. Rajan, "(Invited) Power switching transistors based on GaN and AlGaN channels," in 3rd IEEE Workshop on Wide Bandgap Power Devices and Applications (WiPDA), 2015

S. Bajaj, O. F. Shoron, P. S. Park, S. Krishnamoorthy, **F. Akyol**, T.-H. Hung, S. Reza, E. M. Chumbes, J. Khurgin and S. Rajan, "Density-dependent electron transport for accurate modeling of AlGaN/GaN HEMTs," in 11th Topical Workshop on Heterostructure Microelectronics (TWHM), 2015

Fatih Akyol, Sriram Krishnamoorthy,Yuewei Zhang and Siddharth Rajan, "3-Junction GaN Bipolar Cascade LEDs with Low On-Resistance", 57TH Electronic Materials Conference June 24 - 26, 2015 .

Sriram Krishnamoorthy, Yuewei Zhang, , Jared M Johnson, **Fatih Akyol**, Andrew Allerman, Michael W Moseley, Andrew Armstrong, Jinwoo Hwang, Siddharth Rajan," UV Tunnel Junction LEDs" WOCSEMMAD 2015 (Workshop on Compound Semiconductor Materials and Devices) February 16-19, 2015

Sanyam Bajaj,Omor F. Shoron, **Fatih Akyol**, Sriram Krishnamoorthy, Ting-Hsiang Hung, Jacob Khurgin and Siddharth Rajan, "Field and Electron Density Dependence of 2-Dimensional Electron Gas Velocity in GaN", 57TH Electronic Materials Conference June 24 - 26, 2015

Yuewei Zhang, Sriram Krishnamoorthy,Jared M. Johnson, **Fatih Akyol**, Andrew Allerman, Michael W. Moseley, Andrew Armstrong, Jinwoo Hwang and Siddharth Rajan, "Tunneling Injection of Holes in III-Nitride Ultraviolet Emitters ", 57TH Electronic Materials Conference June 24 - 26, 2015

Yuewei Zhang, Sriram Krishnamoorthy, **Fatih Akyol** and Siddharth Rajan," Tunnel Junctions for III-Nitride Ultraviolet Optoelectronics" (Invited), 42nd International

Symposium on Compound Semiconductors June 28-July 2, 2015 University of California, Santa Barbara, CA, 2015

Yuewei Zhang, Sriram Krishnamoorthy, **Fatih Akyol**, Sadia Khandaker, Andrew Allerman, Michael W. Moseley, Andrew Armstrong, and Siddharth Rajan,"Sub 300 nm Wavelength III-Nitride Tunnel-Injected Ultraviolet LEDs", 73rd Device Research Conference (DRC), June 21-24, 2015

Sanyam Bajaj, Omor F Shoron, Pil Sung Park, Sriram Krishnamoorthy, **Fatih Akyol**, Ting-Hsiang Hung, Shahed Reza, Eduardo M Chumbes, Jacob B Khurgin and Siddharth Rajan, "Density-Dependent Electron Transport for Accurate Modeling of AlGaN/GaN HEMTs", 73rd Device Research Conference (DRC), June 21-24, 2015
Sriram Krishnamoorthy, **Fatih Akyol**, Siddharth Rajan III-nitride tunnel junctions (Invited Paper), SPIE Photonics West OPTO, San Franscisco, CA

Fatih Akyol, Sriram Krishnamoorthy and Siddharth Rajan, "Cascading Nitride light emitting diodes using low-resistance InGaN tunnel junctions", Lester Eastman Conference on High Performance Devices, Aug 5-7, 2014

Yuewei Zhang, Sriram Krishnamoorthy, **Fatih Akyol**, Siddharth Rajan, "Design of Ga-polar low resistance polarization engineered GaN/InGaN tunnel junctions", Electronic Materials Conference 2014, Santa Barbara, CA.

Siddharth Rajan, Sriram Krishnamoorthy, **Fatih Akyol**, "Tunnel Junctions for efficient III Nitride Optoelectronics (Invited Talk)", International Union of Materials Research Society, International Conference in Asia - 2013 (IUMRS-ICA 2013)
Sriram Krishnamoorthy , **Fatih Akyol**, Siddharth Rajan "III-Nitride Tunnel Junction Devices (Invited)", National Workshop on III- Nitrides Materials and Devices, Solid State Physics Lab, SSPL, New Delhi.

Sriram Krishnamoorthy, **Fatih Akyol**, and Siddharth Rajan, "Tunnel Junctions for Efficient III- nitride Optoelectronics", 17th International Workshop on The Physics of Semiconductor Devices, December 10-13, 2013, Noida, India.

Siddharth Rajan, Sriram Krishnamoorthy, **Fatih Akyol**, "III-Nitride Tunnel Junctions: Devices and Applications (Invited Paper)", International Semiconductor Device Research Symposium (ISDRS 2013).

Siddharth Rajan, Sriram Krishnamoorthy, **Fatih Akyol**, "III-Nitride Tunnel Junctions: Device Engineering and Applications (Invited)", 10th Topical Workshop on Heterostructure Microelectronics September 2-5, 2013 in Hakodate, Japan

Sriram Krishnamoorthy, **Fatih Akyol**, and Siddharth Rajan, "Incorporation of GaN/InGaN and GdN/GaN tunnel junctions in commercial III-nitride LEDs", Electronic Materials Conference 2013, South Bend, IN.

Sriram Krishnamoorthy, **Fatih Akyol**, and Siddharth Rajan, 'III-Nitride tunnel junctions for efficienct solid state lightening' (invited talk), SPIE photonics west 2014.

Siddharth Rajan, **Fatih Akyol**, Sriram Krushnamoorthy, 'III-Nitride tunnel junctions: devices and applications' International Semiconductor Research Conference (ISDRS) December, 2013.

Fatih Akyol, Sriram Krishnamoorthy, and Siddharth Rajan, 'Overcoming nitride led efficiency droop by tunneling based carrier regeneration', International Semiconductor Research Conference (ISDRS) December, 2013.

Fatih Akyol, Masihhur Laskar, Craig Pochinski, and Siddharth Rajan, 'MBE growth of N-polar InGaN under N-rich conditions' Electronic Materials Conference 2013.

Fatih Akyol, Digbijoy N. Nath, Pil Sung Park, Sriram Krishnamoorthy, and Siddharth Rajan, 'The efficiency droop characteristics of reverse polarization (N-polar) green light emitting diodes (LEDs)' Electronic Materials Conference 2012.

Sriram Krishnamoorthy , **Fatih Akyol**, Jing Yang, Pil Sung Park, Roberto Myers, Siddharth Rajan, "Record low tunnel junction specific resistivity (< 3X10^-4 Ohm cm^2) in GaN inter-band tunnel junctions ", Device Research Conference (DRC), 2012 69th Annual , June 2012

Sriram Krishnamoorthy , **Fatih Akyol**, Jing Yang, Pil Sung Park, Roberto Myers, Siddharth Rajan,"III-Nitride Interband Tunneling Devices" IEEE Lester Eastman Conference on High Performance Devices, Brown University, Aug 7-9 2012 (Talk Delivered by Prof. Rajan)

S. Krishnamoorthy , **F. Akyol**, J. Yang, P. Sung Park, R. Myers, S.Rajan,"Efficient Tunneling in Wide Bandgap III-Nitride Semiconductors", 29th North American Conference on Molecular Beam Epitaxy (NAMBE 2012), Stone Mountain Park, Georgia October 14-17, 2012

S. Krishnamoorthy, **F. Akyol**, J. Yang, P. S. Park, R. C. Myers, and S. Rajan, "III-nitride tunnel junctions: device engineering and applications " , International Workshop on Nitride Semiconductors 2012,October 14-19, 2012, Sapporo, Japan.(Invited talk delivered by Prof. Rajan)

Sriram Krishnamoorthy, Aaron Arehart, Digbijoy Nath, **Fatih Akyol**, Pil Sung Park, Michele Esposto, Steve Ringel, Siddharth Rajan, "Enhanced Inter-band tunneling by polarization engineering in InGaN/GaN quantum wells", Electronic Materials Conference 2011, UC Santa Barbara, CA

Sriram Krishnamoorthy , Digbijoy Nath, **Fatih Akyol**, Pil Sung Park, Michele Esposto, Siddharth Rajan, "Polarization-engineered GaN/InGaN/GaN tunnel junctons", Late Breaking News, International Workshop on Nitrides (IWN), Tampa, 2010.

Sriram Krishnamoorthy , Digbijoy Nath, **Fatih Akyol**, Pil Sung Park, Michele Esposto, Siddharth Rajan, "Polarization-engineered GaN/InGaN/GaN tunnel junctons", Late Breaking News, International Workshop on Nitrides (IWN), Tampa, 2010.

Digbijoy Nath, **Fatih Akyol**, Pil Sung Park, Emre Gur, Steven A. Ringel and Siddharth Rajan, "Molecular Beam Epitaxy of N-polar InGaN", 52nd Electronic Materials Conference 2010, South Bend, IN (USA).

Digbijoy Nath, **Fatih Akyol**, Pil Sung Park, Emre Gur, Steven A. Ringel and Siddharth Rajan, "N-polar InGaN based Green (540 nm) LED", Late Breaking News, 6th on Nitride Semiconductors, September 21-24, 2010, Tampa, FL (USA) International Workshop.

Digbijoy Nath, Sriram Krishnamoorthy, **Fatih Akyol**, Siddharth Rajan , "InGaN Quantum Well Devices", Workshop on Innovative Devices and Systems (WINDS), December 2010, Hawaii (USA) (Presented by S. Rajan)

Digbijoy Nath, **Fatih Akyol**, Pil Sung Park, Emre Gur, Steven A. Ringel and Siddharth Rajan, "N-polar InGaN based Green (540 nm) LED", Late Breaking News, 6th International Workshop on Nitride Semiconductors, September 21-24, 2010, Tampa, FL (USA)

Digbijoy N. Nath, **Fatih Akyol**, Emre Gur, Pil Sung Park, Steven A. Ringel, Siddharth Rajan, "Molecular Beam Epitaxy of N-polar InGaN", 52nd Electronics Materials Conference, June 21-23, 2010, South Bend, IN (USA).

Michele Esposto, Pil Sung Park, Digbijoy Nath, Sriram Krishnamoorthy, **Fatih Akyol**, Valerio De Lecce, Alessandro Chini, and Siddharth Rajan, "Design of GaN HEMTs for power switching operation", 19th European Workshop on Heterostructure Devices, October 2010, Crete, (Greece)

Fields of Study

Major Field: Electrical and Computer Engineering

Table of Contents

List of Tables

List of Figures

Chapter 1

Introduction

1.1 Fundamentals of III-Nitrides

This section briefly introduces the fundamentals of III-Nitrides such as polarization and electronic band properties.

1.1.1 Polarization in III-Nitride Crystals

III-Nitride crystals is present in nature as wurtzite or zincblende crystal structures. Wurtzite crystal structure is preferred for device applications. Figure 1.1 (a) and (b) depicts GaN crystal structures of zincblende and wurtzite, respectively. The direction of the dipole moment is from nitrogen (yellow sites) to gallium (grey sites) atom sites. In a GaN zincblende structure, the total dipole moment is zero for each unitcell, whereas the lack of inversion symmetry in wurtzite crystal results in a finite dipole moment. This results in highest dipole in [0001] or [000-1] direction under no strain of the crystal lattice which is called as spontaneous polarization. Ga- [0001] and N-face [000-1] crystals together with the direction of SP are depicted in Fig.1.2 (a) and (b), respectively.

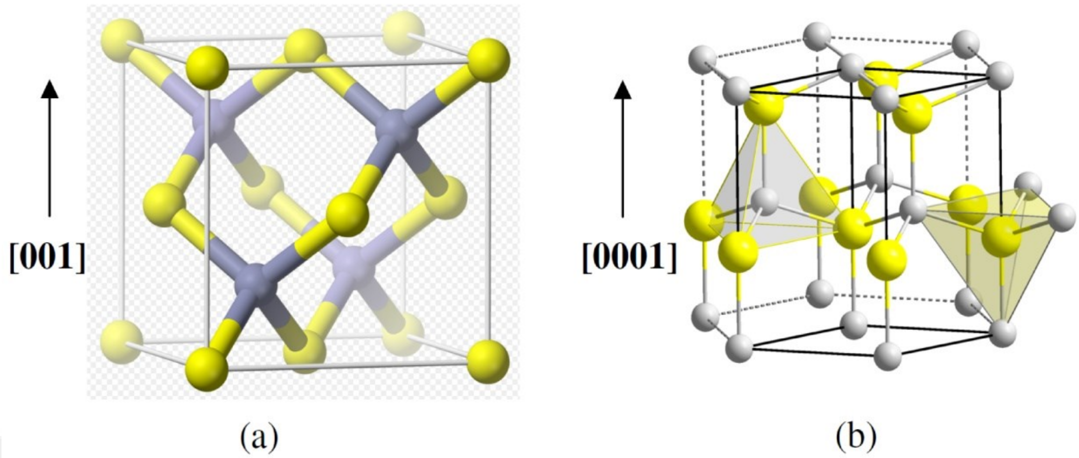

Figure 1.1 GaN crystals in (a) zincbelnde and (b) wurtzite structure. Figure courtesy: www.en.wikipedia.org/wiki

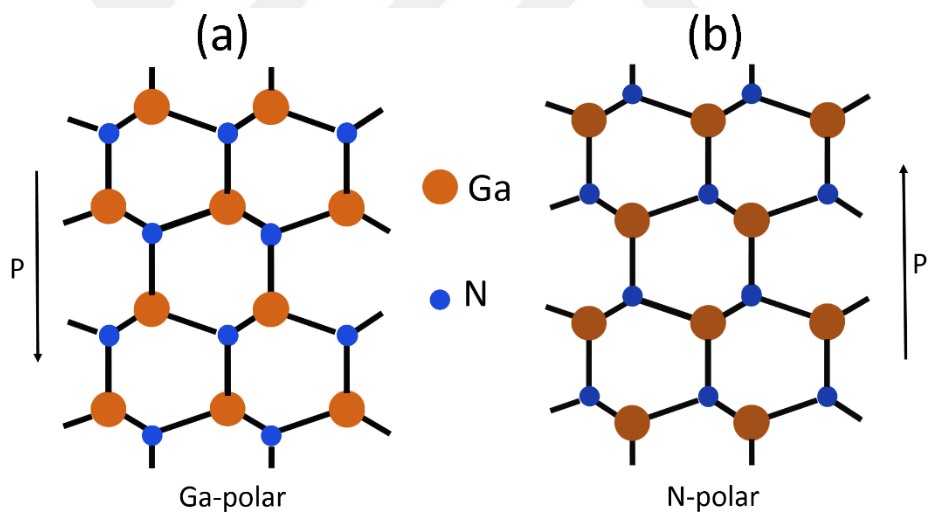

Figure 1.2 (a) Ga-polar and (b)N-polar wurtzite GaN crystal and the direction of spontaneous polarization for each.

The lattice parameters and polarization constants of III-nitrides are shown in Table 1.1 [1,2]. The piezoelectric polarization (PZ) induces by strain in the epitaxial layers. The value of PZ along [0001] axis p_{pe} can be calculated using the following relation.

$$p_{pe} = e_{33}\frac{c-c_0}{c_0} + e_{31}\frac{a-a_0}{a_0}, \qquad 1.1$$

where a_0 and c_0 is the lattice parameters of a strained layer, e_{33} and e_{31} are PZ polarization constants given in Table 1.1. Using the Eqn. 1.1, it can be found out that a compressive strain results in PZ polarization in the opposite direction of SP whereas; a tensile strain induces PZ in the direction of SP. Since lattice mismatch between InN and GaN is quite high (~11 %), PZ is dominant in InGaN crystals. On the other hand, SP is dominant in Al rich AlGaN samples, since the lattice mismatch is relatively low (~2.5%). Polarization charges cancel each in a bulk material but at the boundary of a layer, a sheet charge remains which induce electric field in the crystal without any external effects such as built-in bias or light illumination. Electric field generated under net polarization p is given by

$$E = -\frac{p}{\epsilon_r(x)\epsilon_0}, \qquad 1.2$$

where $\epsilon_r\ (x)$ represents the relative dielectric constant of the alloy. It has been reported that polarization induced electric fields can be as high as 15 MV/cm in nitrides, thus can have drastic effects on device operations [3].

		GaN	**InN**	**AlN**
Lattice Constants	a (A)	3.189	3.534	3.111
	c (A)	5.185	5.718	4.978
Polarization parameters	p_{sp}(C/m2)	-0.029	-0.032	-0.081
	e_{31}(C/m2)	-0.49	-0.57	-0.6
	e_{33}(C/m2)	0.73	0.97	1.46

Table 1.1 Lattice constants and polarization parameters of GaN, InN and AlN.

1.1.2 Electronic Band Properties

III-Nitride material system has a direct band gap throughout the alloy range, thus has a potential to show exceptional optoelectronic properties. The recombination of electrons and holes or an absorption of a photon occurs in shorter time for direct band semiconductors compared to indirect band materials, such as Silicon. Figure 1.3 depicts band gap versus lattice constant values for various semiconductor materials. It can be seen that III-nitrides alloys can be tuned in a wide energy range from ~0.7 to 6.2 eV covering the spectrum from infra-red to deep UV, which takes further attention for III-nitrides and makes them candidate for optoelectronic applications such as LEDs and solar cells.

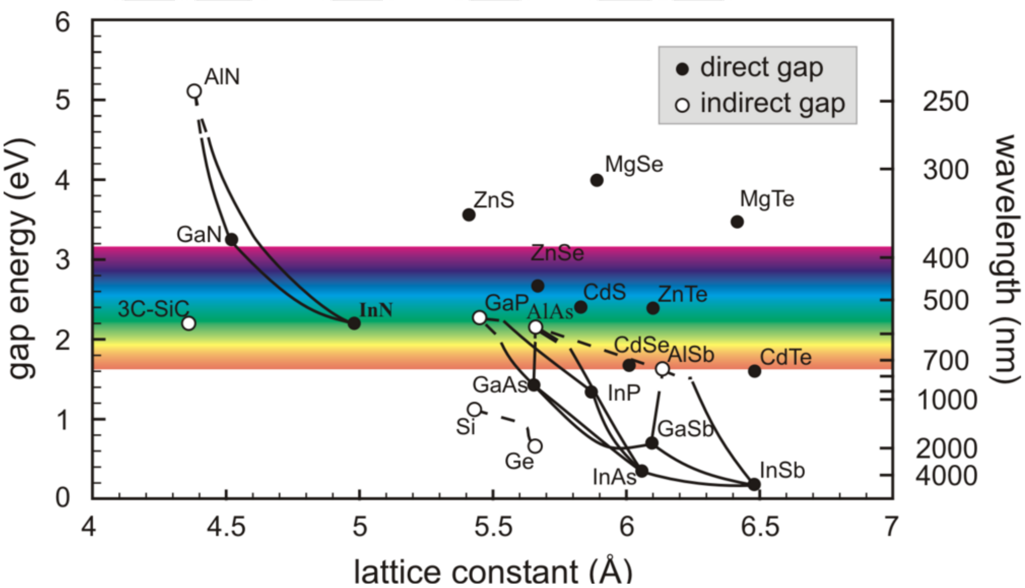

Figure 1.3 Band gap and lattice constant of various material systems. Reprinted with permission from Elsevier, after [4].

The presence of high spontaneous and piezoelectric polarization affects the energy band diagram of polar quantum-well (QW) structures dramatically. A schematic band diagram of an InGaN/GaN QW is shown in Fig. 1.4 without (a) and with (b) polarization charges [5]. It can be seen in Fig 1.4a that electron and hole wave functions fully overlap in a rectangular well whereas they get spatially separated in a triangular well (Fig. 1.4b). There are several effects of a triangular-well especially on LED operations. Firstly, electrons and holes get spatially separated across the QW which decreases the wave-function overlap, thus decreasing the spontaneous emission rate. Secondly, under low current regime where the polarization charges are not screened by the injected electron hole pairs yet, it is observed that the emission energy reduces under strong polarization field depicted in Figure 1.4 (where $E_1>E_2$). This is calledthe quantum confined Stark effect (QCSE). This causes instability in the peak emission wavelength which is not desired in an LED. To reduce and eliminate such problems caused by polarization field, crystal growths along semi- and non-polar planes has been widely investigated.

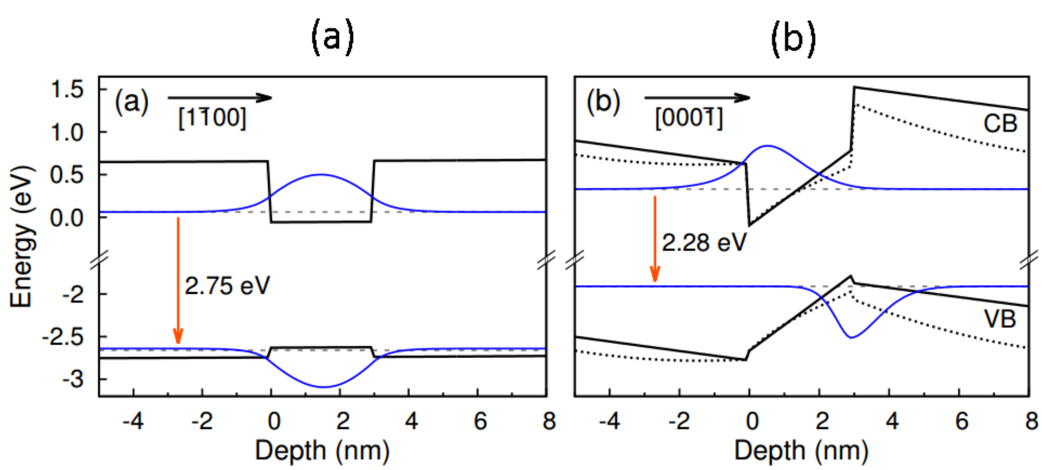

Figure 1.4 Schematics of energy band diagram of a GaN/InGaN/GaN junction (a) without polarization and (b) with polarization charge. After [5].

1.2 GaN Light Emitting Diodes (LEDs)

1.2.1 Development of GaN and III-Nitride LEDs

The first single crystal GaN sample was grown by Maruska and Tietjen using hydride vapor phase epitaxy (HVPE) in 1969 [6]. Using that sample, intrinsic properties such as the direct band gap of 3.39 eV and the n-type conduction in the undoped crystal were determined. In the following years, there were only few reports of light emission from GaN crystal. The first LED was fabricated by Pankove and co-workers using an undoped n-type GaN crystal and an insulating Zn-doped layer with an indium metal contact forming a metal-insulator-semiconductor (MIS) type LED with an emission in the green region in 1971 [7]. In the following year, Maruska reported violet emission (430 nm) via tunneling of electrons through a triangular-potential-well from a Mg-doped GaN crystal which was also an inefficient way of electron to photon conversion [8]. Those poor efficiency devices are far from commercial applications due to two reasons; (1) highly defective GaN substrates with cracks and (2) lack of having p-type conductivity. The first breakthrough in the growth of GaN came in 1986 [9]. H. Amano and I. Akasaki nucleated AlN layer on sapphire substrate before the growth of GaN layer using metal organic chemical vapor deposition system (MOCVD). This growth enabled high structural quality, crack free GaN layer. However, the single flow MOCVD reactor produced nonuniform GaN layer with poor reproducibility. In 1991, S. Nakamura has used a two-step-flow MOCVD system to produce even higher structural quality, reproducible and reliable GaN layers [10]. The main idea behind his invention was the availability of higher gas flow rate with improved thermal boundary between substrate and the gas flow. In the same year, Nakamura investigated GaN buffer layers using his reactor and obtained higher electron mobility in GaN layer compared to GaN layers grown after AlN nucleation. Meanwhile, in 1990, Akasaki et al.

found out that electron beam irradiation of MOCVD grown Mg-doped GaN layer resulted in p-type conductivity. They have then reported a p-n junction GaN LED with violet and UV emission patterns in 1991 [11]. In 1992, Nakamura found that Hydrogen was responsible for passivation of Mg atoms and holes can be obtained upon thermal annealing in an H_2 free environment [12]. This method make it more efficient, practical and uniform for activation of Mg acceptors. After this discovery, the major roadblocks for high power LEDs were overcome. In the following year, Nakamura fabricated GaN/InGaN/GaN double heterostructure (DH) LED which confines electron and holes in the InGaN layer which enables high carrier density with high radiative recombination rate [13]. As expected, he observed single peak violet and blue emission by changing the In atomic composition in the InGaN layer. In 1994, he has reported high brightness 2.5 mW blue LED [14] which has encouraged Nichia to commercialize nitride white LEDs in 1996 using InGaN DH blue LEDs. Since then, the efficiency of Nitride LEDs and laser diodes (LD) has been improved every year. In 2014, S. Nakamura, H. Amano and I. Akasaki shared the Nobel Prize in Physics for being the inventors of such environmental friendly and efficient nitride emitters.

1.2.2 LEDs: State-of-the-Art

Nitride LEDs and LDs are now commercially available for violet, blue, green and white light emission. They are used in applications such as display panels, backlighting, TV and computer screens, traffic lights, blue-ray discs, laser pointers, and white bulbs. White LED bulbs are usually obtained by using efficient blue LED integrated with a yellow phosphorous coating which converts some of the blue light to yellow, thus integration of broad yellow band luminescence with blue spectrum resulting white light. Especially regarding the commercial lighting, the market currently is around 40 billion dollars and it is forecasted that LED lighting will dominate the market by more than ~50% in 2019 [15].

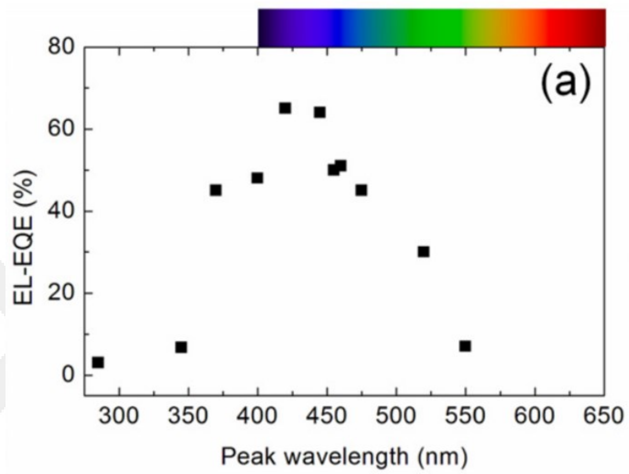

Figure 1.5 Reported EQE of Nitride emitters measured at 350 mA (35 A/cm^2). Reprinted with permission IOP Science after [16].

Since GaN lacks native substrates, it is still widely grown on sapphire/Si substrates which results in threading dislocation (TD) densities ~10^{-8}-10^{-10} cm^{-3} range due to the lattice mismatch with the foreign substrates (Si, Sapphire) [15]. Indeed such high level of TD density kills LEDs in GaAs material system [17]. Fig. 1.5 depicts the external quantum efficiency of InGaN emitters at 350 mA [16]. It can be seen that LEDs have highest EQE in 420-450 nm range over 60%. However, the EQE decreases as wavelength getting away from this range. The main reasons behind the decrease of EQE at longer wavelength range are; (1) high lattice mismatch between InGaN and GaN nucleates dislocations [18], (2) higher polarization field with increasing In atomic composition increases non-radiative recombination process [19]. On the other hand, the mechanisms for reduction of EQE in shorter wavelength are (1) decreasing In-alloy fluctuation [20] as lattice mismatch reduces which delocalize carriers from highly confined In-rich regions [20] (which increases the chance of finding non-radiative recombination centers) and (2) decreasing carrier confinement due to lower energy offset in conduction (ΔE_c) and valance (ΔE_v) band.

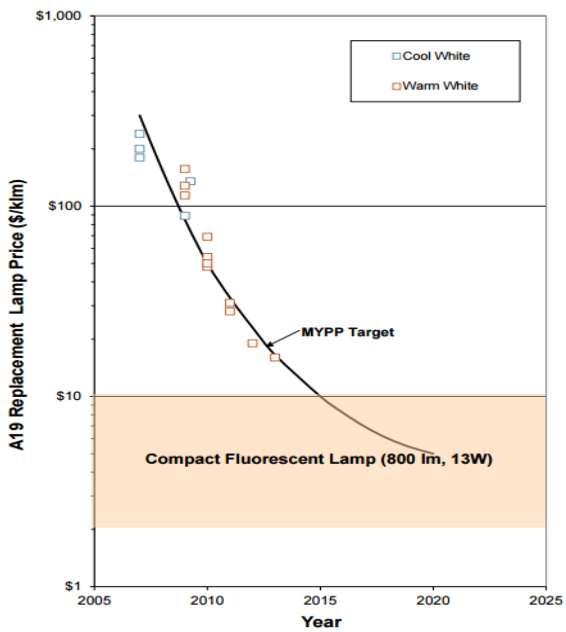

Figure 1.6. LED package price and efficacy evolution and future projection Compact florescent data shown for comparison. (Figure courtesy [15])

Figure 1.7 Schematic of an LED bulb. Image courtesy [21].

1.2.3 Challenges in Nitride LED lighting applications

Fig. 1.6 shows LED package price and efficacy evolution from 2007 and future prospections [15]. It can be seen that white LED bulbs are still quite expensive compared to compact florescent lamps. The price of a dimmable cheapest LED (A19) was reported to be around 16 $/1000 lumens, on the other hand non-dimmable compact florescent lamp price is ~ 2 $/1000 lumens. This obviously shows that it is quite challenging to compete with compact florescent in the market (especially before 2011, the beginning of this PhD study). However, lifespan should also be mentioned at this point. The LED bulbs can last for ~15 years, whereas a compact fluorescent bulb lasts ~3 years [15] which makes LEDs more attractive as long term lighting source.

The main components of an LED module are depicted in Fig. 1.7. The major component are (1) LED driver, (2) thermal management components, and (3) LED array. An LED array composed of ~10 individually packaged LEDs. LEDs are capable of operating at higher current density for high brightness which can potentially reduce the number of the LEDs in the array. The major reason for keeping LEDs at low current is the drop of efficiency which is discussed in the next section.

1.2.4 Nitride LED Efficiency Droop

Nitride LEDs have been observed to show efficiency droop under higher injection current density (> ~ 0.5 – 5 A/cm^2) (Fig. 1.8), called 'efficiency droop' [22-24]. Efficiency droop is higher for longer wavelength emitters such as green emission. While the reason for this remains a topic of active research, various groups have identified it to be due to Auger recombination processes, overflow electron current, and inefficient carrier injection and transport mechanisms.[25-31] The effects of electron overflow current on droop characteristics were investigated using multiple-quantum-well (MQW) active regions, $Al_xGa_{1-x}N$ and lattice matched InAlN electron blocking layers (EBLs), and non-polar LEDs.[23,31-34] While these were shown to improve the efficiency, the use of MQWs and EBLs also degrades the carrier injection and transport mechanisms. [28,29,34]

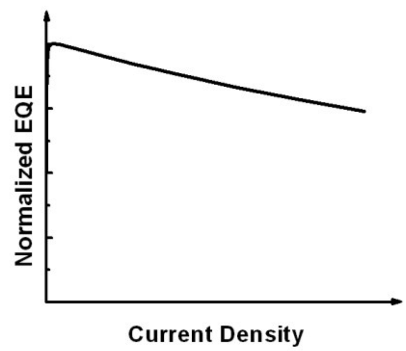

Figure 1.8: A typical external quantum efficiency (EQE) variation with current density in a commercial LED.

As it is mentioned in the previous section, efficiency droop might be an inherent problem (in spite of various designs configurations, it still exists). The commercial LED bulbs are designed with LED arrays to overcome this problem. For example, for 1000 lm of output, 10 individual LED packages are typically used, each giving 100 lm. A typical commercial LED operates around 100 lm/W of efficacy [15] which means that each LED chips need an input power ~1 W for 100 lm output. Assuming that it operates at 3 V of forward voltage, it requires ~0.33 A of input current. Since a commercial LED approximately operates at 35 A/cm^2 of current density [11], the device area is to be ~ 0.01 cm^2. Overall, 10 individual LED chips are required each has 0.01 cm^2 semiconductor area to get 1000 lm. This is one of the major cost component of LED bulbs. It is desired to achieve high output power from a small semiconductor area such as 0.001 cm^2 of a single semiconductor chip operating near 100 lm/W for an output of 1000 lm. This type of operation would reduce the cost of an LED bulb.

1.3 Thesis Overview

This thesis organized as follows: in chapter 2, the promises of N-polar LEDs (opposite polarization charge) are discussed. The first N-polar green LED demonstrated using plasma assisted molecular beam epitaxy (MBE) growth. Next, N-polar InGaN growth under N-rich conditions is investigated and optimum growth conditions are found out for the best optical output. Using InGaN quantum wells grown under N-rich conditions, single and double quantum well LEDs are fabricated and intrinsic electron blocking and enhanced efficiency droop characteristics of N-polar LEDs are analyzed.

In chapter 3, another approach to deal with efficiency droop, cascading multiple active regions via tunnel junctions, is investigated on Ga-polar LEDs. The benefits of operating LEDs with increasing voltage rather than injection current are discussed to circumvent efficiency droop in any nitride LED. Next, the growth of LEDs with multiple active regions were developed by optimizing p-GaN layer emitting layers. Finally, the first three junction LED in Nitrides is demonstrated using low-resistance InGaN/GaN polarization engineered tunnel junctions (TJs).

GaN homo-TJs are investigated in chapter 4. Utilizing heavy Si and Mg doping, the first III-Nitride backward (Esaki) diodes were reported with repeatable negative differential resistance. Both forward and reverse characteristics were investigated under varying doping concentration. Both forward and reverse current is found to increase with higher doping across the tunnel junction. Next GaN TJ is combined with a PIN diode for further analysis of the reverse bias characteristics of the TJ. The diode is operated up to 150 kA/cm^2 at 7.6 V which demonstrates the operation of highly conductive GaN tunnel homojunctions. Next, these TJs are incorporated with LED to realize p-down LEDs to enable LEDs with reverse polarization. The issues with these devices are discussed in the last part.

In chapter 5, simulation and experimental work on InGaN solar cells is reported. The simulation of 2.3 eV InGaN homojunction PIN solar cell is shown. The optimization of the device design under varying minority carrier lifetime and mobility is discussed and shown that efficiency can be enhanced as much as 36% over the PN junction design by optimizing the intrinsic layer thickness of PIN design. Due to technological limitations, these devices are not feasible for experimental demonstration. In the experimental part, an InGaN/GaN PIN solar cell is demonstrated with a TJ on the top of the device to convert resistive p- to n-type layer thus enables thin window layer. Next a dual junction solar cell fabricated and the issues with the device is discussed.

In the last chapter, future work is discussed to extend the work discussed in this thesis.

Chapter 2

N-polar InGaN Growth and Light Emitting Diodes

2.1 N-polar Green (540 nm) Light Emitting Diode with InGaN grown under In-rich conditions

2.1.1 Introduction

In the introduction chapter, the problems of the state of the state of the art LEDs were mentioned. One of the major problems is the lower peak efficiency of green emitters compared to blue LEDs. This indicates that there is significant growth and device design challenges for green and longer wavelength Nitride emitters.[35] Firstly, higher In content InGaN requires lower growth temperatures than the optimal growth temperature of GaN due to the higher volatility of In species. This mismatch in optimal growth temperatures leads to challenges in the growth of high quality InGaN/GaN multi quantum well emitters. Secondly, polarization effects are more pronounced as the In composition is increased (which is required for longer wavelength emission), It is expected that the relatively high polarization fields in c-plane oriented InGaN/GaN emitters could lead to poor carrier confinement and consequently poor efficiency in LED structures.

The N-polar orientation of GaN has several advantages that make it attractive for high In composition InGaN growth. Fristly, N-polar InN can be grown by PAMBE at higher temperatures (approximately 100^0C higher) than In-polar InN, [36,37] This is attributed to the higher stability of InN on the N-polar surface. Recent work on N-polar InGaN growth demonstrated significantly higher growth temperatures and In incorporation on N-polar InGaN when compared to Ga-polar InGaN. [38] The direction of the spontaneous and piezoelectric polarization in N-polar is in opposite direction compared to Ga-polar crystal. In this work, we examine the polarization field in reverse direction which may provide advantages for LED operations. Prior to this work, there has been no reports of electrical characterization or demonstration of N-polar green LEDs. In addition, polarization plays a critical role in device operation of all polar emitters, and investigation of N-polar InGaN-based heterostructure devices provides a route to investigate these effects. Since the polarization field increases with In composition, these effects are more pronounced as longer emission wavelengths are targeted.

Although N-polar electronic devices with performance comparable to Ga-polar ones have been reported, [39] there are relatively fewer reports on N-polar InGaN growth for optoelectronic applications, [40-42] In this letter, we report on the growth and optical characterization of N-polar InGaN based multiple quantum well (MQW) LED grown by PAMBE.

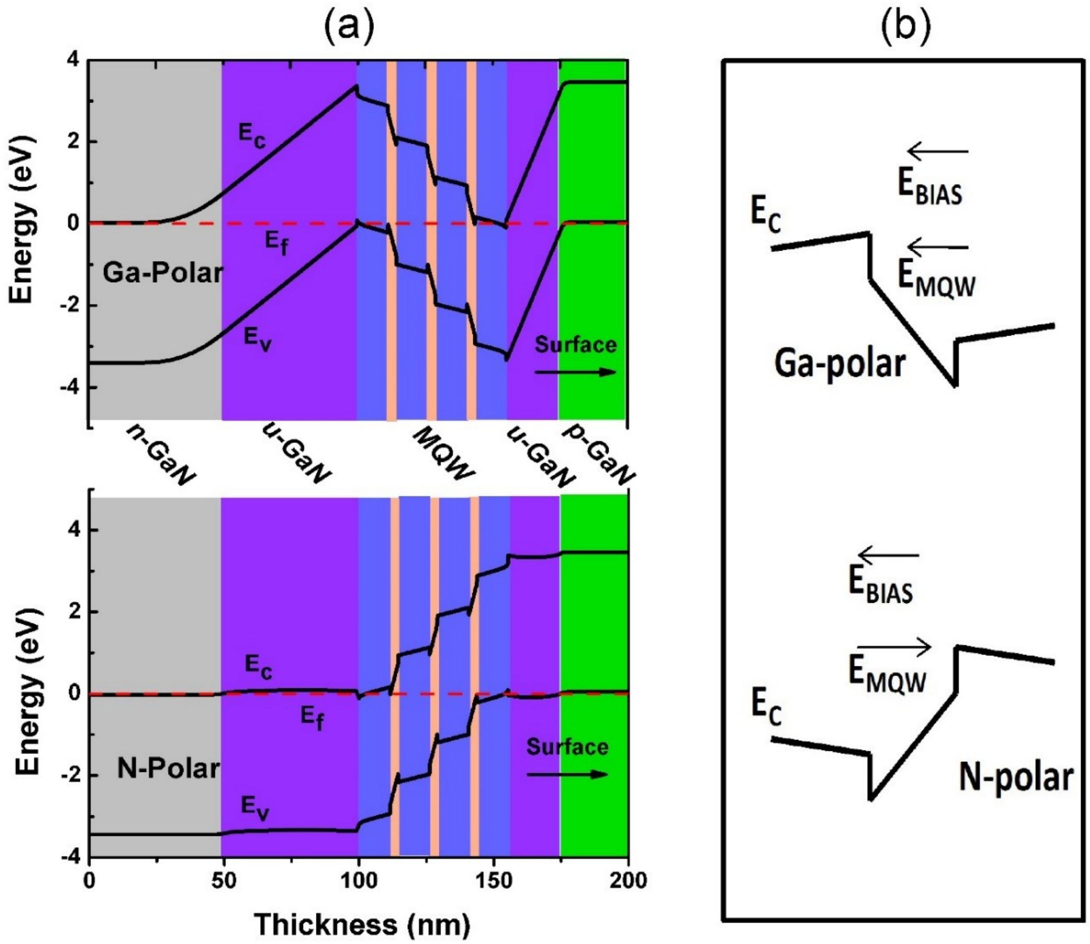

Figure 2.1: (a) Zero bias energy band diagrams of Ga- and N-polar LEDs. (b) Direction of polarization field and the electric field applied under forward bias in a Ga- and N-polar GaN/InGaN/GaN quantum well.

Zero-bias energy band diagrams of N-polar and Ga-polar typical InGaN/GaN MQW heterostructures are shown in Fig.2.1a. The energy band diagrams were calculated using a self-consistent Schrodinger-Poisson solver that incorporates spontaneous and piezoelectric polarization. [43] In the Ga-polar LED structure, the polarization fields are reversed with respect to the p-n junction depletion field, thus leading to a *wider* depletion region, however in the case of the N-polar structure, the polarization acts in the same direction as the depletion, and the depletion region is therefore reduced. This is expected to lead to a lower turn-on voltage for the N-polar p-n junction. It can be seen from Fig. 2.1b that due to the reverse direction of polarization in N-polar device, an increase in forward bias voltage assists the field in quantum well regions to approach flat-band conditions leading to suffering less from stark effect across the quantum-well. However, in a Ga-polar device structure, increasing forward bias voltage increases the field in the quantum-wells, thus decreasing the electron and hole wave-function overlap in the quantum wells. The direction of polarization in N-polar GaN therefore are more favorable to LED operation than in the case of Ga-polar GaN. It is also observed from the same figure that the injected carriers come across a potential barrier for Ga-polar structure which decreases the carrier injection efficiency and shows itself as higher turn-on voltages. Conversely, in the reversed polarization the potential barrier against the injection is eliminated which is obviously favorable to obtain lower turn-on voltages.

2.1.3 Experimental Approach for the Realization of N-polar Green LED

The sample was grown on a N-polar free standing LED quality GaN substrate (dislocation density ~ 10^8 cm^{-2}) obtained from Lumilog. Radio-frequency plasma assisted molecular beam epitaxy in a Veeco Gen 930 system equipped with standard Knudsen cells for Ga, In Mg and Si was used to grow the epitaxial stack shown in Fig. 2.2. [44] Active nitrogen was supplied using a Veeco RF plasma source. Following the growth model for N-polar InGaN growth by PAMBE, [38] a Ga-flux was chosen to achieve 29 % In mole fraction at a growth temperature of 600^0C. The growth of the active MQW region was performed in an N_2-limited and In rich growth regime with excess In coverage on the surface.

Figure 2.2 The epitaxial stack of the N-polar green LED.

The nominal growth rate defined by the N_2-stoichiometric flux in the absence of InGaN decomposition is 5 nm/min. However as predicted by the growth model, for the In composition and growth temperature used for this growth, a reduced growth rate of 3.25 nm/min was calculated accounting for decomposition to grow 3 nm of $In_{0.29}Ga_{0.71}N$ quantum well and 12 nm $In_{0.14}Ga_{0.86}N$ barrier, the compositions being verified by XRD scan data with simulation (Fig. 2.3a). The growth of InGaN QW and a GaN (or InGaN) barrier without growth interruption with a single Ga effusion cell in PAMBE poses severe challenges because the growth temperature as well as the Ga flux required for the growth of QW and barrier are significantly (~3 X) different. An N_2-pulsing scheme was hence employed to grow the barrier where In and Ga shutters were kept open throughout with the Ga-flux at the same value as used for preceding quantum well layer growth. The duty cycle of the pulse was adjusted to get InGaN with a higher Ga mole fraction. To investigate the surface morphology of the QW layer, a test sample was grown in identical conditions with the growth intentionally terminated with a ~ 2 nm $In_{0.05}Ga_{0.95}N$ (to prevent decomposition) on a single 3 nm $In_{0.29}Ga_{0.71}N$ QW layer. The atomic force microscopy (AFM) image shows smooth surface morphology (Fig 2.3b).

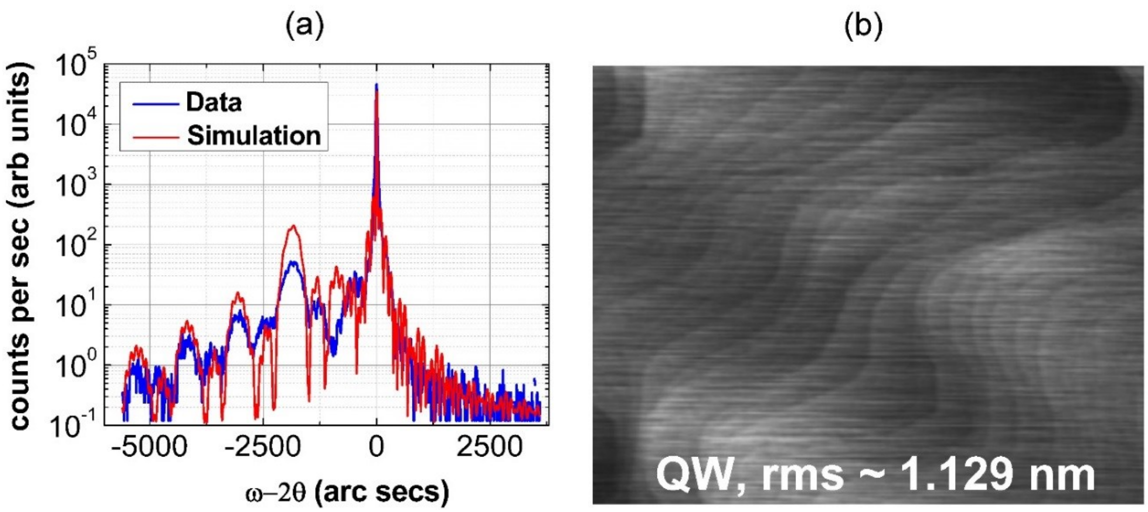

Figure 2.3 (a) The HR-XRD measurement and data fit confirming the epitaxial design. (b) 2 x 2 μm^2 AFM scan of the control sample which was terminated after the first quantum well capped with ~ 2 nm $In_{0.05}Ga_{0.95}N$ layer to prevent decomposition of InGaN.

LEDs were fabricated using conventional optical lithography. Ni / Au / Ni (5 / 5 / 1 nm) metal stack was evaporated to form the p-type electrode. Following the p contact evaporation, mesa isolation of the devices was performed by Cl–based ICP RIE etching with Cl_2 / BCl_3 / Ar (50 / 5 / 5 sccm) plasma under 40 W ICP power and 3 W RF power for

30 minutes. Finally, Ti / Au (20 / 100 nm) n-contact was deposited on the etched n-GaN layer. All measurements reported were performed on a 17,000 μm^2 device at room temperature under continuous wave operation.

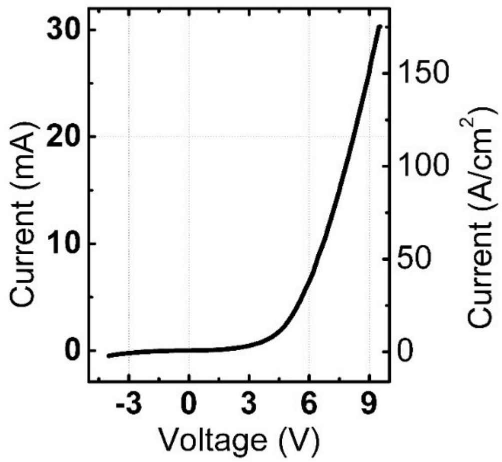

Figure 2.4: I-V characteristics of the diode.

2.1.3 Results of the N-polar green LED and discussion

I-V characteristic of a typical N-polar LED is shown in Fig. 2.4. The differential resistance and turn-on voltage were 0.012 Ω.cm^2 (72 Ω) and 5 V, respectively. It can be seen that the diode is leaky which is attributed to non-optimal N-polar crystal growth and fabrication. This is further confirmed with the image of the forward biased LED as shown in the inset of Figure 2.5. There were dark spots as well as green spots over the sample surface. This microscopic variation of emission uniformity can be due to non-uniform Mg incorporation during p-GaN growth under Ga-rich conditions. The electroluminescence (EL) spectra for increasing driving current are shown in Fig. 2.5. The maximum current driven in this regime was 30 mA, corresponding to a density of 176 A/cm^2. The peak wavelengths, peak intensities and full width at haft maximums (FWHM) as a function of driving current are shown in Figure 2.6. An increase in the driving current results in a linear increase in the EL emission intensity up to 88 A/cm^2, and after that point, it starts to saturate which might be due to the excess device heating. The peak wavelengths were measured as 563 nm and 540 nm at 2 mA and 30 mA, respectively. The 23 nm blue shift over 28 mA (165A /cm^2) is attributed to screening of the piezoelectric field by electrons and holes at higher injection current density. [45] Note that there is only 0.7 nm blue shift from 88 to 176 A/cm^2 which may result from a competition between state-filling effect and heat generation. [46]

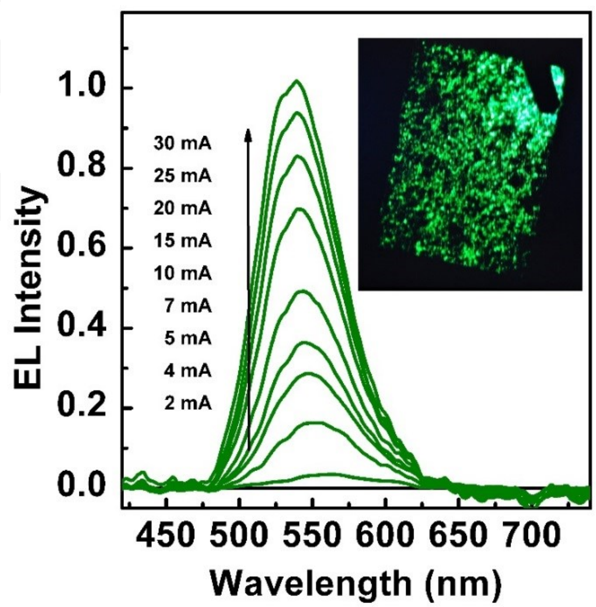

Figure 2.5: Electro-luminescence spectra of World's first N-polar green LED. Inset shows the optical microscope image of the LED taken under forward bias.

The emission FWHM variation as a function of drive current showed a decreasing trend from 74 nm to 63.4 nm at 2-mA and 30 mA, respectively. Decreasing FWHM for low current regime has been attributed to band filling effect caused by potential fluctuations. However, we have observed the decreasing trend of FWHM regardless of current injection. We also note that past reports showed increasing FWHMs for Ga polar and semi polar leds and this behavior was attributed to screening charges and excess heat generation. [46,47] The opposite (and desirable) behavior in the case of N-polar LEDs may be attributed to the effects of N-polar growth and the reversed direction of polarization. While further investigations are needed to clarify these issues, we note that the FWHM saturates after 7 mA (41 A/cm^2). In this current range, the device starts suffering from heat which should result in an increasing FWHM thus; a possible competition between the effects of N-polar orientation and heat generation might explain the saturation of FWHM.

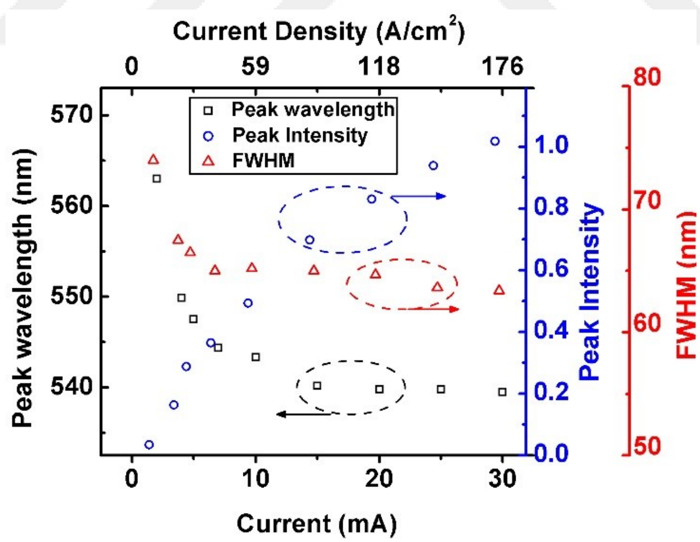

Figure 2.6: The peak wavelength, peak intensity and fwhm of the EL spectrum of the device.

2.1.4 Conclusions

In conclusion, N-face InGaN green LED was grown by MBE and fabricated successfully. The EL measurement results of the device showed a short blue shift from 563 nm to 540 nm and a decreasing FWHM from 74 nm to 63.4 nm under 80 mA (165 A/cm^2) current range. These results demonstrates the first N-polar green LED. As the device characteristics showed many problems such as current leakage, microscopic scale non-uniform emission patterns with very low radiative power, high EL fwhm (large In-atomic fluctuations). Further optimization in material growth and fabrication is required to enhance the LED performance. Optimization of InGaN emitting layer and p-GaN could lead to improved performance of N-polar emitters. In the next section, the growth of N-polar InGaN layer is optimized.

2.2 Plasma Assisted Molecular Beam Epitaxy growth of InGaN under N-rich Conditions

2.2.1 Introduction

There has been extensive work on the MBE of (In)GaN. It has been shown that N-polar GaN decomposes at a higher growth temperature (T > 800 ^{o}C) [48] compared to Ga-polar counterpart which enables the growth with higher adatom mobility. Also, the existence of lower diffusion barrier for Ga adatoms under N-rich condition [49] has been revealed which has enabled the growth of N-polar GaN under step flow mode at elevated temperatures (T=730 ^{o}C), unlike the 3-D growth of Ga-polar GaN in similar conditions, [50] However, by further increasing the growth temperature (T>760 ^{o}C), step flow growth of Ga-polar GaN under N-rich condition is possible. [50] This growth is limited by the generation of active Nitrogen flux to overcome the decomposition as Ga-polar GaN decomposes at a growth temperature higher than 750 ^{o}C.

It was reported that N-rich growth of Ga-polar InGaN results in 3-D morphology. [51] This is attributed to the absence of In coverage which acts as surfactant on Ga-polar surface. [52] Whereas, near stoichiometry or slightly N-rich conditions was shown to enable 2D layer by layer growth for In % < 18% and SK growth mode for In-compositions exceeding 18% with 2D to 3D transition after few monolayers of InGaN. [53] The growth of In-polar InN has been reported to be limited to substrate temperatures below 500 ^{o}C beyond which the vacuum decomposition rate is much higher than the growth rate, whereas N-polar InN has been grown by PAMBE at much higher substrate temperatures of 600 ^{o}C. [36,37] Similarly, N-polar InGaN grown under In-rich conditions exhibits higher Indium incorporation compared to Ga(In)-polar samples. In that study, Nath et al. [54] observed a decrease in In-content of relaxed InGaN films in both crystal polarities as the substrate temperature was increased from 500 ^{o}C to 600 ^{o}C due to thermal decomposition of InN. Additionally, semi-polar facets were observed in all strain relaxed N-polar InGaN films grown under In-rich conditions. [54] It should also be noted that the N-polar green LED charterized in the previous section had InGaN quantum wells grown under In-rich conditions and shown to have very low radiative power and microscopically non-uniform emission. Here, we examine the structural, optical, and electro-luminescent properties of N-polar InGaN grown under N-rich conditions to enable the growth of high power N-polar LEDs.

2.2.2 Experimental Design of the MBE growth

A Veeco RF plasma source was used at a plasma power of 350 W with N_2 flow rate adjusted to yield a background system pressure of 2 x 10^{-5} torr with the plasma lit. The active nitrogen under these conditions leads to a N-limited GaN growth rate of 4.5 nm/min. We define the III:N beam flux ratio as 1:1 at the III source beam equivalent pressure (1.9 x 10^{-7} torr for Ga and 2.1 x 10^{-7} torr for In) where the active nitrogen and III flux (Ga or In) are balanced (the cross over from III-limited to N-limited growth). The substrates, N-polar free-standing GaN with dislocation density < 10^8 cm^{-2}, were obtained from Lumilog[30] cleaved into ~1 x 1 cm^2 pieces and loaded on 2" Silicon carrier wafers using indium for bonding. For each sample, a buffer layer consisting of 50 nm of GaN was first deposited at 710 ^oC with Ga:N flux ratio of 2.4. The substrate temperature was then decreased to 530-675 ^oC for InGaN growth, and the indium flux was kept constant throughout the growths at In:N = 0.12. The Ga:N flux ratio was set to 0.42 (referred to as series A) and 0.21 (referred to as series B) for the growth of relatively low and high In composition InGaN respectively. Assuming no decomposition under N-rich growth, Indium composition (x) can be found using the following equation,

$$x = \frac{\Phi_{In}}{\Phi_{In}+\Phi_{Ga}} \tag{2.1}$$

where, Φ_{In} is In:N and Φ_{Ga} is Ga:N flux ratio. According to the Eqn. 2.1, the corresponding Indium composition with the flux ratios used in the experiment is $x = 22\%$ and 36% for series A and B, respectively. All of the bulk InGaN growths were designed for a nominal thickness of ~60 nm assuming negligible decomposition. Following the growth of InGaN, the substrate was cooled down to room temperature.

Room temperature photoluminescence (RT PL) measurements were performed by Thomas Kent at the Ohio State University using a mode-locked Ti:sapphire oscillator (Coherent Chameleon Ultra II) operating at 900 nm, a repetition rate of 40 MHz, pulse width of 150 fs. The laser output was then frequency tripled yielding an excitation wavelength of 300 nm, and average power of 10 mW focused onto the sample through a 36×, 0.5 numerical aperture reflective objective. The PL was collected, passed through a 300 nm long pass filter, and focused onto the monochromator (SP2500i), and dispersed onto a PI PIXIS 100 CCD camera. Time resolved photoluminescence (TR-PL) measurements utilized the same reflective objective described above for excitation and collection, while the Ti:sapphire laser was tuned to 740 nm, a 40 MHz repetition rate, frequency doubled to an excitation wavelength of 370 nm, and finally focused to a 10 micron spot size on the sample at an average power density of 764 kW/cm^2. The collected PL photons passed through a 300 nm long pass filter, and were focused on a 150 mm f/4 spectrometer and then counted using a Hamamatsu R38009U-51 micro channel plate photomultiplier tube. The photocurrent pulses were pre-amplified then input to an SPC-130 time correlated single photon counting system (Becker & Hickl).The instrument response function (IRF) of the system with full width half maximum (FWHM) < 60 ps was measured. TRPL decay curves were collected at temperatures of 200 K and 300 K with the spectrometer set to the peak center of the PL emission at 552 nm.

The high resolution x-ray diffraction (HR-XRD) ω-2θ measurements were collected symmetrically about the (000-2) diffraction peak of GaN using a Bede HR-XRD system with Ge hybrid monochromator and Cu $K\alpha_1$ radiation (k=1.54056 A). The surface morphology of the samples was evaluated with atomic force microscopy (AFM) using a Veeco DI 3000 under tapping mode.

2.2.3 Experimental results of N-polar InGaN

The HR-XRD ω-2θ scans of the low Indium composition samples (series A) are shown in Fig.2.7a. Samples grown at a temperature range from 530 ºC to 630 ºC exhibit similar InGaN diffraction peaks (out of plane lattice constants), whereas the diffraction peak for samples grown at 650 ºC and 675 ºC are shifted to longer angles corresponding to reduced out of plane lattice constants implying reduced In-compositions. The indium composition of the samples is estimated according to the ω-2θ scan peak positions assuming that the films are fully strain relaxed. The resulting In composition of sample series A is shown in Fig. c. The In-composition of the samples grown at 600 ºC and 630 ºC is 22%, matching the low-decomposition limit estimate, and suggests negligible decomposition up to a substrate temperature of 600 ºC, whereas previous reports of N-polar InGaN grown under In-rich growth conditions [54] showed significant decomposition at the same substrate temperature. The compositions were also verified using PL measurements. It is evident that reduced decomposition of In-N bonds occurs under N-rich growth condition. Further increase in temperature above 630 ºC resulted in a sharp decrease in InN content (Fig. 1c) due to the InN decomposition, followed by In evaporation from sample surface.

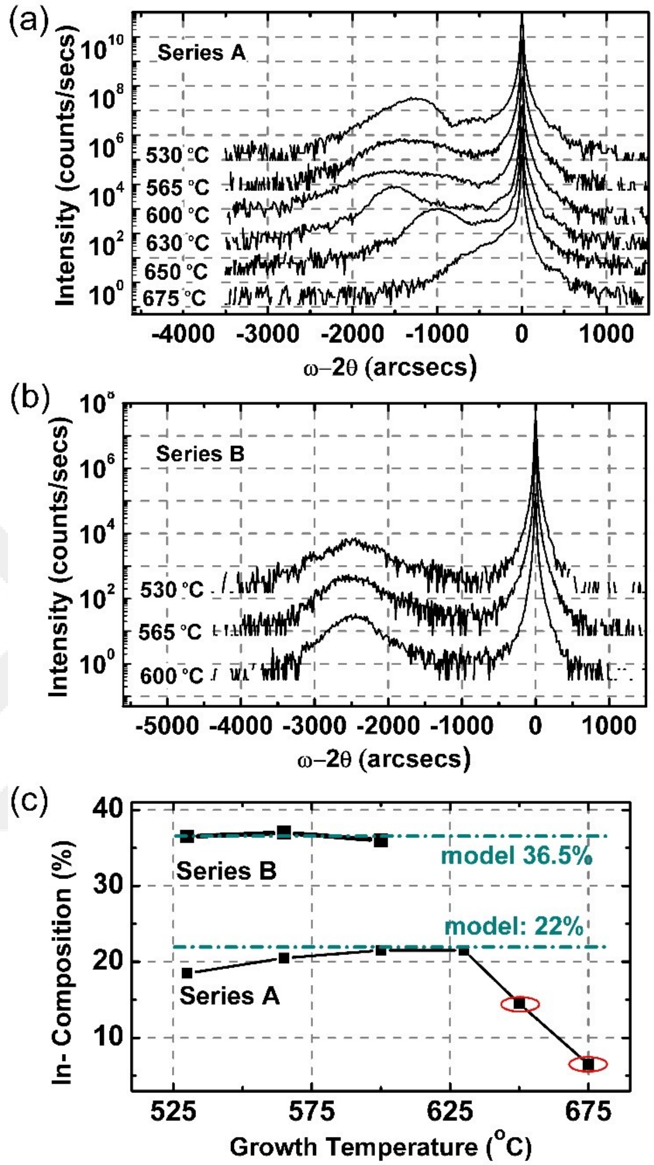

Figure 2.7: The omega-2 theta high resolution X-Ray diffraction scans of the samples in (a) series A and (b) series B. (c) Extracted In atomic ration in for series A and B. The data points with red circles denotes the samples grown under decomposition regime and In % may be overestimated for those.

Fig. 2.7b shows the HR-XRD ω-2θ scans of the high Indium composition (B) series. In agreement with the series A, InN decomposition was not noticed at growth temperatures up to 600 ºC. The Indium composition (estimated from ω-2θ scan peak positions assuming fully relaxed film) of series B is shown in Fig. 2.7c. It is seen that measured Indium composition agrees well with the growth model which confirms no decomposition during the growth up to 600 ºC. The samples with growth temperature of 630 ºC and 650 ºC were grown under InN decomposition regime, thus In atomic ratio is lower. Since the estimate of In% was based on assumption of fully relaxation, the In% for these samples may be overestimated which are denoted by red circles in Fig. 2.7c.

The PL measurement of series A is shown in Fig. 2a. All samples showed relatively broad PL emission with the peak wavelength located at a longer wavelength than what is expected from ~22% InGaN PL emission. Similar phenomenon has been observed reported for Ga-polar InGaN films grown under N-rich conditions and attributed to presence of large alloy fluctuation. [56, 57] Optically generated electrons and holes gets confined in the regions with higher In atomic ratio, thus dominates the PL spectra with higher radiative recombination rates compared the regions with lower atomic ratio. Thus, it is misleading to estimate In% from PL specta of N-polar InGaN.

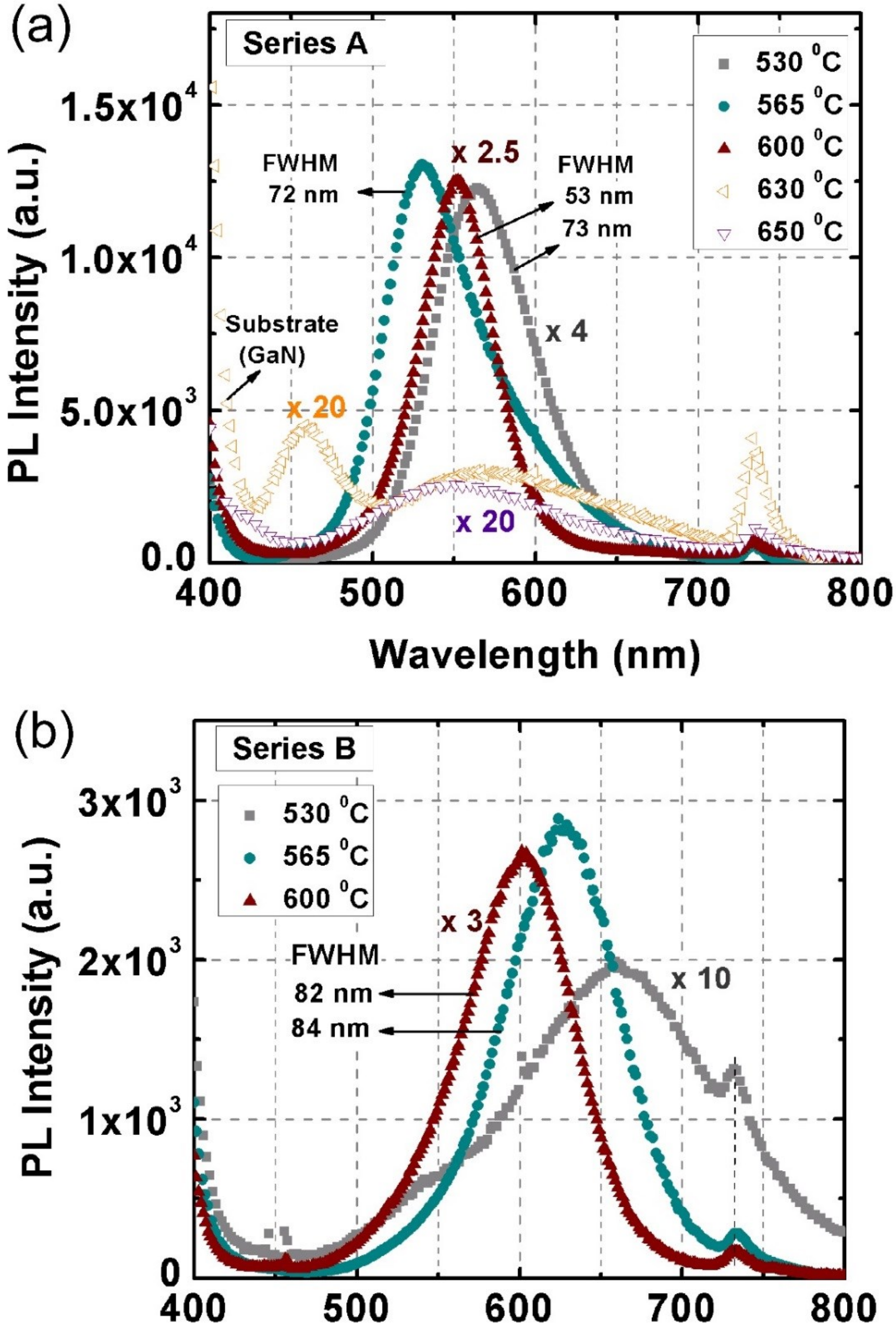

Figure 2.8: Photo-luminescence spectra of the samples in (a) series A and (b) series B.

There were two distinct characteristics observed from the series. For low temperature growths (T<600 ºC), single phase InGaN with strong single peak green emissions were observed. The PL peaks were measured in the wavelength range of 530-560 nm. The narrowest PL FWHM of 53 nm was obtained from the sample grown at a temperature of 600 ºC with a peak wavelength at 550 nm. In the high temperature regime (T>600 ºC), a weak high energy emission, and a broad-band yellow luminescence were observed. The PL peak of the band-edge emission was measured at 460 nm and 418 nm for the growth temperature at 630 ºC and 650 ºC respectively. The broad yellow band luminescence (FWHM ~130nm) has been attributed to defect induced transitions in (In)GaN. [58] The indium incorporation decreased with increasing temperature and the band-edge emission shifted to higher energy with further reduction in the emission intensity which is attributed to spinodal decomposition [59] commonly observed at high temperature. Thus, the optimal growth temperature window was determined as 530 ºC < T < 600 ºC for $In_xGa_{1-x}N$ with x < 22%.

Based on the conclusions from Series A, where high temperature growths (T>600 ºC) resulted in phase separation and thermal decomposition, the temperature range for growth of Series B was limited to 600 ºC. The PL measurement of these samples is shown in Fig. 2.8b. Similar to Series A, the samples grown at 565 ºC and 600 ºC showed high intensity single peak emission. The PL emission peak wavelengths (and FWHM) were measured as 630 nm (FWHM of 84 nm) and 600 nm (FWHM of 82 nm) for the samples grown at 565 ºC and 600 ºC respectively. On the other hand, at 530 ºC, phase segregation and significantly lower PL intensity peaking at 650 mn with a local peak ~550 nm was observed. Although it is known that phase separation is a kinetically driven process, it was observed during low temperature growth of high In-composition bulk N-polar InGaN under N-rich conditions. Further investigations needed to figure out the mechanisms of the process. Thus, for the N-rich growth of single phase high composition (x ~ 36.5 %) N-polar $In_x Ga_{1-x} N$ in Series B, our results suggest that the optimal growth temperature is narrower than that of Series A (x ~ 22%), limited between 565 ^oC and 600 ^oC. Also, it is noteworthy that the peak wavelengths of the samples in series A and B are relatively close to each other. For instance, the samples grown at 600 ^oC for series A (~21% In) and B (~37% In) showed peak wavelength at 550 nm and 600 nm respectively. This implies that the emission peak was dominated by In- allow fluctuation. In-rich regions of the film confines the carriers and dominates the PL spectra of the samples. We noted that the PL peak ~740 nm present in Fig. 2a and b is due to second order diffraction of intense GaN PL emission from the diffraction grading.

TRPL measurement results of the $In_{0.22}Ga_{0.78}N$ sample (600 ^oC growth, PL peak at 552 nm with the narrowest FWHM of 53 nm among all samples) are shown in Fig. 2.9. PL lifetimes are reported by fitting a single time constant decaying 'stretched' exponential function;

$$I = I_0 x \exp\left\{-\left(\frac{t}{\tau_{PL}}\right)^{\beta}\right\} \tag{2.2}$$

where I_0 represents PL intensity at t=0 sec, τ_{PL} is PL life time and β is a parameter representing disorder, assumed to be 0.5 which is comparable to previous investigations. [59] The measured data fit well with the equation for first 3 ns of the decay trace. PL lifetimes were measured to be 0.9107 ns and 1.5810 ns at 300K and 10K respectively. Assuming 100% internal quantum efficiency (IQE) at 20 K, [60] the IQE of 16.07% at 300

K was obtained under 764 kW/cm^2 of excitation which yields radiative and non-radiative lifetimes of 1.545 ns and 0.296 ns, respectively. It is noted that the RT radiative lifetime (1.545 ns) is similar to the values reported for metal polar InGaN. [61] Such high radiative lifetime has been attributed to carrier localization due to compositional of 0.1 -1 ns [62-64] which indicates that N-polar InGaN has comparable radiative and non-radiative carrier lifetime inhomogeneity. [65] The RT non-radiative lifetime of 0.296 ns also falls in the range of the reported values for metal polar InGaN values to the metal polar counterpart.

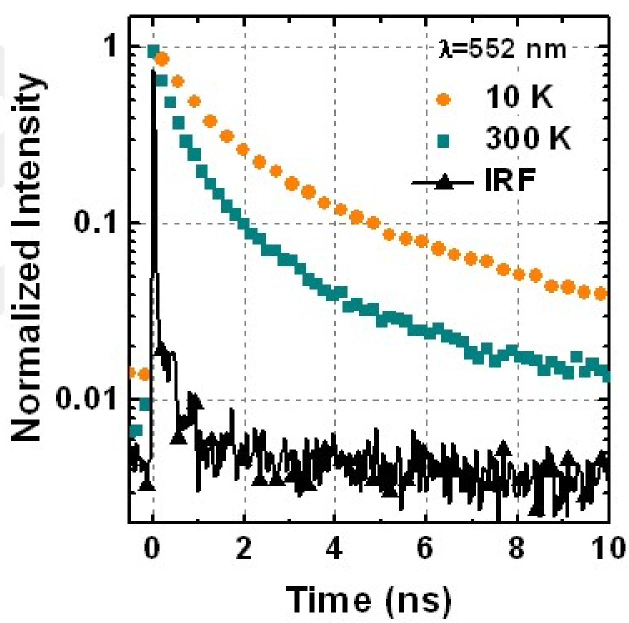

Figure 2.9: Time-resolved photo-luminescence spectra of $In_{0.22}Ga_{0.78}N$ (sample from series A grown at 600 ^0C) at 10K and 300K, PL intensity measured at 552 nm. Measured by Thomas Kent at OSU.

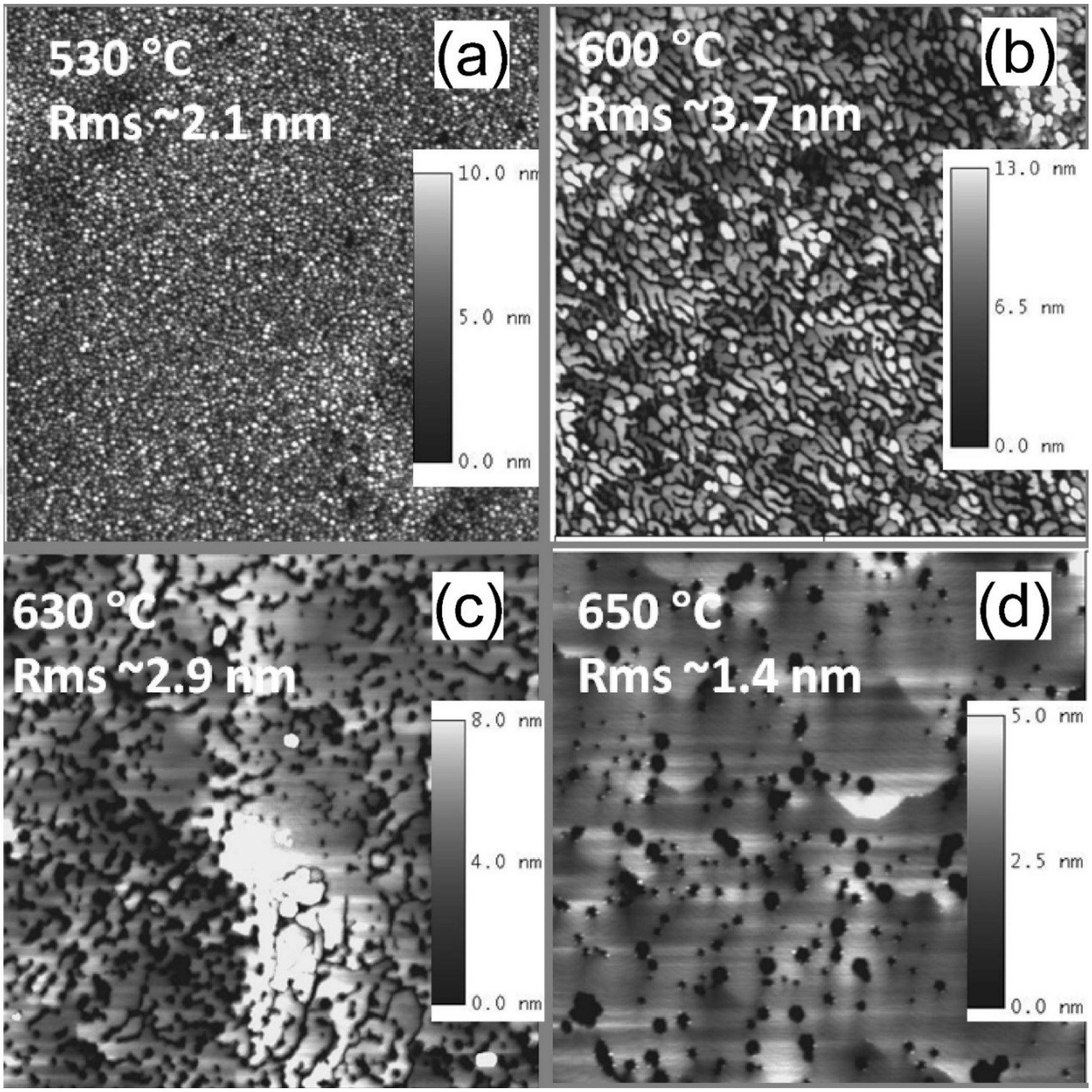

Figure 2.10: Atomic force microscopy 2 x 2 μm^2 images of ~ 60 nm InGaN films grown under N-rich conditions at a growth temperature of (a) 530 ºC, (b) 600 ºC, (c) 630 ºC and (d) 650 ºC.

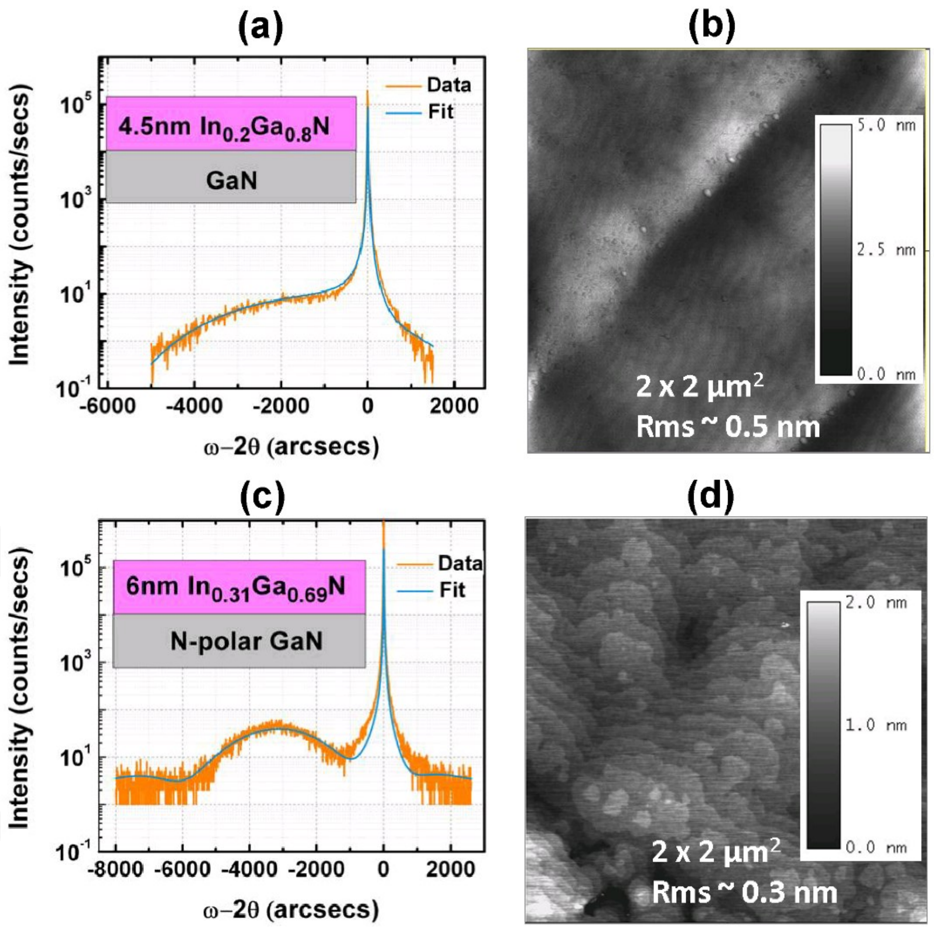

Figure 2.11: (a) & (c) The omega-2theta scans and (b) & (d) AFM images of the thin InGaN films grown at 600 ºC following the growth condition of bulk InGaN growths of series A & B, respectively.

The AFM scans (2 µm X 2 µm) of the low Indium composition series are shown in Fig 2.11. The images reveal the morphological evolution from 3D growth with tiny pillar like structures at 530 ºC to larger pillars at 600 ºC. Step flow growth with large islands was observed at 630 ºC and coalesced islands with hexagonal pits were found at 650 ºC, leading to the smooth surfaces with 1.4 nm rms roughness. As the growth temperature was increased above 600 ^{0}C and especially for the growth at 650 ^{0}C, it is noticed that the surface is almost identical to the binary N-polar GaN grown under N-rich conditions, [49] which is expected due to InN decomposition resulting in low (< 6.5 %) In composition at this growth regime. The morphological evolution from tiny pillars to larger and flatter ones was attributed to the presence of higher adatom mobility with increasing temperature. It is noteworthy that unlike InGaN bulk films grown under In-rich conditions, [54] semi-polar facets were not observed from any of the samples in this study.

Since the morphology is highly dependent on relaxation kinetics, thin InGaN films were also investigated under growth conditions similar to bulk samples. Two samples were grown at 600 ^{0}C (optimum temperature found above) targeting Indium compositions (x) of 20% and 32% using growth model given in eqn. (1) by adjusting Ga and In flux accordingly. Since, it was found from bulk InGaN growths that there is no decomposition for this (20%-32%) In- composition range, the growth thickness can be nominally determined and the Bede software was used to fit the scan data assuming fully strained InGaN layers. The simulation fitted well with the data for both samples at (4.5 nm thick) $In_{0.2}Ga_{0.8}N$ and (6 nm thick) $In_{0.31}Ga_{0.69}N$ which agrees well with the growth design (the thickness of the samples were designed for another study). The AFM scans (2 μm x 2 μm) of the 4.5 nm $In_{0.2}Ga_{0.8}N$ and 6 nm $In_{0.31}Ga_{0.69}N$ is shown in Fig 2.11b and d respectively. Atomic steps were observed from both samples and the surface rms roughness measured as 0.5 nm and 0.3 nm for $In_{0.2}Ga_{0.8}N$ and $In_{0.31}Ga_{0.69}N$ respectively. As the growth morphology of relaxed (Fig. 2.10) and strained (Fig.2.11b and d) InGaN films compared, the change in growth mode from 2-D step flow to 3-D nano-pillar/island growth, SK growth mode, was observed. Our results indicate that growth under the optimal conditions can provide high-quality InGaN with good morphology as long as the InGaN films are thin enough to prevent relaxation.

2.2.4 Conclusions

The PAMBE growth and characterization of N-polar InGaN under N-rich conditions is investigated. It is found that there is negligible InN decomposition from the InGaN films with InN content as high as 37% for growth temperatures up to 600 ^{o}C. The optimum growth temperature for bulk samples with high intensity single peak PL emission was determined to be from 565 ^{o}C to 600 ^{o}C. Although sample surfaces of thick InGaN layers were found to be rough with rms roughness between 2.1 - 3.7 nm, pseoudomorphic InGaN films grown under similar conditions gave smooth surface morphologies (rms ~ 0.3 – 0.5 nm) with step flow growth features . Our work shows that the growth of N-polar InGaN in N-rich conditions leads to good quality thin films, and the optimal growth conditions can be directly applied to device applications such as LEDs and high electron mobility transistors (HEMT) with high In- composition InGaN channel layers for high frequency applications.

2.3 Suppression of electron overflow and efficiency droop in N-polar LEDs with InGaN grown under N-rich conditions

2.3.1 Introduction

Efficiency droop is higher for longer wavelength emitters such as in the technologically important green wavelength region and while the reason for this remains a topic of active research, various groups have identified it to be due to Auger recombination processes, overflow electron current, and inefficient carrier injection and transport mechanisms. [25-30, 66] Recently, it has been reported that the proposed Auger non-radiative recombination process is unlikely to be the cause for the droop since the Auger recombination coefficients are too low to account for the efficiency losses. [67] The effects of electron overflow current on droop were investigated using multiple-quantum-well (MQW) active regions, $Al_xGa_{1-x}N$ and lattice matched InAlN electron blocking layers (EBLs), and non-polar LEDs. [22, 31-33] While these were shown to improve the efficiency, the use of MQWs and EBLs also degrades the carrier injection and transport mechanisms. [28, 29, 68] In addition, previous reports showed that EBLs mitigate efficiency droop in non-polar devices implying that electron overflow plays an important role even in non-polar InGaN LEDs. [69]

Most commercial LEDs are fabricated with the p-top junction oriented along the +c or (0001) direction (**p** on top of **n** on a **+c** oriented substrate). *Reversed* polarization devices can be achieved using a p-down structure on a Ga-polar substrate (**n** on top of **p** on a **+c** oriented substrate) or a p-up junction on a –c oriented or N-polar substrate (**p** on top of **n** on a **-c** oriented substrate). Simulations of reversed polarization emitters indicate several advantages over conventional emitters for device parameters such as electron overflow, injection efficiency, and laser threshold current density. [70, 71] However, there have been very few experimental reports on InGaN/GaN quantum well emitters with reverse polarization [72, 73] due to the inherent challenges in growth and fabrication. Ga-polar p-down devices have been investigated [73] but found to be impractical due to the difficulty in obtaining low contact resistance to the etched p-type region and current crowding in resistive p-type epitaxial layers. Here, p-up junctions on an N-polar substrate was investigated to characterize the effects of reverse polarization in N-polar LEDs and show (i) that the efficiency droop can be correlated with electron overflow effects, and (ii) that the reversal of built-in polarization fields in these N-polar LEDs can be used to mitigate electron overflow and efficiency droop at higher currents.

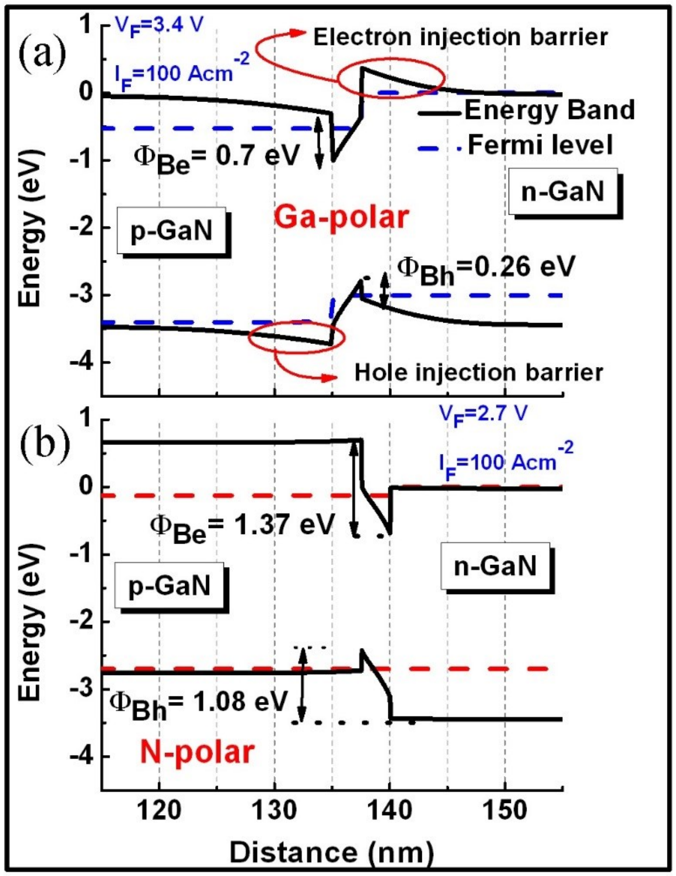

Figure 2.12 Energy band diagram of single quantum well p-up LEDs under forward current density of 100 A/cm^2 for (a) Ga- (b) N-polarity.

Figure 2.12a and b shows simulated band diagrams of the SQW structures under a forward current density of 100 A/cm^2 along Ga- and N-polarity, respectively. The epitaxial structure of the simulated device is depicted in Fig. 2.13a. Simulations were performed with Silvaco Atlas [74] using widely accepted parameters for Auger recombination, [75] optical recombination, [76] and polarization sheet charge values. [2] The potential barriers blocking injection of carriers *into the quantum well* for the Ga-polar orientation are absent in the reversed polarity (N-polar) case (Fig. 2.12b) which manifests as higher operating or biasing voltage for Ga-polar orientation (3.4 V) than for N-polar orientation (2.7 V) for achieving the same current density of 100 A/cm^2. After injection into the quantum well, the electrons are accelerated towards the p-GaN region by the polarization field in the Ga-polar QW, and have significant likelihood of tunneling or overflowing if no blocking layers are provided. In the N-polar case, injected electrons are confined at the n-GaN side and kept away from the n-GaN side by the polarization field-induced potential barrier in the QW. The N-polar device showed 1.37eV potential barrier height for electrons (Φ_{Be}) and 1.08 eV (Φ_{Bh}) for holes. Such values are limited to conduction and valence band offsets in Ga-polarity which are 0.7 and 0.26 eV for electrons and holes respectively. Above simulations thus show that both electron and hole overflows are higher in a Ga-polar than in an N-polar device.

2.3.2 Experimental approach of realization of N-polar LEDs

The InGaN SQW growth was carried out at ~570 °C (from optical pyrometer). As shown by the schematic in Fig. 2.13, the growth was initiated with 50 nm of Silicon doped (~3e18) GaN, 15 nm unintentionally doped (UID) GaN under Ga-rich conditions, followed by 2.5 nm ~30% InGaN quantum well growth under N-rich condition. For the DQW case, a 5 nm UID-GaN barrier was placed above the quantum well, followed by a second 2.5 nm second quantum well. Both structures were capped with 100 nm p+ GaN ([Mg] ~ 2 x 10^{19} cm^{-3}) and 20 nm p++ GaN ([Mg] ~ 8 x 10^{19} cm^{-3}). Wider band-gap electron blocking layers (EBL), commonly used for Ga- and non-polar LEDs, were *not* used in these LEDs.

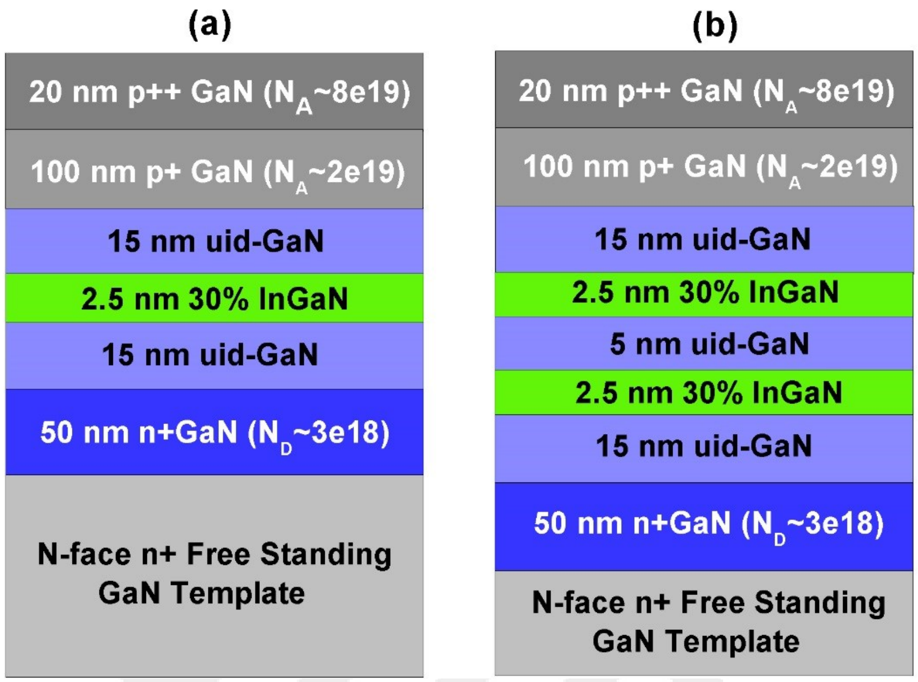

Figure 2.13: The epitaxial design of N-polar (a) single and (b) double quantum well LEDs with InGaN wells grown under N-rich conditions. Note: no electron blocking layers inserted to check intrinsic electron blocking properties.

The devices were fabricated using contact photolithography. A semi-transparent Ni/Au (4/6 nm) metal stack was evaporated to form the p-type electrode, followed by mesa isolation using Cl_2/BCl_3 ICP-RIE etching. Ti/Au (20/300 nm) was deposited for n-GaN contacts, and thick Au current spreading contacts were formed on the top p-GaN contacts. The measurements reported here were performed on-wafer (no dicing or packaging) for 250 µm X 250 µm devices. The electro-luminescence (EL) data was obtained using Ocean Optics USB 2000 spectrometer with a coupled fiber optic cable.

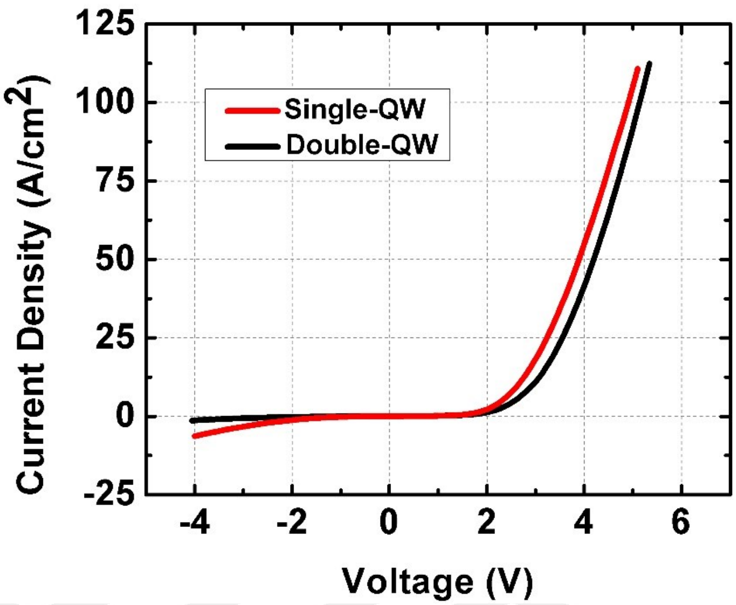

Figure 2.14: I-V characteristics of single and double quantum well LEDs.

2.3.3 Results of the N-polar LEDs and Discussion

Fig. 2.14(b) shows the current-voltage (I-V) plots of both LEDs. They had relatively low turn-on voltage (~2.3 V) which is attributed to decreased electron and hole potential barriers in N-polar devices validating our preceding simulated results. The presence of higher leakage current in the SQW device (Fig. 2.14) may be due to increase in inter-band tunneling of electrons and holes across thin N-polar active region. [77, 78] The electroluminescence (EL) spectrum of SQW and DQW LEDs (Fig. 2.15 (a) and (b)) showed similar peak wavelengths in the green wavelength range under continuous wave (CW) electrical excitation. The EL emission peak shifted from 558 nm to 535 nm for SQW LED while it shifted from 565 nm to 535 nm for DQW as the current density was increased from 16 A/cm^2 to 192 A/cm^2. The rapid blue shift in relatively low driven current regime

(< ~50 A/cm^2) was attributed to the screening process of polarization charges and gradual blue shift at higher current operation to band filling effects. [45, 79] The only noticeable difference for the green emission was that the emission full-width-at-half-maximum (FWHM) of the SQW LED (~78 nm) was higher than for the DQW LED (~67 nm).

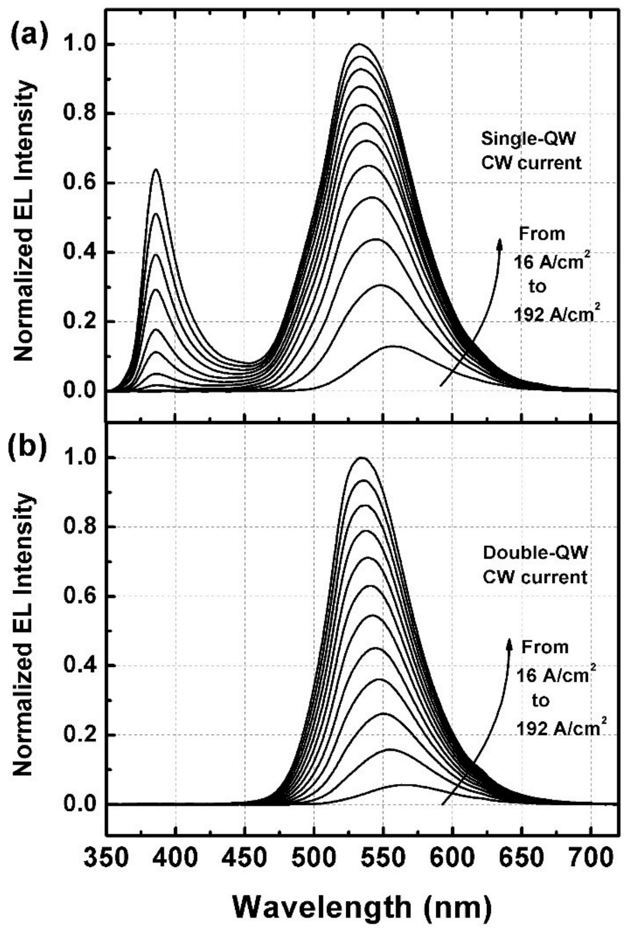

Figure 2.15: Electro-luminescence spectra of (a) single quantum well and (b) double quantum well LEDs.

The most important difference in the overall emission spectra of the two LEDs is the presence of UV emission with 385 nm peak wavelength (Fig. 2.15a) in the SQW LED when the drive current was higher than ~50 A/cm^2, which was *absent* for the DQW case (Fig. 2b). Interestingly, such spurious emission at 385 nm was observed by other groups for Ga- and non-polar MQWs with EBL incorporated LEDs, which had been attributed to radiative recombination due to overflowing (or tunneling) electrons from the active region to p-type GaN layers. [80-82] However, the DQW LED did not exhibit the 385 nm peak even at higher current densities up to 400 A/cm^2 (Fig. 2.15b). This concludes that while one quantum well with the given thickness may be insufficient to prevent electron overflow, the insertion of a second quantum well provides an efficient built-in potential barrier to prevent electron overflow in this N-polar device.

Fig. 2.16a shows the integrated EL intensity and normalized external-quantum-efficiency (EQE) of both SQW and DQW LEDs as a function of CW driving current. While SQW LED has the peak EQE at ~30 A/cm^2 and drops gradually at higher driving currents indicating conventional efficiency droop, the DQW LED has the peak EQE at ~ 96 A/cm^2 and drops only 7% at 192 A/cm^2 CW current density, indicating very little droop in efficiency. The spurious UV peak at 385 nm and thus carrier overflow can be attributed to be the reason for efficiency droop for the SQW based LED at higher drive current densities.

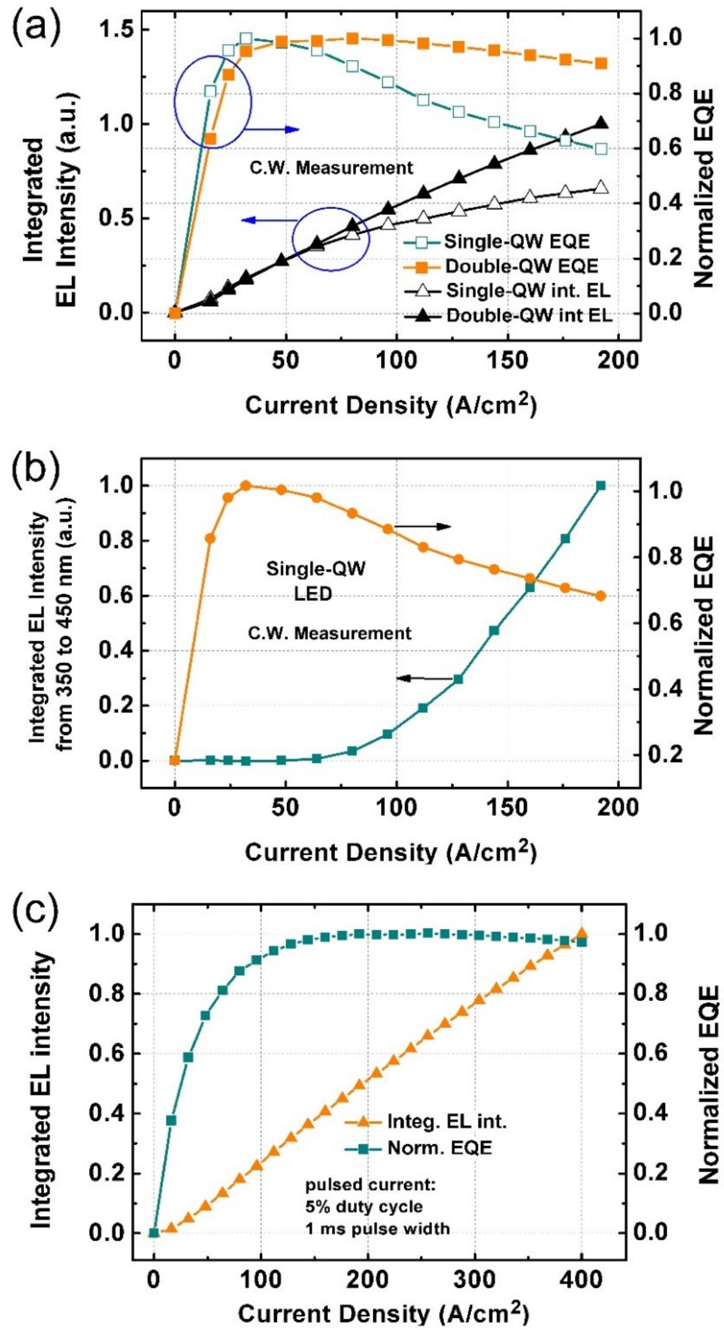

Figure 2.16: (a) The integrated EL intensity and normalized EQE variation of SQW and DQW LEDs with C.W. forward current. (b) The integrated UV-blue (350-450 nm) EL intensity and normalized EQE as a function of C.W. current density. (c) Normalized EQE and integrated EL intensity variation of DQW LED under pulsed current mode. The pulsing was done with 5% duty cycle and 20 ms repetition cycle with 1 ms on time.

This is transparent from Fig. 2.16b which shows integrated EL intensity for the UV peak only (350 to 450 nm) in the left-axis and the normalized EQE for the green emission of the SQW LED in the right-axis. Both drop in the normalized EQE (green emission) and the rise in the intensity of spurious UV peak become significant around the same current level implying that electron overflow *is the reason* for efficiency droop in SQW LED. This is further testified by Fig. 2.16c, where the normalized EQE for the green emission from the DQW LED which is free from spurious UV emission, stays flat with *no efficiency droop* till 400 A/cm^2.under pulsed current conditions. Thus, not only the direct correlation was established between electron overflow and efficiency droop but also demonstrated how to overcome it by using DQW in N-face orientation. It should be noted that the absolute radiative on-wafer output power of these LEDs are still below mW range (~ few 10s of μW). Further optimization is required for device growth (p-GaN, Si & Mg doping) and fabrication to improve these devices.

2.3.4 Conclusions

The emission characteristics of N-polar SQW and DQW LEDs were investigated. The devices emitted green (λ ~ 535-550 nm) light with a low turn-on voltage (~2.3 V). Relatively flat EQE curve was achieved up to 400 A/cm^2 with EBL free DQW N-polar LED. Low turn-on voltage and negligible efficiency droop characteristics were attributed to utilization of reversed (N-face) polarization charges for (1) elimination of potential barriers against carrier injection (outside the QW region) and (2) generation of potential barriers to confine carriers (inside the QW region). While the absolute efficiency values are still lower than the state-of-art green emitters due to non-optimized growth and fabrication, the experiment shows clearly that reversing the direction of polarization can lead to significant changes in emitter characteristics. While these results expand the current knowledge of the effects of polarization field on emitters and efficiency droop mechanism, further investigations would help understand the phenomena better and eventually lead to improved efficiency in III-nitride emitters.

Chapter 3

Cascading Nitride Light Emitting Diodes

This chapter describes the calculations of efficiency improvements in multiple active region LEDs. In the second part, experimental work to establish the growth of cascaded LED devices is discussed. In the last part, demonstration of triple-junction blue LED is discussed.

3.1 Motivation: Overcoming Efficiency Droop by Cascading Multiple LEDs

The underlying cause of efficiency droop is that for higher operating power density, LEDs are driven at higher currents. Here, a solution to the efficiency droop problem is proposed by electron transport engineered devices where high output power can be obtained at low current density. To do this, cascading multiple p-n junctions is shown by using visible transparent tunnel junctions with low resistance and low voltage drop. Combining the performance parameters of a commercial LED and the tunnel junctions, the efficiency droop problem was shown to be almost completely circumvented by using tunneling-based carrier recycling in cascaded multiple active region LED structures. Higher luminous output power can be achieved by increasing the operating voltage, rather than the current, and this can lead to unprecedented power density and efficiency for III-nitride LEDs.

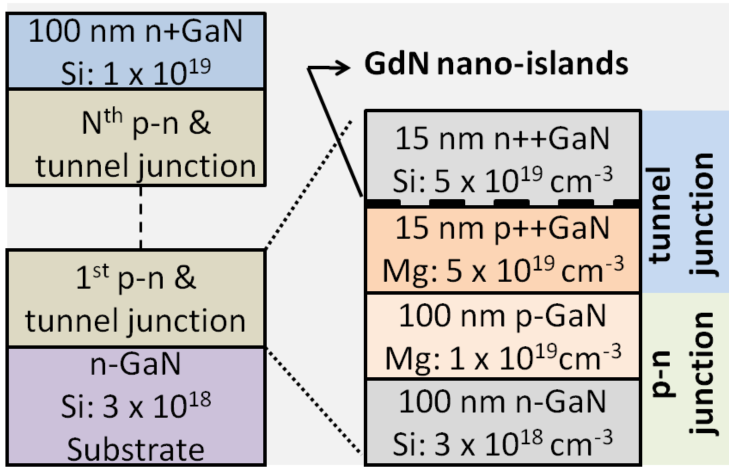

Figure 3.1: Epitaxial design of the cascaded of PN junctions for devices with N=1, 2 and 4.

3.2 Experimental work on cascaded GaN PN junctions

To demonstrate the feasibility of cascading GaN emitters, an experiment was designed using multiple (1, 2, and 4) p-n junctions connected epitaxially in series with tunnel junctions. The epitaxial structure (Figure 3.1) was grown by plasma assisted molecular beam epitaxy on free-standing n-type GaN substrates, and consisted of repeats (N=1, 2, and 4) of p-GaN/n-GaN junction diodes, and p+GaN/GdN nano-island/n+GaN tunnel junctions. Further details of GdN tunnel junctions are discussed elsewhere. [91 92] The top and bottom of this structure are both n-type since the tunnel junction eliminates the need for a top p-contact. The device was processed using contact lithography, mesa isolation was done using Cl_2/BCl_3 etching, and ohmic contacts (to top and bottom n-type regions) were made using Al/Au. The energy band diagrams of this structure at equilibrium and forward bias are shown in Figure 3.2a and b respectively. As the p-n junction is forward biased, the tunnel junction gets reverse biased, electrons in the valence band of p^+ GaN layer of the tunnel junction tunnel into empty states available in the n^+ GaN layer, leaving behind a hole in the p^+ GaN layer. These electrons and holes regenerated at p^+ and n^+ side of the tunnel junctions inject into the active region, in this case, a p-n junction. In case of a multi-quantum well active region, the injected hole and electron recombine radiatively.

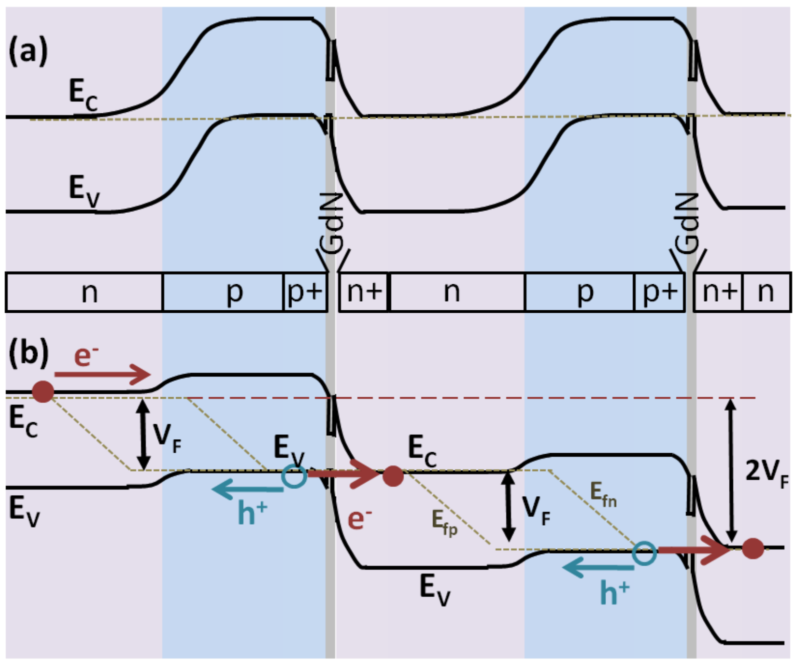

Figure 3.2: Schematic energy band diagram of the cascaded GaN PN-junctions under (a) zero (b) forward bias.

Electrical characteristics of 100 um^2 diodes of cascaded p-n junction stack (number of p-n junctions N=1, 2, and 4) are shown in Figure 3.3a and b. The turn-on voltage of the cascaded device increased with the number of p-n junctions stacked epitaxially. All the structures showed rectifying behavior, although the device with 4 junctions does show higher leakage current. This effect needs further investigation, and optimization of the growth conditions is expected to mitigate these effects. The series resistance (estimated from the linear portion of the IV curve) was found to scale with N, and based on this, the resistivity for each tunnel junction was estimated ~5.7 x 10^{-4} ohm-cm^2 (inset of Fig. 3 (b)). This resistance is relatively low and would lead to a negligible, a voltage drop of 57 mV for a current density of 100A/cm^2. This report of cascaded III-nitride p-n junctions with low series resistance could enable several devices including multi-junction solar cells, and multiple active region LEDs, which is discussed next.

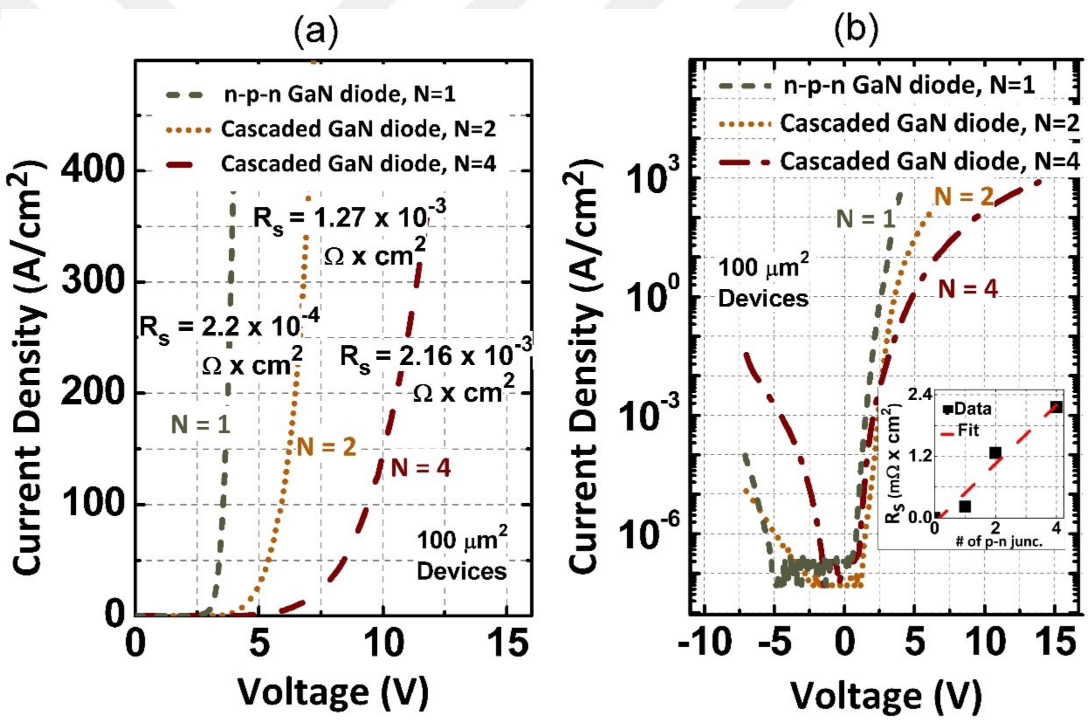

Figure 3.3: I-V characteristics of the cascaded PN-junctions up to four junctions in (a) linear (b) log scale. The inset to (b) shows the variation of total differential resistance with the number of the junctions.

3.3 Modelling Cascaded LEDs: Overcoming Efficiency Droop

Cascading GaN PN-junctions demonstrates the feasibility of cascading active regions, thus the measured results can be used to model cascaded multiple active region LEDs. To estimate the efficiency of cascaded LED structures, the estimated tunneling resistance and the experimental data from the commercial LED published elsewhere [93] were combined, so that non-idealities of the active region are taken into account. The modeled reference LED emits at 470 nm and consists of a 1.02 mm^2 mesa area with ZnO layer as contact to p-GaN. The differential series resistance (R_s) of the reported LED was ~ 0.02 $\Omega.cm^2$. The experimental data to the diode equation was fitted using,

$$I = C * \exp(\frac{q*(V-I*R_S)}{nkT}), \quad (3.1)$$

which is modified for the case of 'N' identical LEDs cascaded to

$$I = C * \exp\left(\frac{q*\left(\frac{V}{N}-I*R_S\right)}{nkT}\right), \quad (3.2)$$

where the series resistance of the tunnel junctions in the structure are taken into account, since the series resistance of n and p regions are much lower they have been ignored here. The tunnel junction resistance used for these calculations is the experimental value of $R_{s(TJ)} = 6.4 * 10^{-4}\ \Omega. cm^2$ which was the highest measured resistance value for a single TJ in the cascaded p-n junctions discussed above. Lower series resistance might be achieved with further optimization of the tunnel junctions. The modeled I-V curves (Fig. 3.4a) for the cascaded structure (N=5, 20, 50) behave as expected. The input voltage at turn-on increases as the number of junctions is increased.

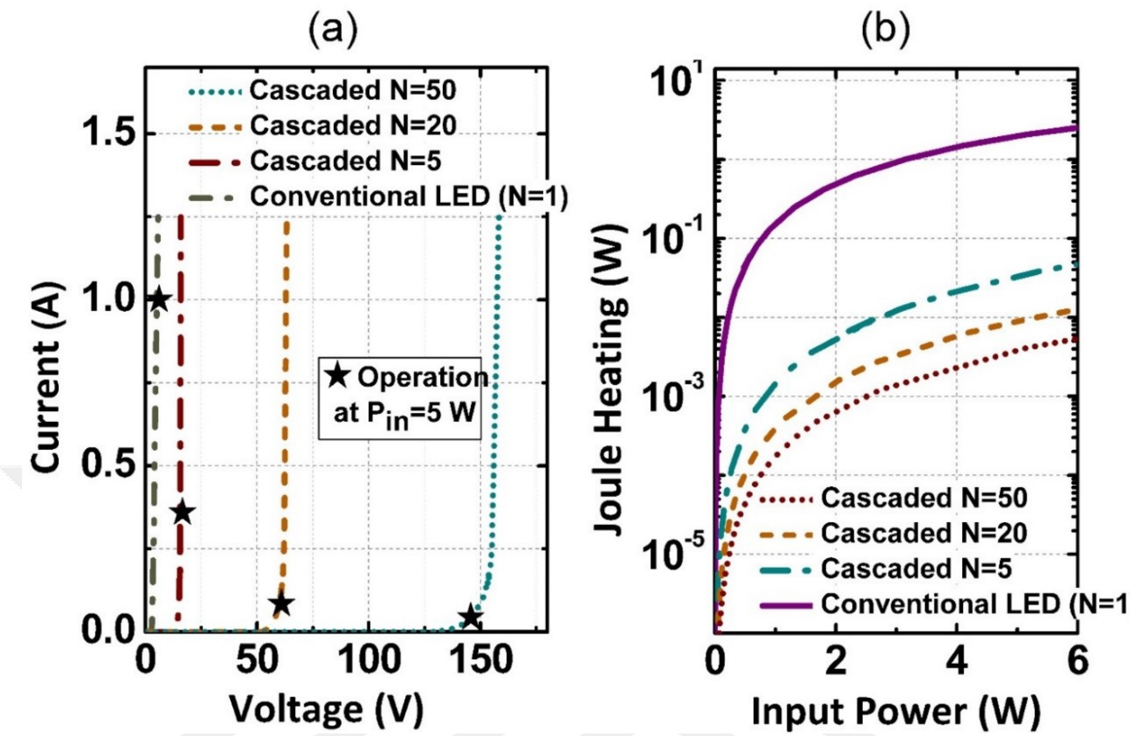

Figure 3.4: (a) I-V curve and (b) variation of joule heating with input power for the modelled LEDs with cascade of N=1, 5, 20 and 50 junctions.

The EQE versus injection current data of the reference LED was fitted using ABC model. It should be noted that this model is only used as an empirical fit, rather than to convey any physical information and does fit the experimentally observed data well. Combining with the I-V of the reference LED, the relation of the output power efficiency (WPE) to the input power of the LED was obtained. Using fitted efficiency curve of the reference LED together with resistive losses (due to tunnel junctions), the output power and efficiency characteristic of cascaded multi-junction LED can be estimated.

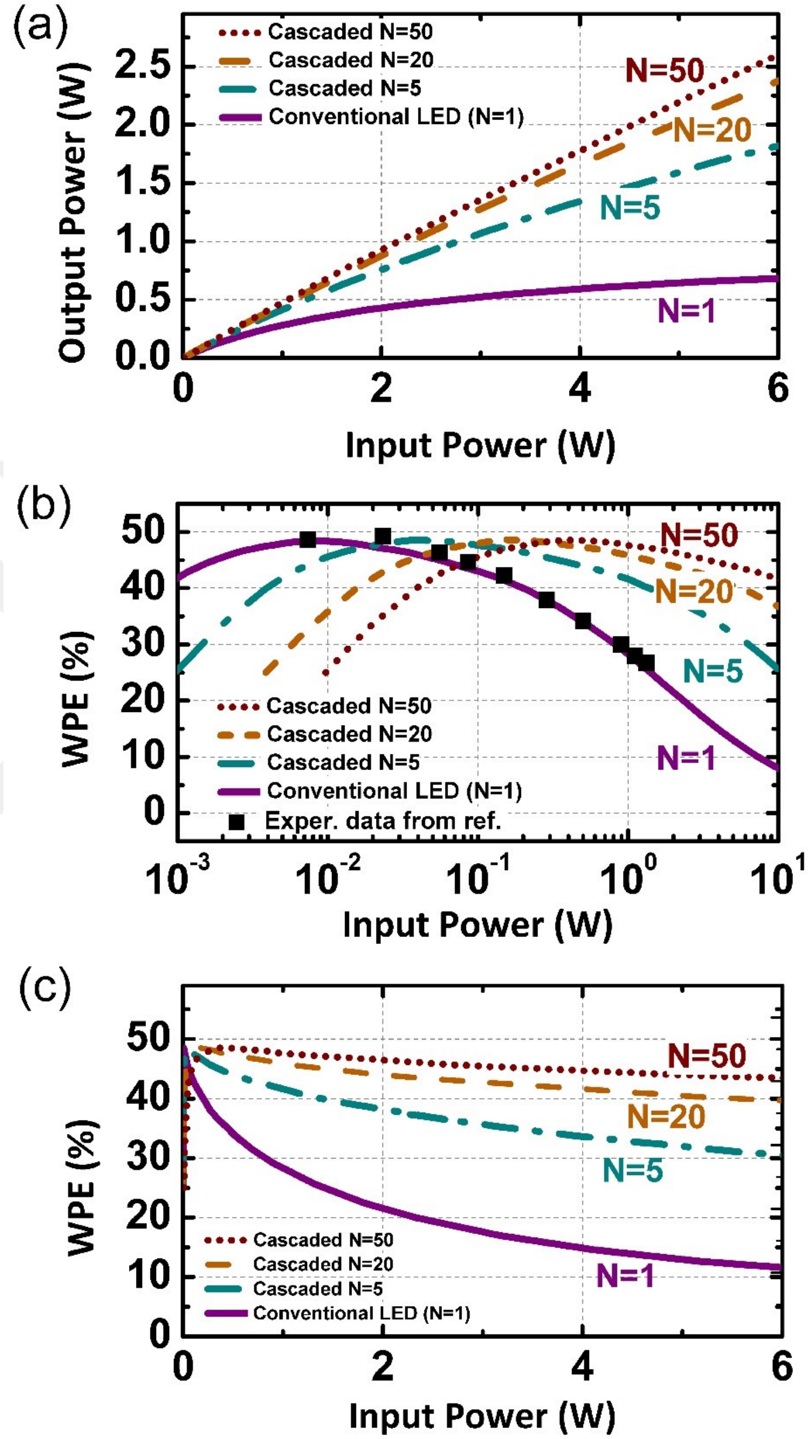

Figure 3.5: (a) radiative output power (b) wall-plug-efficiency cariation in logaritmic and (c) linear scale as a function of input power of the modelled LEDs with number of cascade N=1, 5, 20 and 50 junctions.

In figure 3.5a, the output power characteristics as a function of input power for cascaded LEDs and the conventional LED are compared. The input power, I x V includes the modeled I-V characteristics discussed above. Regarding the optical output power, it is assumed that a structure with N cascaded stages has $EQE_N = N \times EQE_{(single\ LED)}$. Although absorption loss via free-carriers and InGaN QW layers are expected to increase as ‘N’ increases, this was ignored for simplicity. Note that at the same input power level, relatively lower currents and higher voltages are needed for the Cascaded LED structures (Figure 3.4a). As expected, the conventional LED output power increases and saturates below 1 W under 10 W input power. As the number of cascade regions is increased, the saturation is pushed out further, with negligible saturation in output power for the LEDs with N=20 and N=50 cases reach above to 3.5 W..

These results are more striking when shown as efficiency versus power curves (Figure 3.5b and c). From these curves, it can be seen that for a cascaded structure with *N* stages, the maximum efficiency point occurs at approximately *N* times higher power than a single LED. This implies that the maximum device efficiency can be obtained at much higher drive powers even with an LED that exhibits significant droop. The WPE of the modeled conventional LED shows 87% droop at an input power of 5 W, and this value decreases as N increases (Fig.3.4b). For the LED with N=50, the droop is only 9.5% at the same input power which is an enhancement of ~240% in WPE compared to conventional case. The enhancement is not only due to superior external quantum efficiency, but also suppression of joule heating. Since the LED is operated at higher voltage and lower current, resistive losses are lower.

The superior performance of the cascaded LEDs is not only due to the enhancement in EQE but also due to the reduction in joule heating. The total power dissipated due to the series resistance of an LED is $P_R = I^2 R_S$. Since $R_s \propto N$ and $I \propto 1/N$, power dissipated on $R_s \propto 1/N$ which implies that increasing N enables high power operation of LEDs with higher efficiency by reducing overall heat generation. Resistive power dissipation as a function of input power is shown in Figure 3.4b for the modeled reference and cascaded LEDs with N=5, 20, 50 revealing the suppression in heat dissipation in cascaded LEDs. Such property is not only enhancing efficiency but also can enable LED operation at elevated output power.

While the proposed cascaded LEDs promise a tremendous breakthrough in nitride LED commercialization, there are some technological challenges that need to be overcome. Although GaN-based tunnel junctions [94-99] have been explored in the past, they have resulted in additional voltage drop of at least 0.5-1 V across the tunnel junction. Recently, efficient tunnel junctions have been demonstrated by molecular beam epitaxy using polarization engineering and mid-gap states. [77,78] However from the commercialization point of view, MOCVD technology for tunnel junction is desirable. The main problem in MOCVD tunnel junctions [94,95,99] is the activation of buried Mg-atoms (p-type dopant) in MOCVD/MOVPE growth and the outdiffusion of Mg atoms. Extensive investigations on making MOCVD tunnel junctions efficient is hence necessary as it provides a way to circumvent the LED efficiency droop problem which might be an inherent material problem.

In conclusion, using low resistance, visible blind GdN tunnel junctions, we have grown and fabricated epitaxially cascaded multiple GaN p-n junction diodes. I-V measurements showed the expected shift in diode turn on voltage as N increases up to 4 junctions. The average resistance of each tunnel junction was measured as 5.7 x 10^{-4} ohm-cm^2. In the second part of this report, a tremendous breakthrough on circumventing efficiency droop in nitride LEDs by cascading identical active regions with LEDs operating under high voltage rather than current was modelled. It was shown that the maximum efficiency point can be pushed towards higher input power regime as N increases. Efficiency droop can be greatly suppressed since the driving current decreases linearly with N. Under 5 W of input power, the simulated LED with N=50 showed ~240% enhancement in WPE droop compared to modeled reference commercial LED. Cascading LEDs also decreases joule heating by operating at lower current regime which can enable high power operation of nitride LEDs for high brightness applications.

3.4 Cascading Light Emitting Diodes using InGaN Tunnel Junctions

3.4.1 1st Generation Cascaded LEDs (Heavy Mg-doping)

3.4.1.1 Green (bottom) & Blue (top) LED

The epitaxial structure (Figure 3.6a) was grown by plasma assisted molecular beam epitaxy on free-standing n-type GaN substrates. The device consisted of 50 nm Si:GaN of 5 x 10^{18} cm^{-3} grown at 700 ^{o}C under Ga-rich conditions followed by 3-quantum well / Si:GaN barrier of 3 nm $In_{0.25}Ga_{0.75}N$ / 7 nm Si:GaN (5 x 10^{18} cm^{-3}) grown at 590 ^{o}C. Then, Mg:GaN of 6x10^{20} cm^{-3} grown at 580 ^{o}C under Ga-rich conditions The excess Ga metal was thermally desorbed to obtain a dry surface before the growth of 5 nm $In_{0.3}Ga_{0.7}N$ at a growth temeprature of 570 °C under In-rich conditions. InGaN layer is immediately followed by 10 nm Si-doped GaN of 2 x 10^{20} cm^{-3} and Si-doped GaN layer for 340 nm with a doping concentration of 5 x 10^{18} cm^{-3}. Then, 3-quantum well / Si-doped GaN barrier of 3 nm $In_{0.18}Ga_{0.82}N$ / 7 nm Si-doped GaN (5 x 10^{18} cm^{-3}) was grown at 620 °C followed by p-GaN, InGaN tunnel junction and nGaN layers.

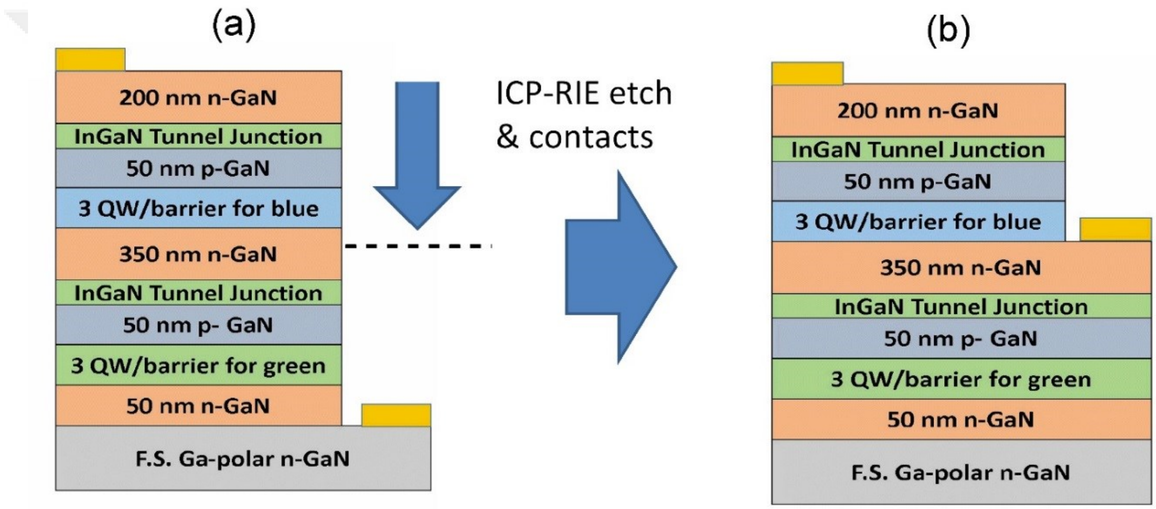

Figure 3.6: (a) Epitaxial stack of the 1st generation Green (bottom) – Blue (top) cascaded LED (b) Probing the top blue LED after ICP-RIE etch and ohmic contact deposition to the n-GaN below the blue LED.

The device was processed using contact lithography, 100 x 100 μm^2 device mesas were fabricated using Cl_2/BCl_3 etching, and ohmic contacts (to top and bottom n-type GaN) were made using Al/Au metal stack. The processing steps were performed to probe the cascaded green-blue LED (Fig. 3.6a) as well as the individual top blue LED only (Fig. 3.6b). Regarding the cascaded green-blue LED, the ICP-RIE etch was performed to reach the n-GaN substrate followed by bottom contact deposition. To probe the top blue LED, some regions of the sample was isolated only down to the central n-GaN layer below the blue LED. The ohmic metal stack was deposited to characterize the top junction individually.

The I-V measurement of the green-blue and blue-only LED is shown in Fig. 3.7a. Although both devices were measured to be leaky, the turn-on voltage values scales well with the number of the junctions in the device. The forvard voltage was measured to be 5.7 V and 3 V for green-blue and blue-only LED, respectively. Next, the electroluminescence (EL) measurement was performed for both devices as shown in Fig. 3.7b. As expected, the designed blue-green LED had two dinstinct emission peaks blue at 456 nm and green at 495 nm. The EL spectrum of the blue-only LED showed a single peak at 450 nm, as expected. However the absolute radiative power was found to be 1.3 μW at 30 mA which is very low ,probably due to high dislocation density in both active regions and/or un-optimized pGaN layer. The results are further discussed in the next section with the comparison of the characteristics of the blue (bottom) – green (top) LED grown under identical conditions.

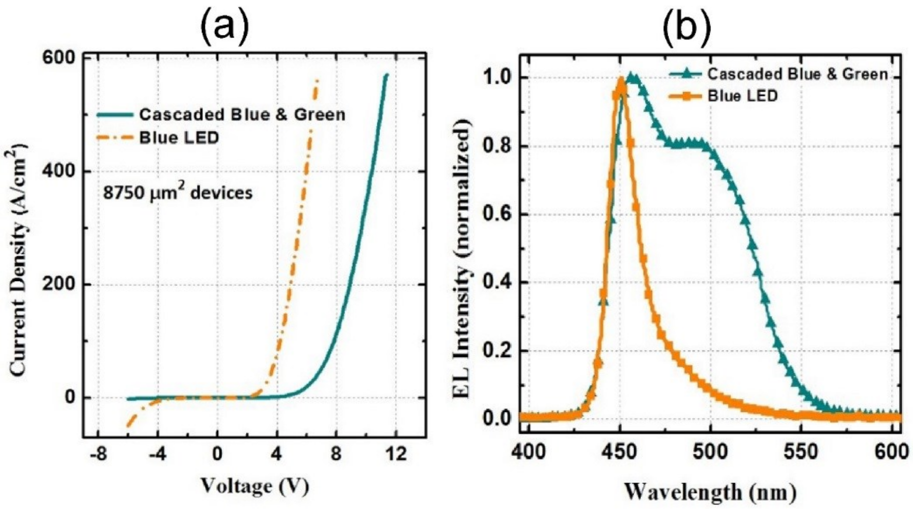

Figure 3.7: (a) The I-V measurement of the cascaded blue-green and blue-only LEDs, showing turn-on voltate ~5.7 V and 3 V, respectively. (b) Correspoding electro-luminescence spectrum of the devices with dual peak emission for blue-green and single peak blue emission for blue-only device.

3.4.1.2 Blue (bottom) & Green (top) LED: The comparison with Green (bottom) & Blue (top) LED

The device described in section 3.4.1.1 was modified such that blue emitting junction was grown at the bottom and active region for green emission was grown on top. The growth conditions of the entire structure was kept same for all layers. The entire blue-green LED was processed rather than investigating the individual junctions.

The I-V measurement of the 1st generation blue-green and green-blue LEDs are shown in Fig. 3.8a. It can bee seen that both LEDs had high leakage current however the blue-green LED has a sharper turn-on with higher rectification. The EL data is shown in Fig. 3.8b for these LEDs. There is ~ an order of intensity difference in blue emission, whereas the green spectra had similar intensity. The radiative output power was measured as 40 μW at 30mA for the blue-green LED which is much higher than green-blue LED (1.3 μW), however still much lower than the mW range. The difference in emission properties can also be seen in optical microscope images of forward-biased devices at 30 mA shown in Fig. 3.8 (c) and (d) for green-blue and blue-green LEDs. The green-blue LED has highly non-uniform emission pattern, whereas blue-green LED showed relatively uniform and brighter emission. However, there are still dark spots (non-uniformity) in the blue-green LED emission (Fig. 3.8d). Since the devices had identical growth parameters except for the order of the LEDs, the following can be councluded from the comparison of these experiments. Firstly, green LED whether grown on bottom or top, emitted very low intensity which may be due to inherent issues with the MBE growth of the active region with high Indium content. Secondly, the blue active region grown on the top of green LED showed much lower intensity . This implies that the epilayers grown below the top blue LED such as heavily Mg-doped ($6x10^{20}$ cm^{-3}) pGaN, InGaN TJ layer etc, generated extended defects which actsas non-radiative recombination centers in this layer. Lastly, the non-uniformity and low radiative power (40 μW at 30mA) of the blue-green LED can be related with non-uniform hole injection due to un-optimized pGaN growth ($Mg=6x10^{20}$ cm^{-3}).

In the next section, experiments on the optimization of p-GaN is discussed in conjunction with hole injection and defect generation.

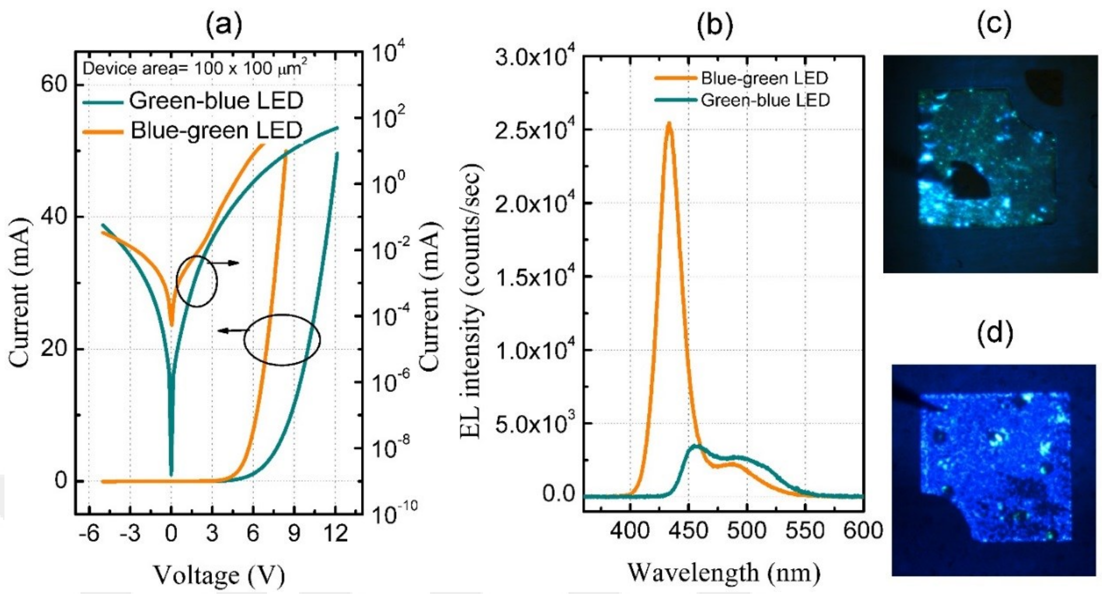

Figure 3.8: (a) I-V and (b) EL measurement of the 1st generation green (bottom)-blue (top) and blue (bottom)-green (top) LEDs. The optical microscope images of (c) green-blue and (d) blue-green LEDs at 30 mA.

3.4.2 Optimization of p-GaN layer as a hole supplier and a burried layer

In the previous section, it was pointed out that cascaded LEDs had some issues. In this experiment, the p-GaN growth conditions were varied in test structures. In a conventional LED, the only criteria for p-GaN layer is to supply the highest hole density with high carrier mobility for current spreading. However, in cascaded LEDs this criteria is not sufficient. The p-GaN layer is buried below another emitting active region, thus nucleation of extended defects and memory effect needs to be avoided in cascaded LEDs. Since memory effect is not an issue in MBE growth, the problem simplifies to the possiblity of nucleation of defects in p-GaN layer.

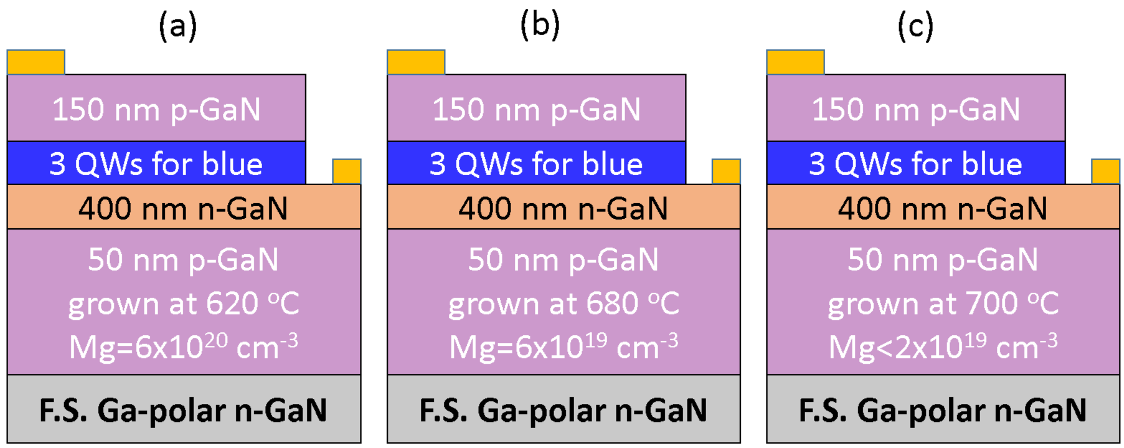

Figure 3.9: Epitaxial designs of the test structures for p-GaN optimization for both hole supplier and burried layer below an LED. The test devices of (a) sample A, (b) sample B and (c) sample C.

A series of test samples shown in Fig. 3.9 were designed and grown. It can be seen that a 50 nm pGaN layer is grown with varying Mg doping and growth temperature below the conventional LED stack.. On top of the quantum well/ barrier layers 150 nm of pGaN layer was grown under the same conditons as the bottom p-GaN layer. In these test structures, bottom p-GaN layer was designed to test the nucleation of extended defects and the top p-GaN layer works as hole injector as in conventional LEDs. In these series of p-GaN samples, Mg-flux was kept same but the substrate temperature varied which results in lower Mg-doping with increasing substrate temperature due to the desorption of Mg-atoms from the sample surface before incorporating in to the GaN lattice. The test samples had p-GaN layers with Mg concentration (growth temperature) of $6\text{x}10^{20}$ cm^{-3} (620 °C) for sample A, $6\text{x}10^{19}$ cm^{-3} (680 °C) for sample B and $6\text{x}10^{20}$ cm^{-3} (700 °C) for sample C.

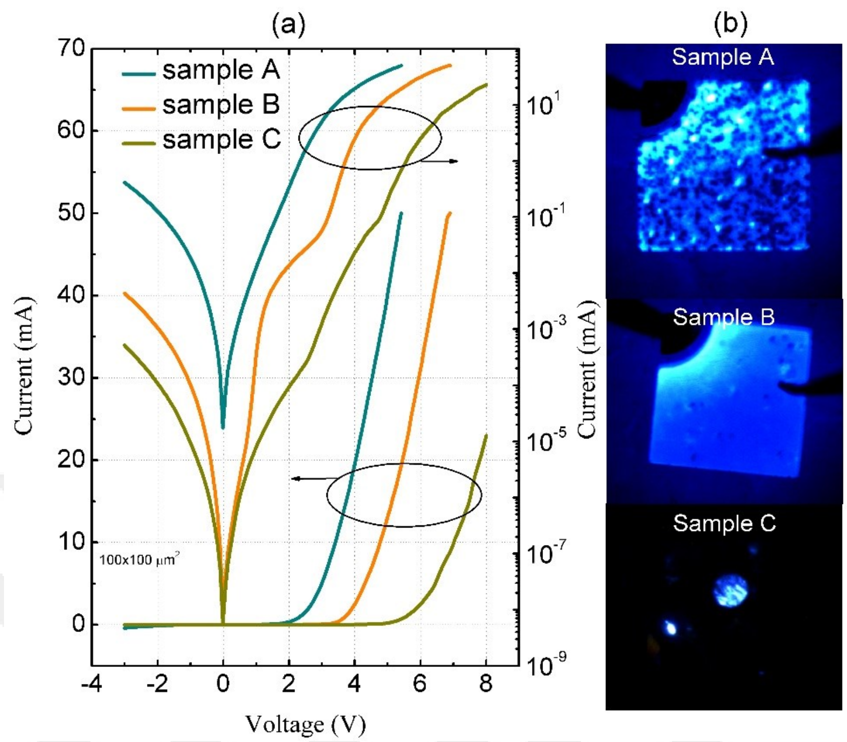

Figure 3.10: (a) I-V measurement and (b) optical microscope images (at 30 mA) of the test structures for p-GaN optimization.

The I-V characteristics of samples A, B and C are shown in Fig. 3.10a. It can be seen that sample A had poor rectification and low shunt resistance (high current leakage) and soft turn-on probably due to high density of dislocations which nucleated in the p-GaN layer below the active region with a heavy Mg doping of 6×10^{20} cm^{-3} grown at low substrate temperature (620 ^oC). Sample B showed sharp turn-on with much reduced current leakage which is the desired characteristics from a proper LED. And sample C showed even lower current leakage (high shunt leakage) and a soft turn-on at much higher forward bias. The optical microscope images at 30mA forward current for the samples are shown in Fig. 3.10b. It can be seen that sample A showed non-uniform light emission with a radiative output power of 30μW at 30 mA. Whereas, sample B showed uniform emission with output power of 150 μW and Sample C had almost no light output. The I-V data, microscope images and output power values are in excellent agreement to show the optimum pGaN growth condition found at a Mg doping of $6x10^{19}$ cm^{-3} at a growth temperature of 680 ^{o}C. For the rest of the cascaded LEDs in this thesis, the growth conditions of the p-GaN layer developed in this section were used.

3.4.3 2nd Generation Cascaded LEDs (optimum p-GaN)

3.4.3.1 Green (bottom) & Blue (top) and Blue (bottom) & Green (top) LEDs

In the section 3.4.2, the optimum growth conditions for p-GaN layer was reported. The green-blue and blue-green LEDs (reported in section 3.4.1.1 and 3.4.1.2) were regrown using the optimum pGaN layers.

The I-V characteristics areshown in Fig. 3.11a. It can be seen that both green-blue and blue-green LEDs had relatively similar current leakage, rectification and turn-on voltage characteristics conpared to the devices shown in section 3.4.1.2 (Fig. 3.8a). However, the blue-green LED showed slighly sharper device turn-on and lower shunt leakage. This might be due to detrimental effects of green LEDon blue LED when it is grown at the bottom. The EL characteristics shown in Fig. 3.11b, validates this hypothesis. It can be seen that there was tremendous difference in emission characteristics of the devices. Blue-green LED showed very bright and uniform emission patterns (Fig. 3.11d). The output power at 30 mA was measured as 1 μW and 350 μW for green-blue and blue-green LEDs, respectively. Compared to 1st generation devices the green-blue LED showed similar power output whereas, the output power of blue-green LED showed ~ an order of magnitude increase in the 2nd generation. From these results following can be concluded; (1) Green active region still shows poor output power even after p-GaN optimization. (2) There is detrimental effects of burried layers to the blue LED on the top. Since optimized p-GaN layers already shown to have negligible effect on characteristics of the LED grown on top (section 3.4.2), the critical epitaxial layers can be listed as InGaN tunnel junction layer, InGaN / Si:GaN quantum well/ barrier emitting layers. In the next sections, the green active regions are not investigated to further simplify the structure for better analysis, and hence growth of high-brightness blue emitting layers was focused upon.

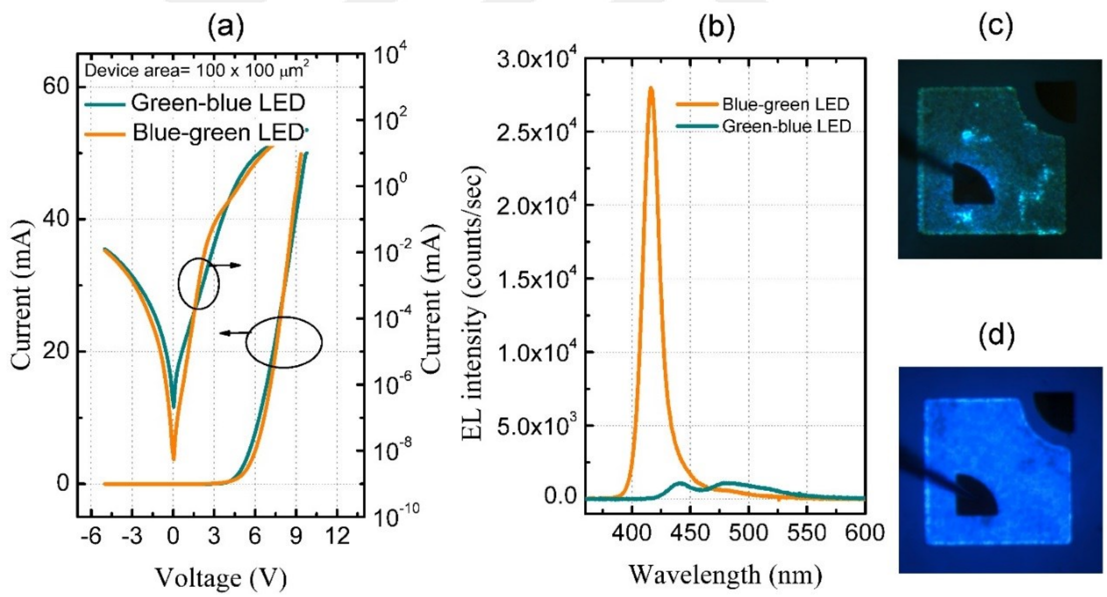

Figure 3.11: (a) I-V and (b) EL measurement of the 2nd generation green (bottom)-blue (top) and blue (bottom)-green (top) LEDs. The optical microscope images of (c) green-blue and (d) blue-green LEDs at 30 mA.

3.4.4 Investigation of the number of the quantum well / barriers on cascaded LED performance

The active regions of the LEDs was designed to be three periodes of InGaN/GaN quatum well/barrier in the previous sections. In this section the two extreme cases of number of periodes will be investigated; single quantum well (SQW) and 8-quantum wells (8QWs). The devices were grown with the epitaxial stack shown in Fig. 3.12a and b. The details of the growth conditions were metioned in section 3.3.1.1. It can be seen that each device had tree active region blue LEDs connected with 3 nm InGaN polarization engineered tunnel-junctions.

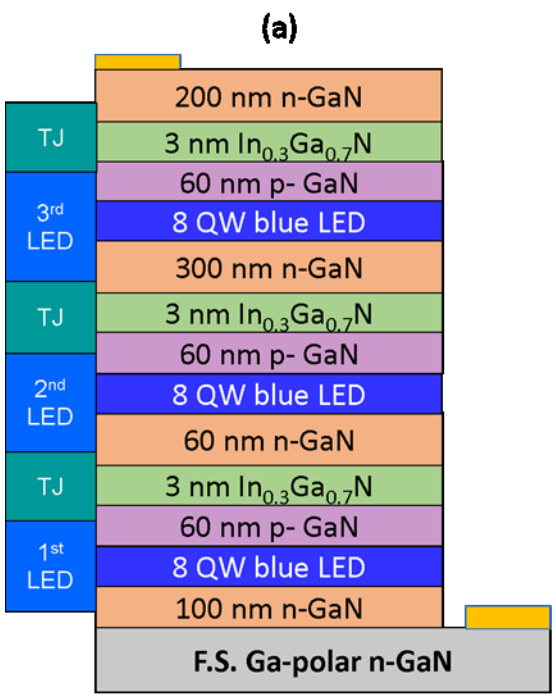

Figure 3.12 The epitaxial design of the three-active region devices with (a) single and (b) 8- quantum well active region.

The I-V characteristics of the 100 X 100 μm^2 devices are shown in Fig.3. 13a. It can be seen that 8-QW LED has two-different diode turn on points, first at 3 V and second ~6 V. Since there are three active regions cascaded, a turn-on voltage ~9 V is expected. Such characteristics imply that the bottom junction was a rectifying diode, the middle junction was a leaky diode, and the top junction was completely shorted. One can conclude that after each active region, there is an increase in extended defect density which makes the 2nd junction leaky and top junction completely shorted. The SQW device showed similar characteristics, but with a turn-on voltage at 6 V which implies that the bottom and middle junctions were rectifying whereas the top is completely shorted. The devices with 30 X 30 μm^2 mesa area were also measured (Fig.3.13b). It can be seen that 8-QW device showed very similar characteristics compared to the 100 X 100 μm^2 case, whereas the SQW device showed the expected diode turn-on voltage (~9V). Such improvement is attributed to lower density of shunt paths in smaller devices. Further structural analysis needs to be done to understand the phenomenon. The shunt leakage of the SQW was much lower compared to 8-QW device which can be seen in semi-log IV plot in Fig. 3.13b. This indicates that the SQW device had less shunt paths (dislocations) compared to 8-QW LED which enables proper rectification in this diode. Such enhancement indicates that multiple InGaN/GaN quantum well / barrier which are grown at substrate temperature of 620 ^{o}C, nucleates higher density of shunt paths compared to the SQW device.

The EL spectra is shown in Fig. 3.13c for both devices. It can be seen that the devices had single emission peak at 405 nm (FWHM = 19 nm) and 425 nm (FWHM = 18 nm) for 8-QW and SQW respectively. The difference in the wavelength of emission peak can be a result of a slight difference in growth temperature or Ga-flux. The radiative output power of the devices were measured as 450 μW and 600 μW at 30 mA. The optical microscope images of forward biased 8-QW and SQW devices are shown in Fig. 3.13d. Both devices showed uniform emission patterns as expected.

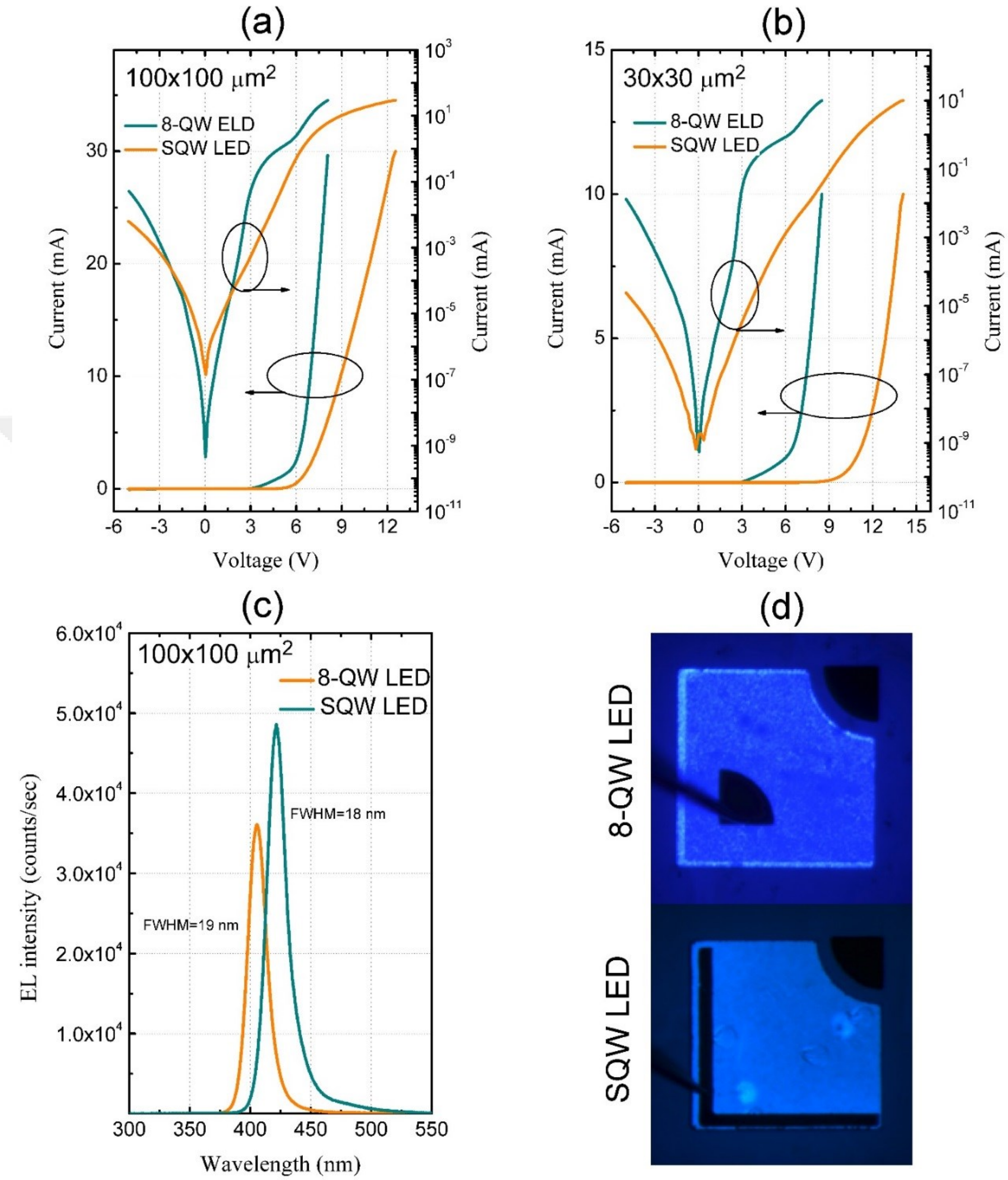

Figure 3.13: I-V measurement of the three junction cascaded LED with 8-quantum wells and single quantum well in each active region with diode mesa area of (a) 100 x 100 μm^2 and (b) 30 x 30 μm^2. (c) Electro luminescence spectrum and (d) optical microscope images of the devices.

In conclusion, high shunt leakage was observed from both of the large area three-active region devices of 8-QW and SQW. However, small area SQW device showed rectifying diode characteristics with lower shunt leakage and turn on voltage at ~9 V. The enhancement is attributed to the thin active region (single well) without the incorporation of multiple periods of low temperature-grown InGaN/GaN superlattice. Further characterization of the three junction SQW LED is shown in the next section referred to as 3rd generation.

3.5 3rd Generation: 3-Junction Blue LED

3.5.1 Experimental Approach for Characterization of the 3-Junction Blue LED

The sample in this study was grown on free-standing Ga-polar GaN substrates with a dislocation density ~7 x 10^7 cm^{-2} (obtained from Saint-Gobain) using plasma assisted molecular beam epitaxy (PA-MBE). The epitaxial structure of the device is depicted in Fig. 3.14a. The growth was initiated with a 100 nm thick Si doped (5 x 10^{18} cm^{-3}) GaN layer at a substrate temperature of 710 ^{0}C. Subsequently, the substrate temperature was lowered to 640 ^{0}C for the growth of 2.5 nm $In_{0.15}Ga_{0.85}N$ single quantum well layer followed by 1 nm unintentionally doped (uid) GaN growth without interrupting the growth to prevent decomposition of InGaN. After ramping the temperature to 680 ^{0}C, 15 nm p-$Al_{0.1}Ga_{0.9}N$ followed by 85 nm p-GaN layer was grown with Mg doping of 3 x 10^{19} cm^{-3}. We found that the substrate temperature and Mg concentration during p-GaN growth is crucial to enable the growth of optically active LEDs with high radiative power grown on top of TJs. The substrate temperature was then lowered to 590 ^{0}C to grow 3 nm $In_{0.3}Ga_{0.7}N$ for the TJ. InGaN was followed by 2 nm Si-doped GaN (3 x 10^{19} cm^{-3}) at the same substrate temperature to prevent InGaN decomposition. Then, it is increased to 710 ^{0}C to continue n++ GaN growth for a total thickness of 15 nm which was followed by 85 nm GaN with Si concentration of 5 x 10^{18} cm^{-3}. Then using these growth conditions, the second and third LED & TJ pairs were grown. It should be noted that all GaN and InGaN layers were grown under Ga- and In-rich conditions respectively. Since it is desired to have n-GaN on top of the device for low contact and spreading resistance, the third TJ was realized to flip the top layer from p-type to n-type layer. Conventional fabrication process was then applied to obtain 900 μ^2 device mesa with Al/Ni/Au ohmic contact pads for both top and bottom of the device. We note that the top contact of the device has grid geometry and doesn't include an external conductive layer for current spreading.

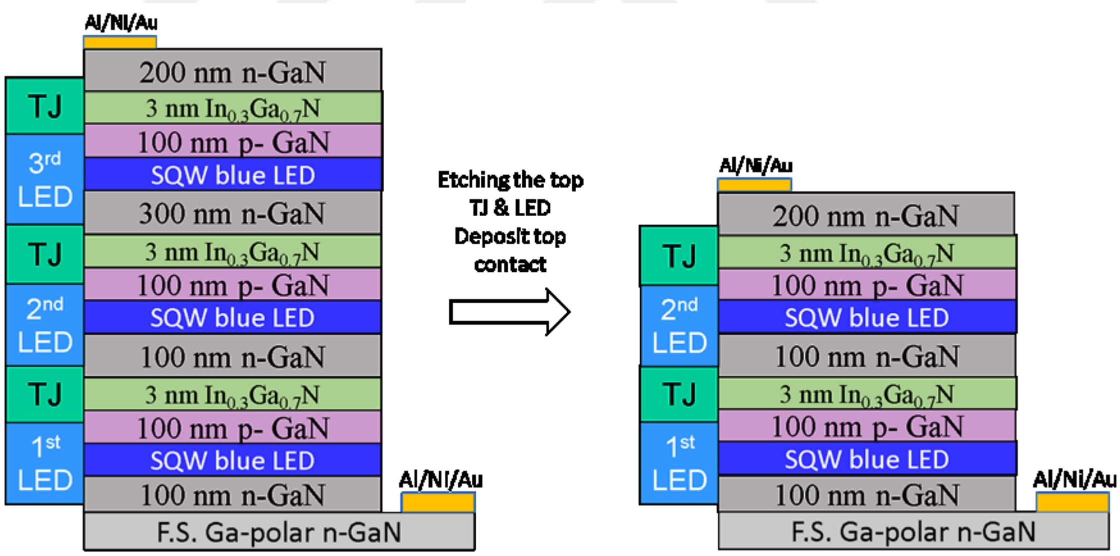

Figure 3.14: The epitaxial stack of the 3-junction blue LED (left) and 2-junction LED obtained by etching the top tunnel junction and LED from the 3-junction device.

The optical power measurements were performed on-wafer using a calibrated Ocean Optics spectrometer coupled with a fiber optic cable. After performing electrical and optical measurements, the top TJ & LED pair was then etched from the device and ohmic contacts were then formed to obtain a dual junction device (Fig. 3.14b). The comparison of the as-grown (3-junction) and etched (2-junction) device enables electrical and optical comparison of the active regions in the device.

3.5.2 Experimental Results and Discussion of the 3-junction Blue LED

The current-voltage (I-V) characteristics measured from the devices are plotted in Fig. 3.15. At an injection current density of 10 A/cm^2, forward voltage values of 9.1 V and 6.07 V were measured for the triple and the dual junction LED respectively. This results in 3.033 V and 3.035 V for each TJ& LED pairs in triple and dual junction respectively. These forward voltage readings show that tunneling mechanism occurs with a negligible TJ turn-on voltage. The differential resistance of the devices was measured as 1.37 x 10^{-3} Ω cm^2 and 7.65 x 10^{-4} Ω cm^2 for triple and dual junction LEDs which are in good agreement with our report on the demonstration of low-resistance InGaN TJs and is suitable for proper adoption in cascaded nitride LEDs.

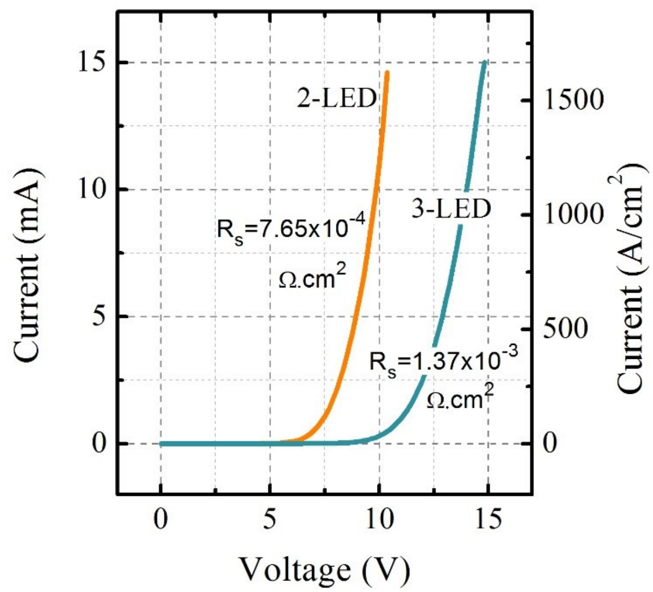

Figure 3.15: I-V measurement of the 3-junction LED and 2-junction LED showing 9.01V and 6.07V at current of 10 A/cm^2

The normalized electroluminescence (EL) spectra of pre-etch (triple junction) and post-etch (dual junction) LEDs at a drive current of 10 mA is shown in Fig. 3.16a. It can be seen that both devices had EL peak ~ 421 nm however, the shape of the peaks are not identical. The Fig. 3.16b shows the semi-log plot of the absolute EL spectrum of the devices which clearly shows that the EL intensity of both devices for $\lambda > 460$ nm are almost identical and EL peak intensity is much higher for triple junction LED. This shows that the top LED is optically active and contributing to light output and it has negligible emission intensity for $\lambda > 460$ nm.

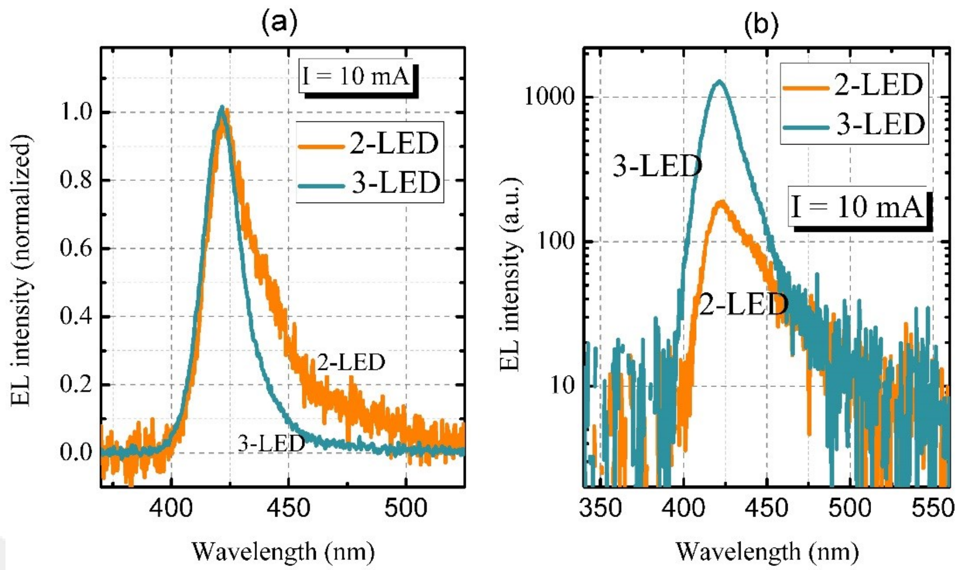

Figure 3.16: The EL spectra of 3-LED and 2-LED devices in (a) linear and (b) semi-log scale.

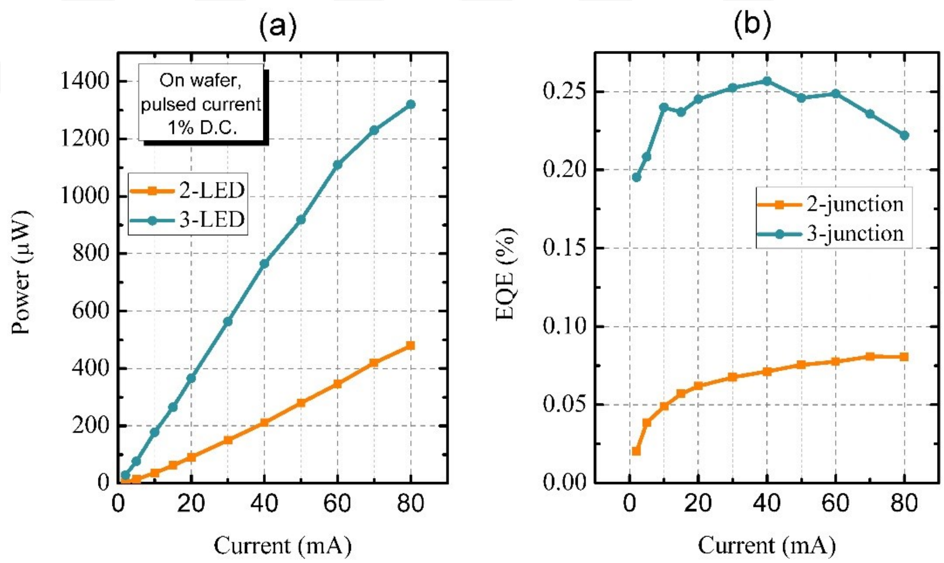

Figure 3.17: (a) The radiative output power and corresponding external quantum efficiency curves as a function of current for3-LED and 2-LED devices.

Although the growth of successive LEDs was performed under identical conditions, the contribution of each LED junction to the light output was found to be non-uniform. Fig.

3.17a shows on-wafer luminescence power output of the devices, measured from the top of the sample using pulsed current with 1% duty cycle and 1 ms pulse width. It can be seen that at 40 mA, 3-LED device emitted around 800 μW, whereas 2-LED device delivered 200 μW. This indicates that 600 μW was contributed from the top most (3rd) LED in the operation of 3-LED device. The external quantum efficiency variation with input current is shown in Fig. 3.17b. Since each active region didn't show identical optical emission properties, the curves are far from the desired characteristics which was discussed in Fig. 3.5c. Neverthless, this might me an inherent issue in MBE grown LEDs and the experiment reported here showed the possibility of cascading optically active LEDs up to 3- junctions using InGaN TJs with low voltage drop.

3.5.3 Conclusions

The first three-junction cascaded nitride blue LED was demonstrated using low resistance InGaN TJs. Triple junction LED operated at 9.1 V under 10 A/cm^2 with a differential resistance of 1.37 x 10^{-3} Ω cm^2. By comparing with the dual junction LED (obtained by etching the top LED&TJ from the triple junction device), we have shown that each of the cascaded LED junctions are optically active. However, the contribution of individual LED active regions to the luminescence output was found to be non-uniform. This is under investigation and might be an inherent issue in PA-MBE growth of LEDs. This proof of concept demonstration using highly conductive polarization-engineered tunnel junctions can enable future cost-effective III-nitride general lighting and multi-color LEDs.

Chapter 4

GaN Tunnel Homo-junctions

4.1 Stand-alone GaN Tunnel Homo-junctions with Repeatable Negative Differential Resistance

4.1.1 Motivation behind GaN homo-junction tunneling diodes

III-Nitrides have been very useful in wide range of applications, particularly in optoelectronics. Despite the commercialization of light emitting diodes (LED), it still faces some challenges mainly due to low hole concentration and mobility. Currently, (semi)transparent conductive oxides (TCO) are in use for the most of the LEDs to spread injected current in p-layer. However, it is desired to replace resistive and lossy TCO layers with a conductive, low-contact resistance, transparent n-type GaN layer. To achieve the conversion of p- to n-type layer, realization of a tunnel junction (TJ) is required. Also, multiple active regions of LEDs (TJs reverse biased) and solar cells (TJs forward biased) can be cascaded in order to operate with higher device efficiency. [100] Low-resistance TJs for GaN were first realized using InGaN/GaN polarization engineered hetero-structures to decrease the tunneling width and barrier. [78, 92] Another approach was to insert GdN nano-islands at the p+ / n+ GaN interface to decrease the tunneling width. [92] Both approaches were realized using relatively low Si and Mg doping concentrations, in the range of 5×10^{18} - 5×10^{19} cm^{-3} and 1×10^{19} - 5×10^{19} cm^{-3}, respectively.

Very recently, a GaN TJ was demonstrated in an NPN device grown by ammonia MBE using heavy Si (2 x 10^{20} cm^{-3}) and Mg (1 x 10^{20} cm^{-3}) doping across the depletion region, thus showing that no other materials are needed for the device if the junction is heavily doped. [101] Similarly, a GaN TJ has been used in an m-plane vertical-cavity surface-emitting laser (VCSEL) grown by the combination of metal-organic chemical vapor deposition (laser emitting layer) and ammonia MBE (TJ layer). [102] However, these reports only characterize the GaN TJ in reverse bias and lacks detailed investigation of doping concentration on device characteristics.

Here, we first fabricate PA-MBE grown stand-alone GaN TJs with varying doping density to investigate both forward and reverse bias operation as a function of Si and Mg doping concentration. Then, we discuss about the observation of negative differential resistance (NDR) in these devices. Further, the characteristics of reverse biased TJ was investigated in a separately fabricated NPN diode.

4.1.2 Experimental Design of GaN Stand-alone Tunnel Junctions

Fig. 4.1 depicts the epitaxial stack of the stand-alone TJ series. The growth initiated with 100 nm GaN with Si doping of 4 x 10^{19} cm^{-3} on MOCVD grown free standing GaN (dislocation density ~3 x 10^{7} cm^{-2}, Si doping ~ 3 x 10^{18}). The TJ layer was formed with10 nm n++ and 20 nm p++ GaN. The Si & Mg doping concentrations were designed as 2 x 10^{20} cm^{-3} & 3 x 10^{20} cm^{-3} for sample A, 4 x 10^{20} cm^{-3} & 3 x 10^{20} cm^{-3} for sample B and 4 x 10^{20} cm^{-3} & 5 x 10^{20} cm^{-3} for sample C, respectively. The TJ layer followed by a 180 nm p+GaN and 20 nm p++GaN layer with Mg doping of 1 x 10^{20} cm^{-3} and 3 x 10^{20} cm^{-3}, respectively. The p-GaN layers were grown under Ga-rich conditions [103] with a stable

In metal was present on the growth surface to enhance the lateral adatom mobility. [104, 105]

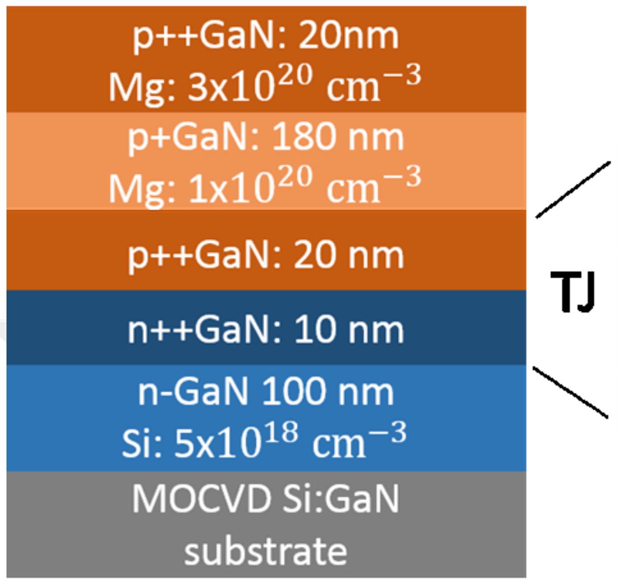

Sample	Si-doping (cm^{-3})	Mg-doping (cm^{-3})
A	$2x10^{20}$	$3x10^{20}$
B	$4x10^{20}$	$3x10^{20}$
C	$4x10^{20}$	$5x10^{20}$

Figure 4.1: Epitaxial design of the stand-alone sample series with varying Mg and Si doping concentration in the tunneling layer.

We note that all Si-doped GaN layers were grown at 700 °C under Ga-rich conditions showing streaky pattern in reflective high energy electron diffraction (RHEED) indicating two-dimensional growth. Also, all p-GaN layers were grown under Ga-rich condition with In metal present on the growth surface at a growth temperature varying between 610 °C and 680 °C using a Mg beam equivalent pressure of 1 x 10^{-8} Torr. The Si and Mg doping concentration were calibrated with secondary-ion spectroscopy measurements on two separate doping calibration growth stacks which are not shown here.

All samples were processed using standard optical lithography techniques. The stack of Ni (4 nm) / Au (6 nm) was deposited on the p-GaN layer followed by annealing at a temperature of 450 ^{o}C in O_2 ambient for sample A, B and C. Then, the samples were dry etched to form 70 x 70 μm^2 device mesa area. The bottom contact to the highly conductive n-GaN substrates was formed by pressing down hand-cleaved In-metal on to the n-GaN substrate.

4.1.2 Results of the GaN Stand-alone Junctions

We analyzed the structural quality of the heaviest doped sample C using atomic force microscopy (AFM) and scanning transmission electron microscopy (STEM). The AFM scan over 5 x 5 μm^2 area showed smooth surface morphology with root mean square roughness ~0.5 nm (Fig. 4.2a). Fig 4.2 (b) shows STEM Z-contrast images of the sample. No defect features were observed either at the regrowth interface, or at the interface between the n++ GaN and p++ GaN layers. We conclude that no extended defects were induced at the scale of the measurement (~0.17 μm^2), with a lower bound on the generated defect density of 5.9 x 10^8 cm^{-2}. We still investigate the nucleation of dislocations (if any) with further measurements. Such characterization is crucial for cascaded devices, or any device grown on top of these tunnel junctions.

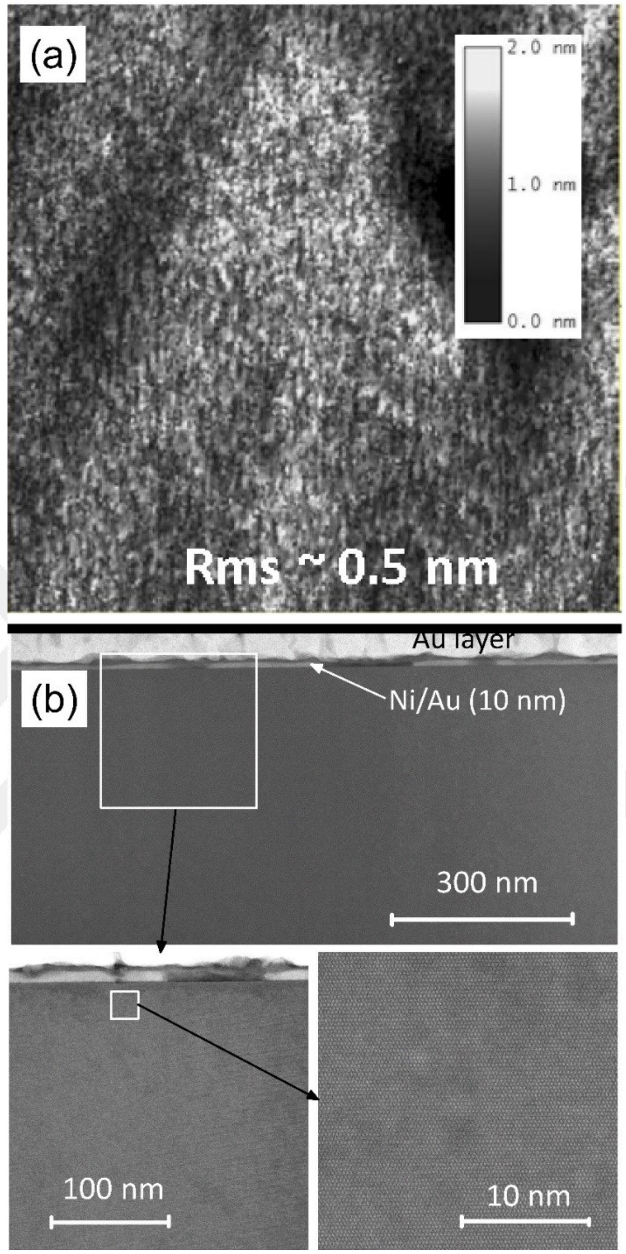

Figure 4.2: (a) The 5 X 5 μm² AFM image of the sample C (heaviest doped stand-alone GaN TJ). (b) STEM Z-contrast images showing no extended defects.

Room temperature (RT) I-V characteristics of the sample A, B and C are shown in Fig. 4.3(a) in both semi-logarithmic and linear scale. It can be seen that sample C has the lowest reverse current and asymmetric forward and reverse current profile near 0 V, whereas sample B and C showed much higher current at forward and reverse bias. At -0.1 V (+0.1 V), sample B and C showed 130X (360X) and 260X (486X) higher current compared to sample A, respectively. As expected, current density increases with higher Si and Mg doping concentration. From the comparison of sample A and B, one can conclude that both forward and reverse tunneling current increases dramatically with increasing Si doping from 1 x 10^{20} cm^{-3} to 2 x 10^{20} cm^{-3} at a similar Mg doping concentration of 3 x 10^{20} cm^{-3}. It can also be observed from Fig. 4.3(a) that both sample B and C showed negative differential resistance (NDR) with a peak current density (PCD) in the range of 150 A/cm^2 to 350 A/cm^2 at a similar forward voltage range from 1.6 V to 2 V at room temperature. The NDR was more pronounced in sample C with peak to valley current ratio (PVCR) of 1.097 compared to sample B (PVCR=1.01) which we attribute to the higher Mg doping in that sample.

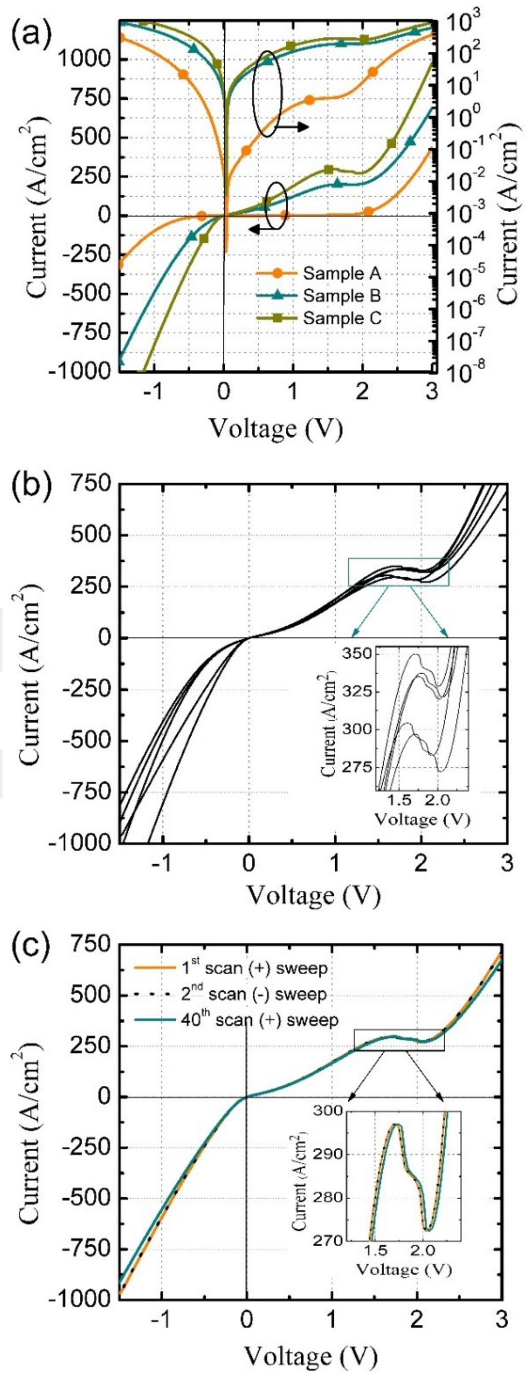

Figure 4.3: Room temperature I-V characteristics of (a) sample A, B, C (device area of 70 X 70 μm^2) and (b) various devices from sample C showing fairly uniform device characteristics over the sample and (c) a device in sample C with positive (+) and negative (-) voltage sweeps and 40th scan showing repeatable characteristics including the NDR region.

We note that such device characteristics were observed from multiple devices in these samples. Fig. 4.3(b) shows various devices from sample C, indicating fairly uniform device characteristics over the sample. The inset of Fig. 4.3b shows the NDR region of these devices. It can be seen that there are plateaus and double humped structures in NDR region which is attributed to the oscillations in the measurement circuit. [106, 107] Such parasitic effect was reported to be fixed by modifying the measurement circuit. Next one of the devices in sample C was measured for multiple scans including positive and negative voltage sweeps (Fig. 4.3c). It can be seen that device has showed highly robust characteristics for these scans at RT. To the best of our knowledge, such characteristics have not been observed from any nitride device with NDR region at RT. We attribute this to ’true GaN’ structure of the device, without using any alloys or nanoparticles.

These stand-alone TJs had p-GaN layer on the top which is usually difficult to make ohmic contacts. The contact resistance and its effects needs to be carefully analyzed to understand the intrinsic characteristics of these devices. Since these devices had very low top-down resistance, the characterization of Ni/Au contacts using a conventional rectangular transfer length method (TLM) pads is not possible (current must flow laterally in p-GaN). Thus, another sample was used which did not include a tunnel junction layer bellow the p-GaN. We note that the p-GaN layer was grown under identical conditions to the p-layer of the stand-alone devices, using Mg doping at 3 x 10^{20} cm^{-3}. The two-terminal I-Vs and the extracted differential resistance of the TLM pads with various contact spacing is shown in Fig. 4.4(a) and (b) for as-deposited contacts and (c) and (d) after contact annealing, respectively. It can be seen that the I-V curves were highly non-linear for as-deposited contact. Upon annealing at 450 ^{o}C under O_2 ambient, the I-V curves showed better Ohmic behavior, however the differential resistance is still slightly higher in low current regime. The extracted contact resistance is 9x10^{-2} ohm.cm^2 and 2x10^{-2} ohm.cm^2 (measured at 0 V) for as-deposited and annealed contacts, respectively.

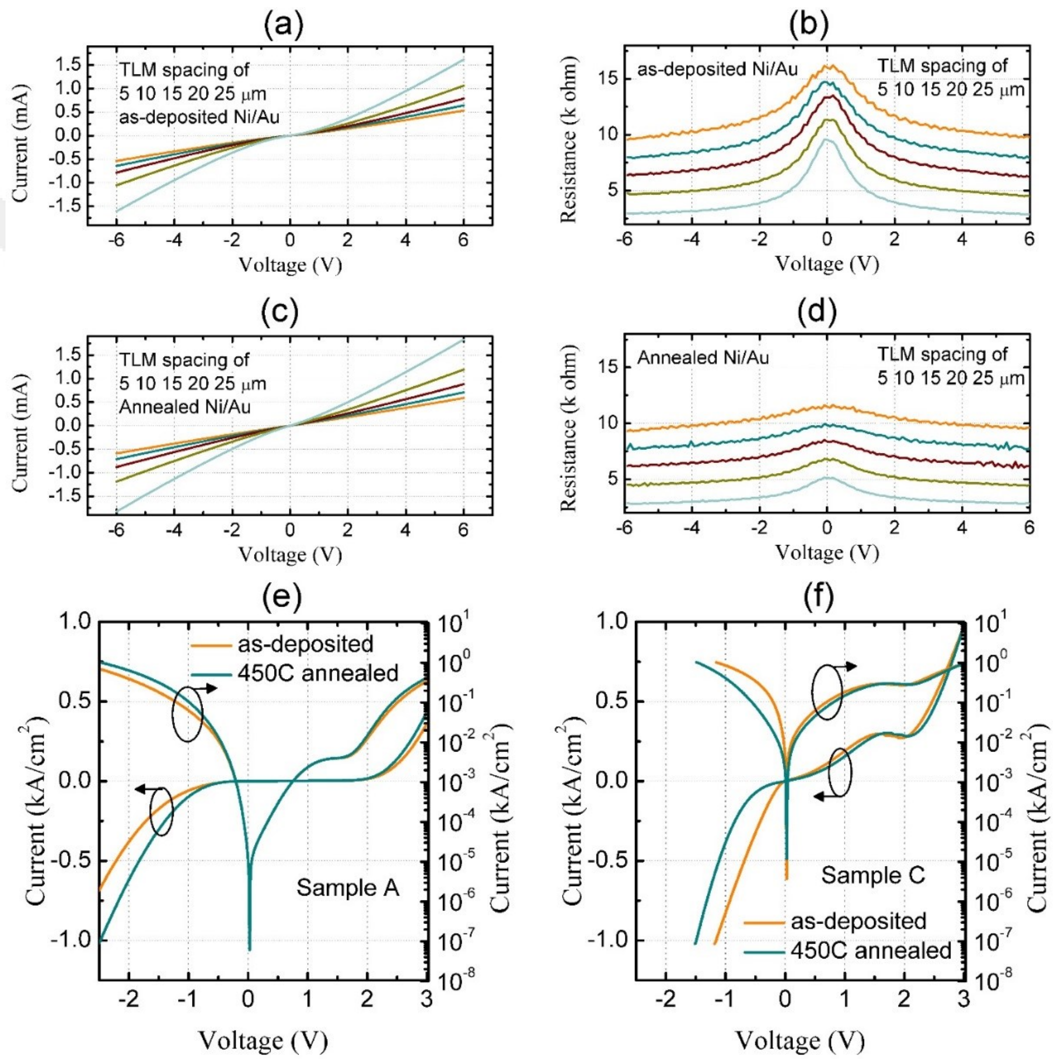

Figure 4.4: Two-terminal I-V measurement & extracted differential resistance of the TLM pads for (a) & (b) as-deposited Ni/Au and (b) & (c) after annealing, respectively. The corresponding I-V characteristics of (e) sample A and (f) sample C.

I-V measurement of sample A and C with as-deposited and annealed contacts are shown in Fig. 4.4(e) and (f), respectively. It can be seen that the devices showed much higher current for the high current range. There was a negligible difference in forward tunneling region (Esaki) of sample C, however especially in Zener region of sample C, the device performance is limited by resistive p-contacts. Since it was observed that even after annealing the contacts showed non-linear I-V, the intrinsic Zener performance was not measured in this device geometry.

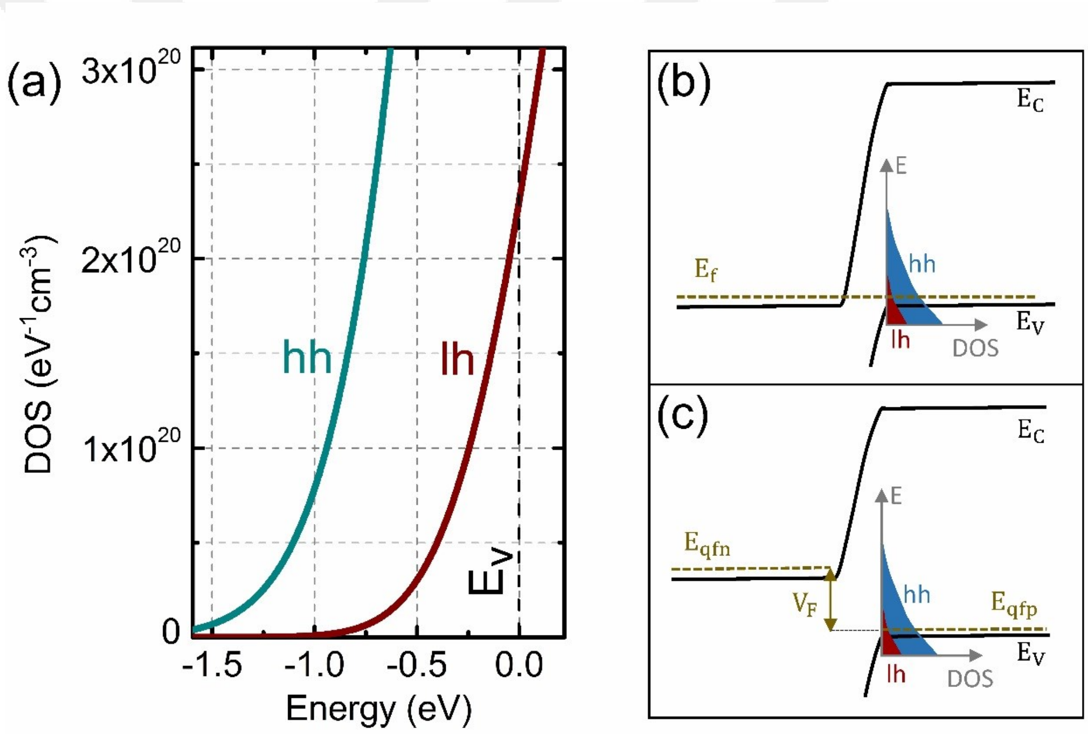

Figure 4.5: (a) Calculated band tail density of states (DOS) of heavy hole (hh) and light hole (lh) bands using Kane's approximation. The schematics of the tunnel junction with tail states under (b) zero and (c) forward bias.

Esaki diodes from various semiconductor material systems typically show peak current density (PCD) at a voltage in the range of 0.1 V - 0.4 V.[24-27] The presence of PCD at higher forward voltage (1.6 – 2 V) was attributed to deep band tail states in heavily Mg-doped (5 x 10^{20} cm^{-3}) GaN. Using Kane's equation, [108, 109] the density of states (DOS) for the light hole (lh) and heavy hole (hh) were calculated assuming an ionized Mg concentration of 1 x 10^{20} cm^{-3} (Fig. 4.5(a)). It should be noted that higher ionization ratio (~50 %) of Mg atoms has been reported for PAMBE grown GaN with heavy (1.2 x 10^{20} cm^{-3}) Mg-doping. [31] Fig 4.5(b) and (c) shows the schematics of a TJ in zero and forward bias, respectively. It can be seen that deep band tail states enable forward tunneling at high forward voltage. We still investigate these tunnel junctions and heavy Mg-doped bulk GaN layers with various measurements to further analyze the mechanism.

4.1.3 Conclusions

Nitride backward (Esaki) diodes were reported with repeatable negative differential resistance for the first time. This achievement was realized by using heavy Si (4 x 10^{20} cm^{-3}) and Mg (5 x 10^{20} cm^{-3}) doping across the GaN p-n junction. Both forward and reverse tunneling current increased with higher doping in the TJ layer. A peak forward tunneling current of 350 A/cm^2 was achieved with the presence of NDR at voltage range 1.6 V – 2 V which might be enabled by deep band-tail states in p++ GaN. The reverse bias characteristics were found to be limited with p-contact resistance. In the next section, further analysis is shown to observe intrinsic reverse bias performance of the tunnel diodes.

4.2 NPN diode with a GaN Tunnel Junction

4.2.1 Motivation for the Design of NPN Diode

As it is mentioned in the previous section, resistive p-contacts limits the GaN tunnel junction performance especially in the Zener region. On the other hand, Ohmic contact to n-GaN is highly conductive and can allow better understanding of the intrinsic device characteristics. To avoid the resistive p-contact, an NPN device configuration was used to take advantage of low-resistance n-type Ohmic contacts to reveal the conductivity of the GaN TJs.

The schematic energy band diagram of the NPN device is shown in Fig. 4.6 under (a) zero, (b) forward and (c) reverse bias. Total voltage across the NPN device is the sum of the voltage drop at the TJ (V_{TJ}), PIN diode (V_{PIN}), p-type and n-type layers (~10^{-5}-10^{-6} ohm.cm^2), and n-type contacts (1-2 x 10^{-5} ohm.cm^2). In the forward bias operation of the PIN diode, the TJ is reverse biased (Fig. 4.6b). Due to the series connection of the TJ and the PIN diode, the applied voltage drops on both for a constant current through the device. As the PIN diode is reverse biased (Fig 4.6c), the current is very low, thus the forward voltage of the TJ and voltage drop on overall device resistance becomes negligible.

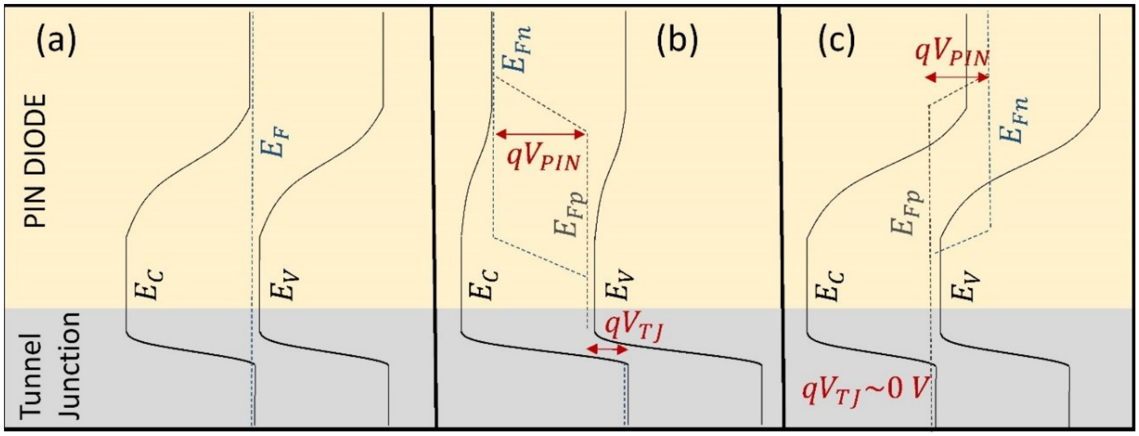

Figure 4.6: Schematic energy band diagram of the NPN device under (a) zero, (b) forward and (c) reverse bias condition of the PIN diode.

4.2.1 Experimental Results of the NPN Diode

The epitaxial design for the NPN diode is shown in Fig. 4.7. The growth of the sample was performed in similar conditions as explained in section 4.1.2. The stack was grown on a similar substrate and composed of a 100 nm GaN layer with Si doping of 5 x 10^{18} cm^{-3} followed by 15 nm unintentionally doped (UID) GaN and a 100 nm Mg-doped GaN with doping concentration of 6 x 10^{19} cm^{-3}. The PIN junction combined with the TJ described in the design of sample B and capped with 150 nm n-GaN (Si=4 x 10^{19} cm^{-3}) and 20 nm n+GaN (Si=1 x 10^{20} cm^{-3}) as current spreading and contact layers, respectively.

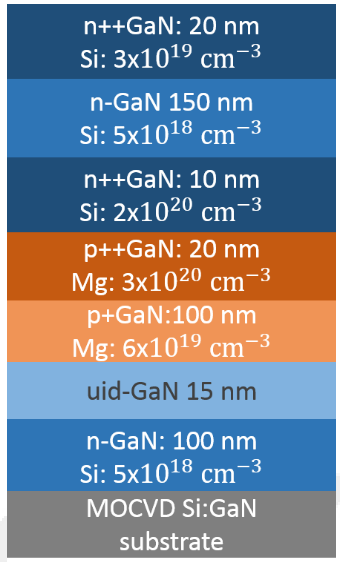

Figure 4.7: The epitaxial design of the NPN device.

Fig. 4.8 (a) shows the I-V characteristics of the 10 X 10 μm^2 diode in semi-log and linear scale. It can be seen that the device has 8 orders of rectification between -4 V and 4 V, indicating decent diode characteristics. The device showed 3 V of forward voltage at 20 A/cm^2 and reached the maximum continuous wave (CW) current density of 150 kA/cm^2 at 7.6 V. We believe these values demonstrate the lowest forward voltage and highest current density operation in any III-Nitride device with a tunnel junction. Fig. 4.8(b) shows the differential resistance of the diode in the forward bias. The differential resistance at current density of 20 A/cm^2, 1 kA/cm^2 and 150 kA/cm^2 were extracted as 9 x 10^{-3} ohm.cm^2, 3.1 x 10^{-4} ohm.cm^2 and 1 x 10^{-5} ohm.cm^2, respectively.

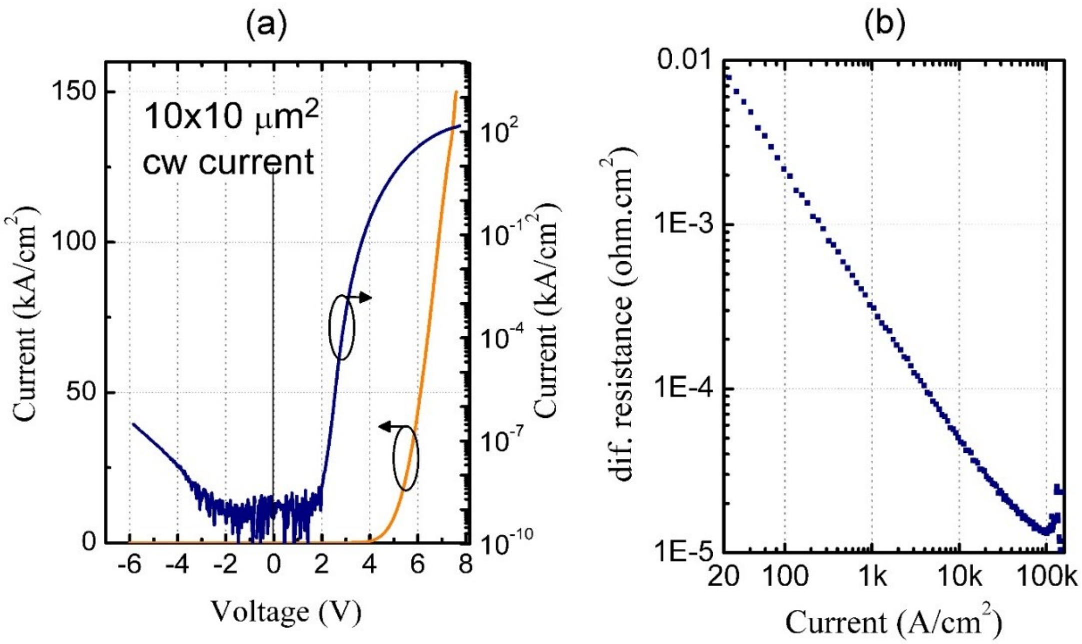

Figure 4.8: (a) The I-V characteristics of the NPN iode in semi-log and linear scale showing 3 V at 20 A/cm^2 and a maximum cw current density of 150 kA/cm^2. (b) The variation of total differential resistance of the NPN diode.

4.2.3 Conclusions

The GaN TJ was integrated with a PIN diode as an Ohmic contact to p-GaN. The NPN test structure had a forward voltage of 3 V at 20 A/cm^2 and could be operated at CW current as high as 150 kA/cm^2 with a total differential resistance of 1 x 10^{-5} ohm.cm^2. To the best of our knowledge, this is one of the lowest differential resistance and highest operation current observed in any Nitride PN diode.

4.3 Study of P-down LEDs with GaN TJs

The superior device performance of LEDs in opposite polarization direction (N-polar p-up or Ga-polar p-down) is discussed in Chapter 2. In this section, Ga-polar p-down structures are discussed.

The p-down Ga polar devices have been investigated and found to have major processing and device problems. Since p-GaN is at the bottom, the p-contact needs to be deposited on the etched p-GaN surface. It has been a long-lasting problem to achieve low resistance Ohmic contacts on dry etched p-GaN surface [112] due to donor like defects generated at the surface. Another problem with this design is the current crowding problem limiting proper device operation due high sheet resistance of p-GaN (low hole mobility) as depicted in Fig. 4.9. [73] These reasons prevented the demonstration of p-down device with comparable performance to p-up device. On the other hand, if a TJ is grown below the p-GaN layer to convert the bottom contact to n-type layer, the those roadblocks can be overcome by having a low-resistance n-type contact and conductive n-GaN bottom spreading layer. The critical component is the tunnel junction which can supply high current at a low reverse bias operation.

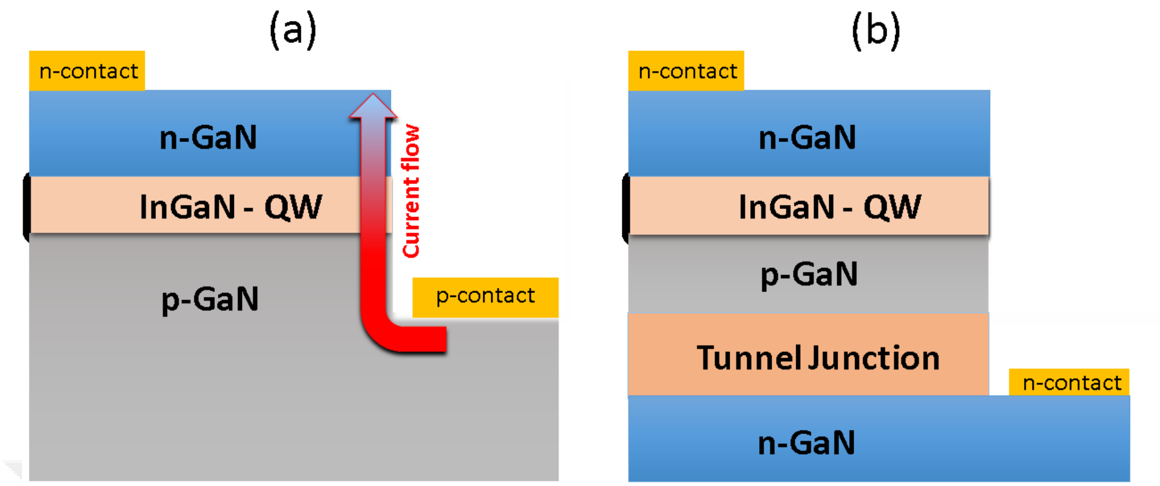

Figure 4.9: The schematic epitaxial design of p-down LEDs (a) without and (b) with a TJ layer at the bottom.

Due to the opposite direction of the polarization field, it is not possible to operate an InGaN polarization engineered tunnel junction in the epitaxial layer shown in Fig.4.9 (b). Whereas, highly conductive polarization independent GaN tunnel homo-junctions can be used to enable this device operation.

The epitaxial design of p-up reference LED and p-down LEDs are shown in Fig. 4.10(b). The MBE growth conditions can be found in section 3.1. The reference LED has the conventional LED design without a TJ layer in p-up geometry. Whereas, p-down LEDs had a TJ layer with Mg concentration of 3 x 10^{20} cm^{-3} and varying Si doping of 1 x 10^{20} cm^{-3} and 4 x 10^{20} cm^{-3} for sample A and B, respectively. The devices we fabricated to obtain 70 X 70 μm^2 mesa area.

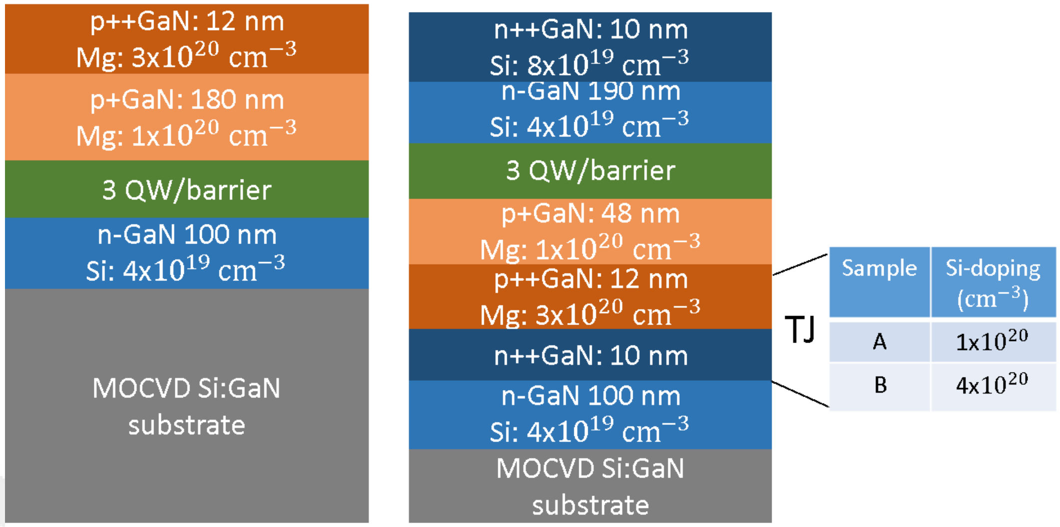

Figure 4.10: The epitaxial design of (a) reference p-up LED and (b) p-down LEDs: sample A and B.

I-V characteristic of the LEDs are shown in Fig. 4.11a. It can be seen that reference LED had lowest shunt leakage of all measured devices while the highest shunt leakage was measured from sample B. This shows that increasing the Si doping in the tunnel junction results in higher leakage. It is well know that shunt leakage increases with extended defect density in the structure. Thus, we attribute this observation to nucleation of new defects with very high Si doping. Plane-view STEM measurements on these samples are under investigation which can reveal the structure of defects in these devices.

It can be seen that the turn-on characteristics of the LEDs agrees well with the characteristics of the stand-alone TJs. A forward current density of 20 A/cm^2 was measured at 3 V, 3.71 V and 2.55V for the reference, sample A and B, respectively. This shows that the Si doping of (sample A) 1 x 10^{20} cm^{-3} is too low for proper TJ operation and Si doping of (sample B) 4 x 10^{20} cm^{-3} results in high leakage in these MBE grown samples.

The optical microscope images (Fig. 4.11b) shows the EL intensity of the samples at 20 mA. The reference LED is brightest and p-down LEDs showed very poor emission. Sample A had slightly higher emission than sample B. This observation agrees very well with the shunt leakage observation from the I-Vs.

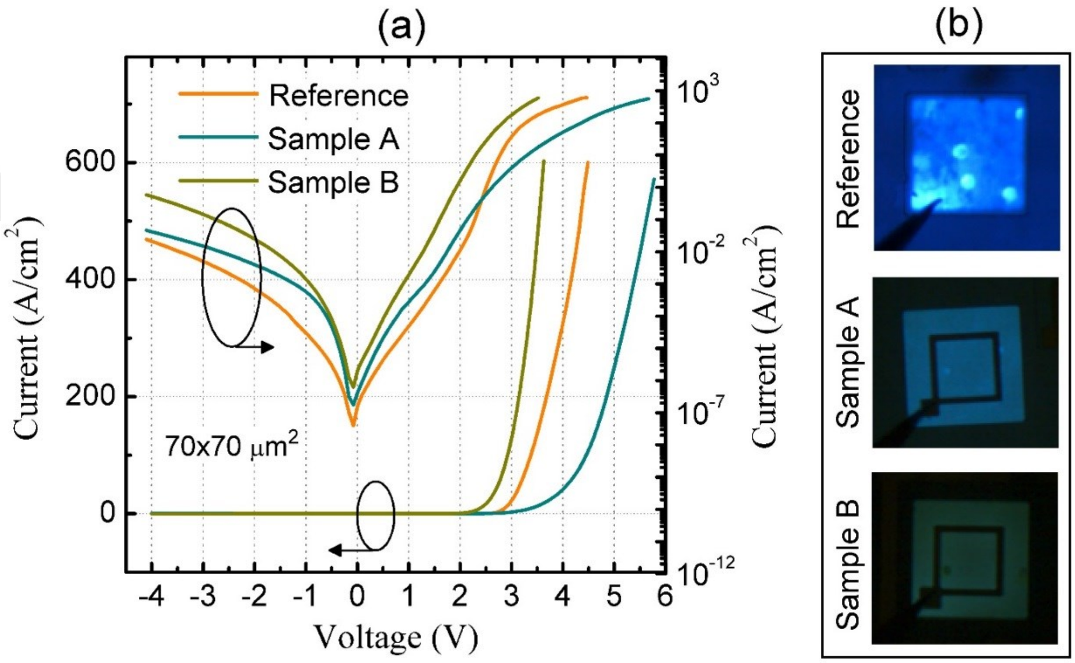

Figure 4.11: (a) I-V characteristics of the reference p-up LED and sample A and B. (b) Optical microscope images of the LEDs at 20 mA.

In conclusion, p-down LEDs were fabricated using GaN tunnel homo-junctions. The p-down LEDs showed increasing shunt leakage with higher Si doping in the TJ, correspondingly the emission intensity was much lower compared to the reference p-up LED. Since MBE LEDs are very sensitive to dislocations in the active region, it is challenging to achieve high power p-down LEDs. Both IV curves and emission properties implies that the p-down devices reported here suffered from the nucleation of dislocation at the TJ layer.

Chapter 5

InGaN Solar Cells towards High Efficiency: Simulations and Experimental Work

5.1 Introduction

The direct energy conversion of photon to electrical energy is called photovoltaic conversion. The process can be simply explained as follows. Incoming photons from sunlight gets absorbed by a solar cell where electron – hole pairs are generated. The epitaxial design of a solar cell is in such a way that, the photogenerated electrons and holes get separated and move towards opposite terminals and this generates an electrical current flow. There are various materials used for solar cell fabrication such as bulk materials, thin films, organic dyes, and organic polymers. Majority of the commercially available solar cells are fabricated using low cost Si bulk semiconductor material, however low cost low efficiency organic-inorganic PV systems have also been investigated. The major goal is to replace the use of fossil fuels for world's emerging energy need. Another application of solar cells is the operation under concentrated sunlight in which sunlight gets focused on a small area expensive high efficiency solar cell. Also, there is a demand for highly efficient radiation hard solar cells for space applications.

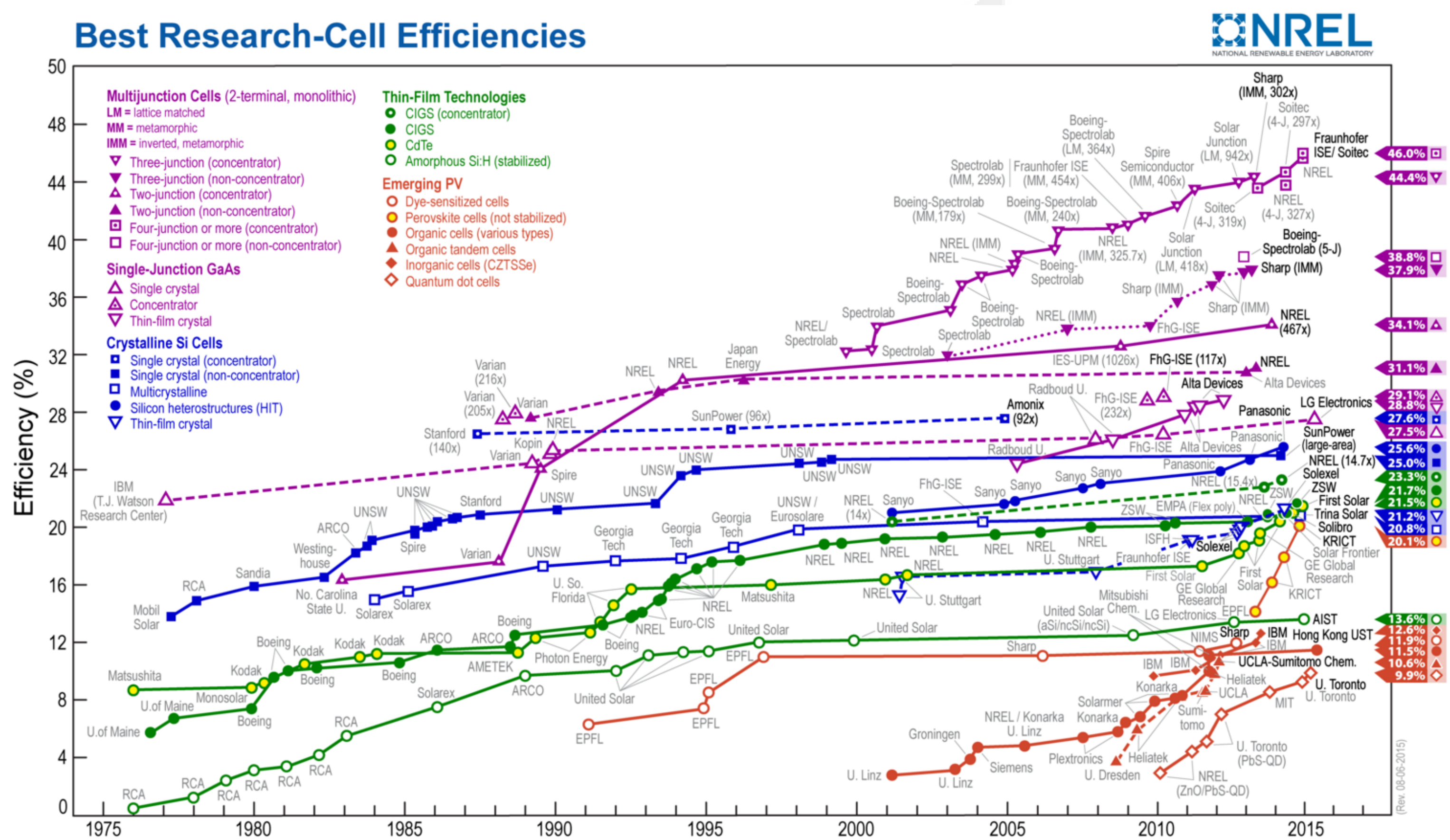

Figure 5.1: Historical developments of best solar cell efficiencies from various materials. Figure courtesy: [www.nrel.gov]

The efficiency improvement of various types of solar cells is shown in Figure 5.1 [112]. It can be seen that most of the solar cell technology is mature with the exception of organic solar cells which targets low cost solar cell application with acceptable high conversion efficiency. Efficiency values as high as 46% has been realized using three junction InGaP/GaAs/GaInAsP/GaInAs-based device under 508-sun solar concentration and is attractive for space and concentrated solar applications. [113]

A single junction solar cell absorbs only the photons with energy higher than the bandgap of the semiconductor. The solar cell is transparent for rest of the photons with energy below the bandgap, and thus are not converted to electrical energy. The photons with energy higher than the bandgap are absorbed. However each photon generates one electron hole pair regardless of its initial energy. The excess photon energy above the bandgap of the semiconductor gets converted to heat in the semiconductor which is device loss mechanism in the device. In the case of a multi-junction solar cells, multiple band gap material are inserted in series to each other using tunnel junctions as shown in Fig. 5.2. The schematic shows three cells connected in series with three different bandgaps. Largest bandgap material is located at the top, medium one in the middle and narrow band gap junction at the bottom. This configuration allows high energy photon absorption in the wide bandgap cell and remaining medium and low energy photons are transmitted to cells below. In the middle cell, medium energy photons are absorbed and low energy photons transmitted to narrow bandgap cell.

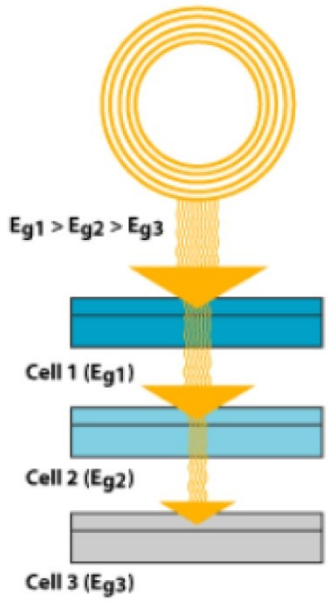

Figure 5.2: Schematic tandem solar cell design of three cells. Figure courtesy: www.reuk.co.uk/Multi-Junction-Solar-Cells.htm

5.2 Nitride Solar Cells

Although conversion efficiency of 46% (506 suns) has been achieved in the III-As/P material system, next generation devices need more junctions to boost the efficiency over 50%. [114-116] Currently, the window (top cell, highest bandgap) cells are designed using InGaP material with a bandgap ~1.8-1.9 eV. However, solar spectrum has photons in the blue and UV spectrum which are now converted inefficiently to electrical energy. Thus, having a high efficiency wide bandgap material-based cell is desired to boost efficiency further. (In)GaN alloy system is one of the promising candidates. InGaN-based blue LEDs have already achieved high efficiency. Thanks to the high value of the absorption coefficient (~ 10^5 cm^{-1}), [115] thin active region is sufficient for light absorption in InGaN-based cells. There have been many reports of InGaN/GaN solar cells using varying device configurations, such as InGaN p-i-n homojunction, n-GaN/i-InGaN/p-GaN and InGaN/GaN multiple quantum wells (MQWs).

InGaN homojunction solar cells have been grown on relaxed GaN layers. Due to the large lattice mismatch between GaN and InN (~11%), the In content and thickness of InGaN layers is limited below the critical thickness for strain relaxation. It is very difficult to achieve high crystal quality thick InGaN active region (~200 nm) to be able to absorb the incident light and generate photo current. Thus, these devices were limited to In content of ~2-5 % in the active region.[118] Further increase in In content drastically reduces device characteristics due to the nucleation of extended defects which work as non-radiative recombination centers, thus killing the diffusion process of the photo-generated carriers. [118]

The solar cells with n-GaN/i-InGaN/p-GaN device geometry has also been widely investigated and shown to have high conversion efficiency. Similar to the InGaN homojunction solar cells, these are also limited to lower InGaN thickness and lower In content. There have been reports with thick InGaN layer layers with low In content giving reasonable device characteristics. [119] However, reaching longer wavelength is required to extend the absorption spectra, achieve higher photo current. Also, these devices suffer from polarization charges at the InGaN/GaN interface. [120] The direction of the electric field in the depletion region turns to opposite direction as the junction gets forward biased, thus the photo current collapses. To recover these detrimental polarization effects both the sides of the InGaN layer should be heavily Si / Mg doped in the nGaN/pGaN layers respectively. [121]. With a proper band engineering, these junctions can achieve high internal quantum efficiency (IQE) [122]. However, thin InGaN layer thickness and low In composition still limits these junctions for the operation at longer wavelength with high external quantum efficiency (EQE).

Multiple quantum well (MQW) InGaN/GaN solar cells have also been reported relatively recently [121, 123, 124]. A typical InGaN quantum well (QW) layer is ~2-3 nm thick. Having 20-30 QWs increase the absorption length of the device and this has been shown to be successful in solar cell operation. The thickness of the GaN barriers between the quantum wells has been reported to be critical for carrier transport which includes thermionic emission as well as tunneling (Fowler-Nordheim type).[124] Thus, GaN barriers needs to be designed thin enough for efficient carrier transport. On the other hand, accumulated strain in the MQWs gets partially released in GaN barriers and this requires thick GaN layers to the balance strain in InGaN QWs. [125] This tradeoff limits the number of the quantum wells in the device which hinders the full absorption of the incident light.

In the following sections, InGaN homojunction solar cell simulation and experimental work on novel nitride solar cell designs are discussed.

5.3 Simulation of 2.3eV InGaN homojunction pin solar cell

5.3.1 Motivation

Having large carrier diffusion length (~few μm) enables proper operation of a solar cell with a simple pn junction design. However, minority diffusion length in GaN has been reported to be much shorter (~0.2 μm) which is a strong function of recombination centers in the material [126]. Because of the large latice mismatch between GaN and InN, material properties degrade for high Indium compositions which results in an even shorter minority carrier diffusion length. Thus, it is necessary to increase the depletion thickness for InGaN solar cells to collect more carriers. One can think of two approaches to realize wider depletion region. First design is to have lighly doped n and p sides in the pn junction. Since the open circuit voltage is a function of doping across the active region, such design delivers low open circuit voltage which is not desirable. Second solution is to have PIN configuration which is realized by inserting an undoped region between the p and n-regions. This way, whicle keeping high p and n side doping, one can also have wide depletion region by having a intrinsic region.

This report simulates a 2.3 eV InGaN homo-junction pin solar cell with varying intrinsic layer thickness and illumination under standard AM0 solar spectrum. Since the actual minority carrier lifetime and mobility for InGaN material is not well-known, the results will be discussed fora range of these material parameters. These results are expected to increase the understanding of the design of InGaN solar cells towards the realization of high efficiency multi-junction solar cells.

5.3.2 Modelling and parameters

We used MATLAB to simulate the output characteristics of InGaN p-i-n solar cells. The designed InGaN p-i-n solar cell is shown in Figure 5.3. The thickness and doping concentration (N_A) of the p-type window layer was chosen to be 70 nm and $5\text{x}10^{17}$ cm^{-3} respectively. N-type base layer was designed as 100nm thick with a doping concentration (N_D) of $5\text{x}10^{18}$ cm^{-3}. Intrinsic layer thickness was varied from 0 to 400nm. The hole mobility was assumed to be 1/100 of the one for electrons. Modified Caughey Thomas theorem was used to find the electron mobility:

$$\mu_e = \mu_{min+} \frac{\mu_{max} - \mu_{min}}{1+(N_A/N_g)^{\gamma}} , \tag{5.1}$$

where μ_{max} , μ_{min} , N_g and γ are semiconductor parameters. Using linear interpolation, the parameters are obtained for $In_{0.3}Ga_{0.7}N$ as 708.8 $cm^2V^{-1}s^{-1}$, 409.7 $cm^2V^{-1}s^{-1}$, $1\text{x}10^7 cm^{-3}$ and 1.26 respectively [127, 128]. The equation was used unless mobility is set constant in the simulation.

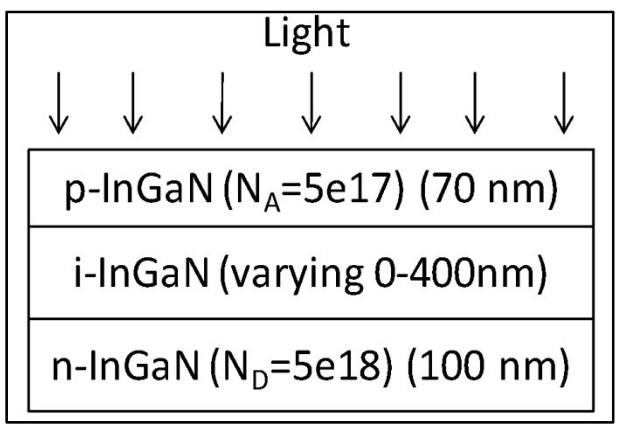

Figure 5.3. The structure of the simulated InGaN homojunction solar cell.

Similarly, linear interpolation between GaN and InN was performed to obtain the constants for relative permittivity, effective density of states in conduction (N_C) and valance band (N_V) for $In_{0.3}Ga_{0.7}N$ which corresponds to the band gap value of 2.29eV (using a bowing parameter of 1.43) [129, 130]. The intrinsic carrier concentration was calculated as 0.593 cm^{-3} from the following equation:

$$n_i = (N_C . N_V)^{1/2}\, exp\left(-E_g/2k_B T\right), \tag{5.2}$$

The minority carrier diffusion length is given by:

$$L = \sqrt{D\tau}\,, \tag{5.3}$$

where τ is minority carrier lifetime which is assumed to be 50 ps unless it is defined for the corresponding simulation [131]. The diffusivity 'D' (cm^2/s) is calculated from Einstein relation:

$$D = (k_B T/\mathrm{q})\,\mu\,. \tag{5.4}$$

The reflection coefficient R is assumed to be 0.2 between air and InGaN interface. The front and back surface recombination velocity $S_{n,p}$ was assumed to be 4000 (cm/s). We used equation (5.5) to calculate the wavelength dependent absorption coefficient $\alpha(\lambda)$ for 30% InGaN and is plotted inFig. 5.4. The parameters of the equation (5.5) were obtained by linear interpolation using the information given in reference [132].

$$\alpha(\lambda) = 10^5\sqrt{2.6763\left(e(\lambda) - E_g\right) - 0.32197\left(e(\lambda) - E_g\right)^2}\,, \tag{5.5}$$

where $e(\lambda)$ is the wavelength dependent energy vector of the standard AM0 spectrum and E_g is the band gap energy (2.29 eV).

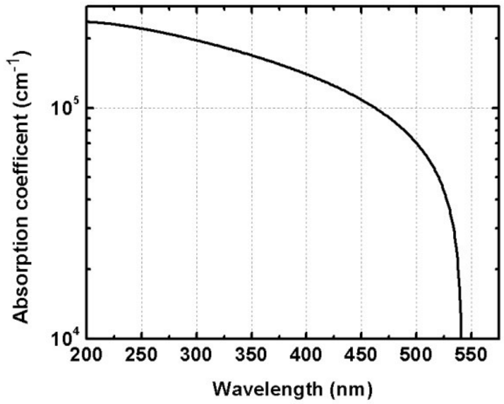

Figure 5.4. Wavelength depending absorption coefficient of $In_{0.3}Ga_{0.7}N$

The electron (j_n) and hole (j_p) diffusion current densities were calculated using the equation (5.6) and (5.7) respectively. [133]

$$j_n = \left(1 - \frac{W_{dep}{}^2}{\mu\tau(V_{bi}-V)}\right)\left(-\frac{q(1-R)b_s\alpha L_n}{(\alpha^2 L_n{}^2-1)}\right)\left\{\frac{e^{-\alpha(x_p-w_p)}\left(\frac{S_nL_n}{D_n}cosh\frac{x_p-w_p}{L_n}+sinh\frac{x_p-w_p}{L_n}\right)-\left(\frac{S_nL_n}{D_n}+\alpha L_n\right)}{\frac{S_nL_n}{D_n}sinh\frac{x_p-w_p}{L_n}+cosh\frac{x_p-w_p}{L_n}}\right. +$$

$$\left.\alpha L_n e^{-\alpha(x_p-w_p)}\right\} + \frac{q(D_n n_0(e^{\frac{qV}{k_bT}}-1)}{L_n}\left\{\frac{\frac{S_nL_n}{D_n}cosh\frac{x_p-w_p}{L_n}+sinh\frac{x_p-w_p}{L_n}}{\frac{S_nL_n}{D_n}sinh\frac{x_p-w_p}{L_n}+cosh\frac{x_p-w_p}{L_n}}\right\}, \tag{5.6}$$

and

$$j_p = \left(1 - \frac{W_{dep}{}^2}{\mu\tau(V_{bi}-V)}\right)\left(-\frac{q(1-R)b_s\alpha L_n}{(\alpha^2 L_n{}^2-1)}\right)\ e^{-\alpha(x_n-w_n)}$$

$$*\left\{\frac{\left(\frac{S_pL_p}{D_p}cosh\frac{x_n-w_n}{p}+sinh\frac{x_n-w_n}{L_p}\right)-\left(\frac{S_pL_p}{D_p}+\alpha L_p\right)e^{-\alpha(x_n-w_n)}}{\frac{S_pL_p}{D_p}sinh\frac{x_n-w_n}{L_p}+cosh\frac{x_n-w_n}{L_p}} - \ \alpha L_p\right\} +$$

$$\frac{q(D_p p_0(e^{\frac{qV}{k_bT}}-1)}{L_p}\left\{\frac{\frac{S_pL_p}{D_p}cosh\frac{x_n-w_n}{L_p}+sinh\frac{x_n-w_n}{L_p}}{\frac{S_pL_p}{D_p}sinh\frac{x_n-w_n}{L_p}+cosh\frac{x_n-w_n}{L_p}}\right\}, \tag{5.7}$$

where W_{dep} is total thickness of depletion region, V_{bi} and V are built-in voltage and diode voltage respectively. b_s is photon flux density and $x_{p,n}$, $w_{p,n}$ are total and depleted thickness of the p and n-regions respectively. Note that the equations are modified by multiplying with an additional term which is '$\left(1-\frac{W_{dep}{}^{2}}{\mu\tau(V_{bi}-V)}\right)$'. It is generally assumed to be equal to '1' since, the recombination in depletion region is neglected. However, recombination process for thick depletion regions should be taken into account since it can be the limiting factor of the device. This term represent the carrier collection probability in the depletion region which could be less than '1'. The light generation current density in the space charge region is also given with the same coefficient by [133]:

$$J_{scr}=\left(1-\frac{W_{dep}{}^{2}}{\mu\tau(V_{bi}-V)}\right)q(1-R)b_{s}e^{-\alpha(x_{p}-w_{p})}. \tag{5.8}$$

Total short circuit current density is calculated by using equation (5.9) [133].

$$J_{sc}=-j_{n}(-w_{p})-j_{p}(-w_{n})-j_{scr}\,. \tag{5.9}$$

Since recombination process in the depletion region dominates the generation-recombination current (J_o), having a wider depletion region in pin diodes requires modified J_o for more accurate modelling. The equation (5.10) was used to obtain dark current density in pin diodes [133]:

$$J_{o}=\frac{\mathrm{q}n_{i}W_{dep}}{\tau}\frac{2\sinh(\mathrm{qV}/2kT)}{q(V_{bi}-V)/kT}\,. \tag{5.10}$$

From this, the diode output current can be calculated as,

$$J=J_{o}-J_{sc}\,. \tag{5.11}$$

The open circuit voltage (V_{oc}) was determined numerically since; the model lacks analytical relation between current and voltage. The efficiency (η) of the solar cell was calculated using equation (5.12):

$$\eta = \frac{J_{sc}V_{oc}FF}{P_{in}}, \tag{5.12}$$

where FF is the fill factor and P_{in} is the power of the incident light. Here, we also used P_{in} as the total power of the absorbed part of the spectrum to get a reference for a multi-junction solar cell operation since~2.3 eV wide band gap solar cell is an ideal window cell material for a tandem cell and would transmit the sun light with energies less than ~2.3 eV.

5.3.3 Results and Discussion

We investigated the effect of intrinsic region thickness on the short circuit current density under varying carrier lifetime and mobility as it is mentioned previously. Figure 5.5(a) and (b) shows such variation and the contribution of depletion region with carrier lifetime and variable mobility, respectively.

It can be seen that having a certain thickness of an intrinsic layer increases the short circuit current density. Secondly, it is observed that more than half of the total current is generated in depletion region (drift current) especially as the intrinsic layer is thicker. When it is shorter, the depletion expands further into p-GaN which decreases the electron diffusion current generated in p-GaN region. Thirdly, it is noteworthy that for high quality materials with minority carrier lifetime (>100 ps) and electron mobility (>500 $cm^2V^{-1}s^{-1}$), the short circuit current density increases over the 400 nm of intrinsic layer thickness. However, as expected, it suffers from extensive increase in the intrinsic layer thickness as the minority carrier lifetime and electron mobility are relatively lower.

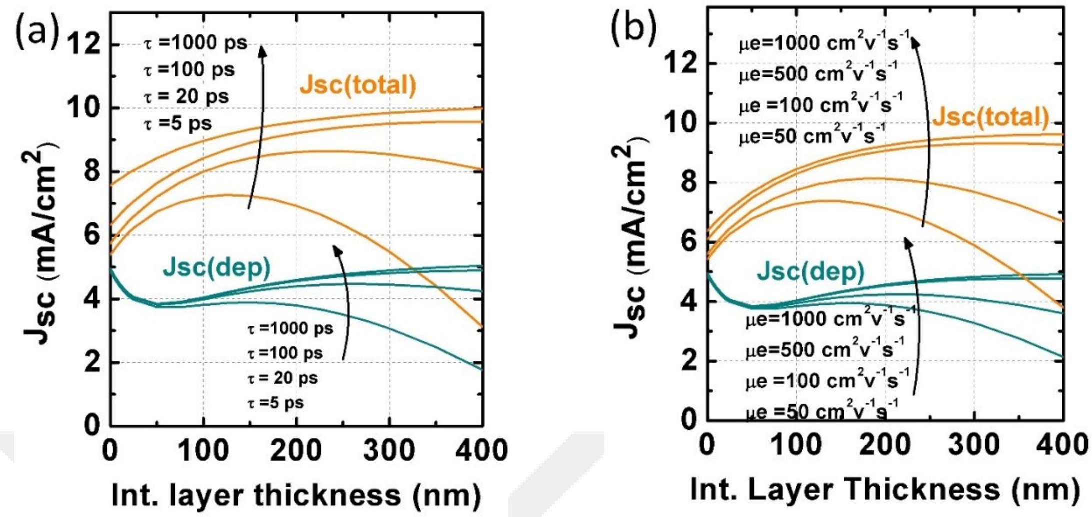

Figure 5.5. Short circuit current density and its amount generated in the depletion region variation as a function of intrinsiic layer thickness under varying carrier (a) lifetime and (b) mobility

The reason for the current drop can be explained as follows. Increasing the intrinsic layer thickness decreases the field across the depletion region. It should be noted that there is an important factor as the first term of the equations (5.6), (5.7) and (5.8); the ratio of the depletion thickness with the product of minority carrier mobility and lifetime. When depletion is thicker or the product of minority carrier mobility and lifetime is low, the short circuit current decreases. The physical explanation is that the electric field in the depletion region decreases approximately linearly with intrinsic layer thickness and the diffusion length for both carriers become too low with lower mobility. Overall, carriers that enters the depletion region or the carriers that are generated in depletion region may not be drift across the junction.

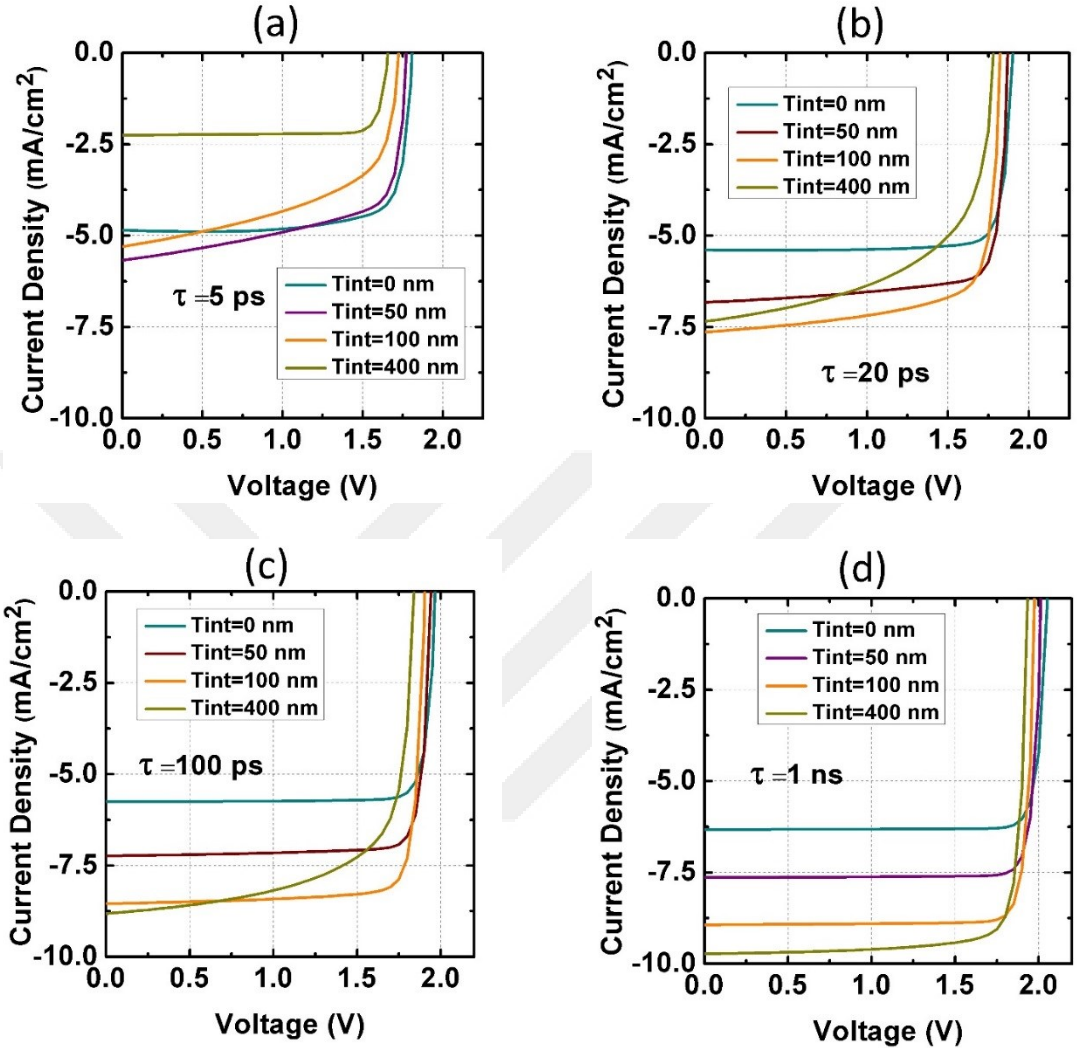

Figure 5.6. I-V plots of the solar cells with varying intrinsic region thickness under (a)τ_e=5ps, (b)τ_e=20ps,(c)τ_e=100ps and (d)τ_e=1ns (Intrinsic layer thickness increases in the direction of the arrows.)

The Current-voltage (I-V) characteristics of the p-i-n cells are shown under varying T_{int} as a function of electron minority carrier lifetime (τ_e) of 5, 20, 100 and 1000ps in Figure 5.6(a), (b), (c) and (d) respectively. The open circuit voltage (V_{oc}) drops as T_{int} increases for all τ_e's. However, the magnitude of the decrease strongly depends on τ_e. It can be seen from Fig. 5.6d that V_{oc} slightly decreases from 2.16V ($T_{int} = 0$) to 2.04V ($T_{int} = 400nm$) under τ_e of 1ns. Whereas; it sharply decreases from 1.9V ($T_{int} = 0$) to 0.8V ($T_{int} = 400nm$) under τ_e of 5ps as shown in Figure 5.6a.

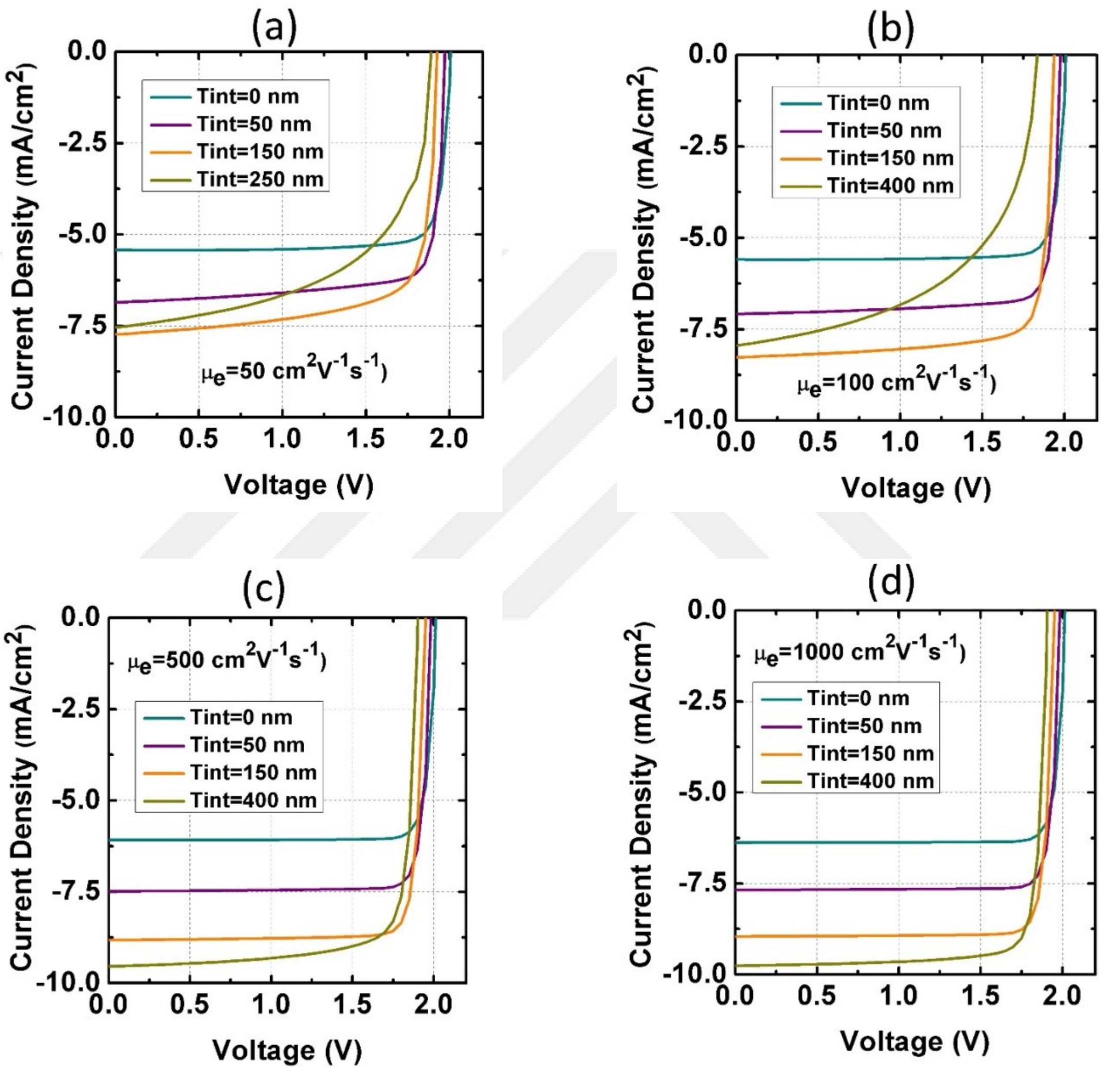

Figure 5.7. I-V plots of the solar cells with varying intrinsic region thickness under (a) μ_e=50 cm2V-1s-1, (b) μ_e=100cm2V-1s-1,(c) μ_e=500cm2V-1s-1 and (d) μ_e = 1000cm2V-1s-1 (Intrinsic layer thickness increases in the direction of the arrows.)

There is a couple of factors responsible for the reduction in V_{oc}. Firstly, the dark current is proportional to the thickness of the depletion region and inversely proportional to the average lifetime as shown in equation (5.10). Thus, increasing depletion thickness or decreasing average carrier mobility decreases V_{oc}. But this drop can be negligibly small. The major reason for the sharp drop is the decrease in the electric field with increasing operating voltage. This decrease in drift velocity especially with shorter τ_e eventually results in an increase of carrier recombination in the depletion region.

Figure 5.7(a), (b), (c) and (d) shows the I-V characteristics under varying electron mobility of 50, 100, 500 and 1000 cm^{2}V^{-1}s^{-1} respectively. From Figure 5.7d, it can be seen that V_{oc} decreases slowly from 2.02V ($T_{int} = 0$) to 1.91V ($T_{int} = 400nm$) under μ_e of 1000 cm^{2}V^{-1}s^{-1}. Whereas, it decreases sharply from 2.02V ($T_{int} = 0$) to 0.95V ($T_{int} = 400nm$) with a μ_e of 50 cm^{2}V^{-1}s^{-1} as shown in Figure 5.6a. The results depicted in Figure 5.6 and 5.7 show similar I-V characteristics since both of the parameters (τ_e and μ_e) affects the diffusion length.

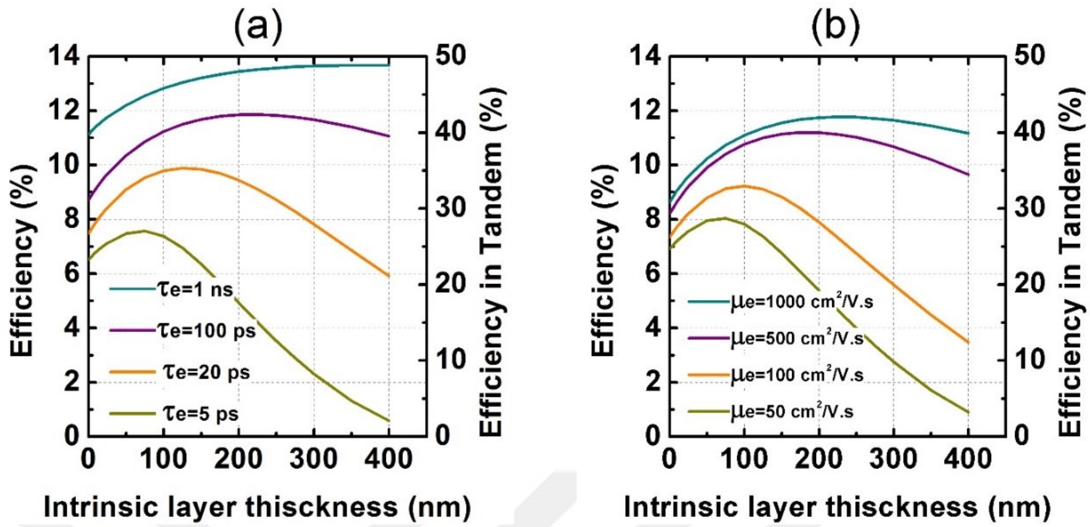

Figure 5.8. Single and tandem cell efficiency as a function of intrinsic layer thickness under varying (a)electron minority carrier lifetime and (b)carrier mobility

Figure 5.8 depicts the single and tandem cell efficiencies of the simulated 2.3 eV solar cells with varying intrinsic layer thickness as a function of (a) minority carrier lifetime and (b) mobility. Efficiency in tandem cell is estimated by considering the efficiency of the device with respect to the absorbed part of the spectrum. Since this wide bandgap cell would be designed as a window cell it will be transparent for photons with energy less than 2.3 eV. It is noteworthy that in all cases efficiency of the solar cell can be increased with a optimum thickness of intrinsic region. Such thickness is relatively higher for high quality cells. For instance, ~200nm thick intrinsic region is optimum for the cell with $\tau_e = 100\ ps$ and $\mu_e = 444$ cm^{2}V^{-1}s^{-1}. Although efficiency variation with carrier lifetime or mobility seems to be similar (Fig. 5.8 (a) and (b)), carrier lifetime variation results in relatively higher efficiency variation under default parameters $\tau_e = 50ps$ and $\mu_e \sim 444$ $cm^2V^{-1}s^{-1}$ which is obvious especially when the thickness of the intrinsic region is relatively thin ($T_{int} < 50nm$). The maximum efficiency obtained under carrier life time variation with T_{int} of 400nm is around 14% for a single cell and 50% for a tandem cell. This is around 12% for a single cell and 42% for a tandem cell with carrier mobility variation with T_{int} of 225nm. From the Figure 5.8, it can be seen that the pn junction solar cell efficiency can be increased by 36% if a p-i-n design with appropriate intrinsic layer thickness is used.

5.3.4 Conclusions

The simulation of a 2.3 eV InGaN p-i-n homojunction solar cell was performed with varying carrier mobility and lifetime to study the effects of material properties on the optimum intrinsic region thickness. The fill factor and open circuit voltage of the cells have been shown to decrease as the intrinsic layer thickness increased, however the short circuit current can be boosted to enhance the overall efficiency. The efficiency can be enhanced as much as 36% over the pn junction design by optimizing the intrinsic layer thickness of the p-i-n design. Furthermore, the intrinsic layer thickness has shown to be critical when carrier mobility and lifetime is relatively low. The efficiency decreases dramatically with further increase in the intrinsic region above the optimal thickness of the particular cell.

However, the realization of these devices faces some material growth challenges. Firstly, undoped GaN crystal shows n-type conduction ($<1x10^{16}$) due to the presence of Ga vacancies and native negative ions [134,135]. The unintentional doping background concentration is higher as the Indium content increases in InGaN films. Thus, obtaining an intrinsic region with very low carrier concentration is still challenging. Secondly, there is a lack of native substrates for the growth of films with low density of dislocations.

Currently InGaN materials are grown on GaN on sapphire/silicon templates, however the lattice mismatch between GaN and InN is quite high which results in nucleation of dislocations while growing thick InGaN films with high In content. Keeping the technological limitations in mind, these results are expected to improve the understanding the design issues of InGaN p-i-n solar cells.

5.4 Experimental: InGaN solar cells with TJs

5.4.1 InGaN solar cell with a polarization engineered InGaN TJ

As it is discussed above the main challenge in achieving high efficiency InGaN solar cells are the limitations in the active region thickness and In- content of the InGaN layer. Also, it can be seen from the solar cell characteristics that the EQE is very low for the wavelength range near GaN band energy. This is due to the absorption of incident UV light in the top GaN layer. One can argue that GaN layer can be kept thin to reduce the absorbed light. However, decreasing pGaN thickness increases the sheet resistance of the top p-GaN layer which works as current spreading layer. Low hole mobility and concentration in a pGaN layer requires thick pGaN layer. In this work, we have used a tunnel junction layer to convert resistive pGaN layer to conductive nGaN layer which enables the growth of a Nitride solar cell very thin top GaN layer for current spreading, thus transporting UV light to the InGaN active region below.

The epitaxial design of the InGaN/GaN heterojunction solar cell with a TJ is shown in Fig. 5.9. The device was grown using Veeco Gen 930 N_2 PAMBE system equipped with elemental sources for Ga, In, Si, and Mg, and a Veeco uni-bulb N_2 plasma source with a base pressure of 5×10^{-11} Torr. A nominal growth rate of 430 nm/hr was used throughout the growth of all samples under a system pressure of 2.5 x 10^{-5} Torr at a radio-frequency plasma power of 350 W.

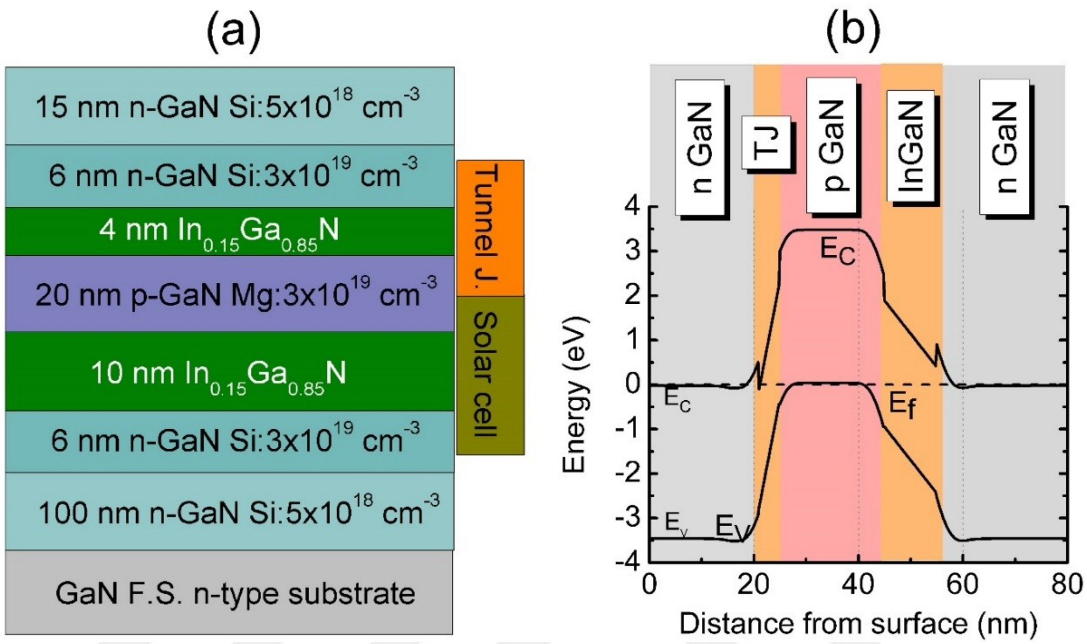

Figure 5.9: (a) The epitaxial stack of the InGaN/GaN heterojunction solar cell with a polarization engineered InGaN/GaN TJ on top. (b) Corresponding energy-band diagram of the device.

The growth was initiated with 100 nm GaN with Si doping of 5 x 10^{18} cm^{-3} on free standing GaN subtrates (dislocation density ~3 x 10^{7} cm^{-2}, Si doping ~ 3 x 10^{18} cm^{-3}, obtained from Saint-Gobain, France), followed by 6 nm of n+ GaN with Si doping of 3 x 10^{19} cm^{-3} at a growth temperature of 700 ºC under Ga-rich conditions. Then 10 nm undoped InGaN layer was grown at a growth temperature of 630 ºC with In excess metal present on the growth surface. A 20 nm Mg:GaN with a doping of 3 x 10^{19} cm^{-3} follows at a substrate temperature of 680 ºC with In metal riding the surface. The InGaN-based tunneling layer was formed with undoped 4 nm $In_{0.15}Ga_{0.85}N$ followed by 6 nm n++ GaN with Si doping of 3 x 10^{19} cm^{-3}. The top spreading layer was formed by 15 nm n GaN with Si doping of 5 x 10^{18} cm^{-3} at a substrate temperature of 700 ^{o}C.

The device with ~143 X 143 μm^2 mesa area and Al/Ni/Au electrode on top and bottom n-type ohmic contacts was fabricated using standard lithography techniques. It should be noted that unlike traditional nitride solar cells, this device doesn't have a thin metal layer or a semitransparent conductive oxide layer as current spreading layer on top of the device. The top electrode covers only ~10% of the device area, thus light is directly incident on the semiconductor surface without such absorbing layers. This is crucial especially for the transmittance of short wavelength photons to the active region since traditional conductive oxide layers absorb those photons.

It can be seen from Fig. 5.9(a) that the device has only ~41nm GaN and 4nm InGaN on top of the active region which makes the device unique compared to traditional solar cells with thick p-GaN layer on top (~100-500 nm). One can mention that 10 nm InGaN layer is very thin compared to the absorption length (~100 nm). However the idea behind this device is that, if it is shown to work with a proper TJ, it would be possible to cascade this device with identical active regions to extend the active region thickness to extend the active region for full absorption which is discussed in the next section.

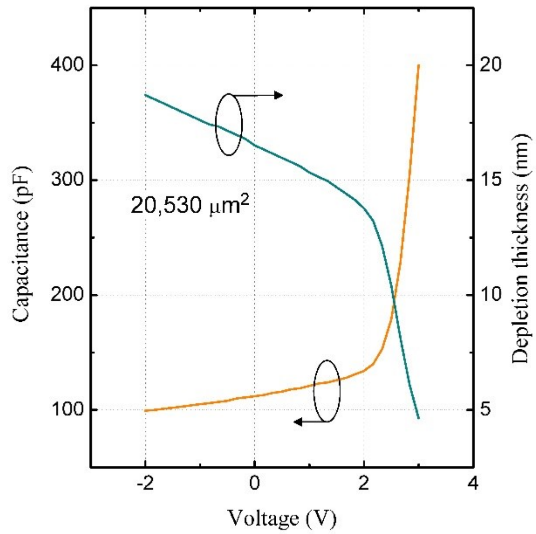

Figure 5.10: The Capacitance-voltage measurement of the device at 100 kHz showing a depletion thickness of 17 nm at 0 V.

Fig. 5.10 shows the quasi-static capacitance-voltage (C-V) characteristics of the TJ solar cell measured at 100 kHz. The zero bias energy band diagram (Fig.5.9b) calculated using a self-consistant1-D Poisson-Schrodinger solver that incorporates polarization charges (BandEng) indicates that theoretical total depletion thickness across the device is ~20 nm. The extracted depletion thickness of from the C-V data is 17 nm which is very close to the theoretical value, thus confirming the doping levels in the device epitaxy.

Room temperature EQE measurement was performed by Zhen Zhang at the Ohio State University. The light output of a 1000 W Xe-lamp source was dispersed through a 0.25 m monochromator to provide monochromatic optical excitation from 2.0 eV to 3.6 eV in 0.02 eV increments focused on the sample in a rectangular 2 mm x 5mm spot. The photon flux at each wavelength was measured using a calibrated thermopile. With zero bias applied on the diode, the photocurrent generated at each wavelength was collected by electrometer, and the EQE was calculated and plotted as a function of light energy. Since the excitation spot is much larger than the device area, the absolute value of the EQE might be overestimated. Nevertheless, the measurement showed encouraging results especially for an MBE-grown solar cell.

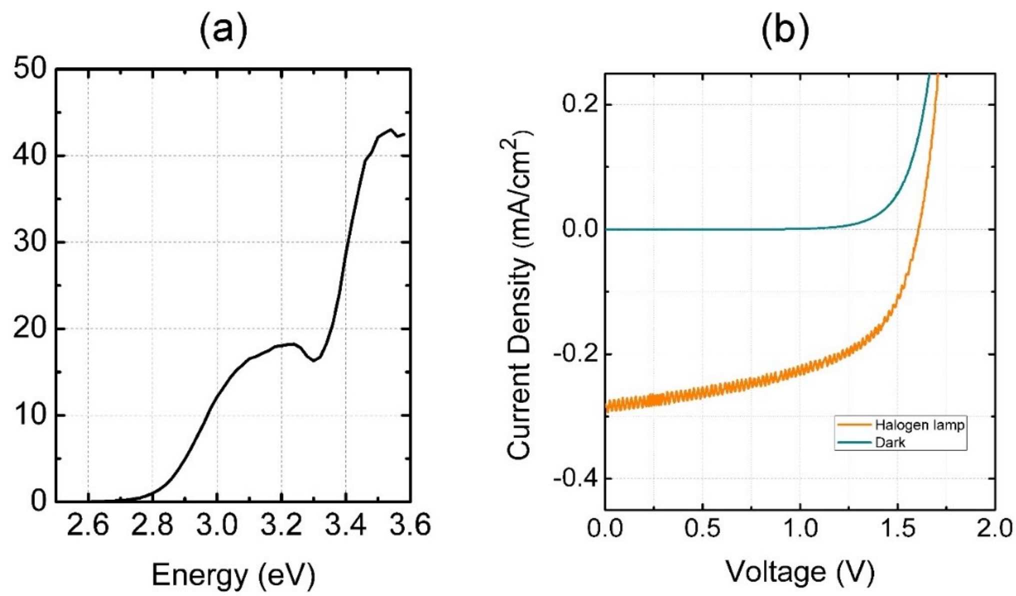

Figure 5.11 (a) The external quantum efficiency (EQE) measurement of the device and (b) the device I-V under no light and halogen light of the probe station.

It is noteworthy that the EQE peak ratio of GaN to InGaN is ~2.5 which is quite encouraging since InGaN layer is only 10 nm and is able to contribute considerably to the overall efficiency of the device. This is attributed to the high crystal quality of the thin InGaN layer present in the device. A series of samples with thicker InGaN layers were also investigated but found to be very leaky probably due to lattice relaxation and nucleation of extended defects which acts as shunt paths for vertical leakage. [136] Here the reported device is ~143 x 143 μm^2 mesa area and larger devices were found with higher leakage. This phenomenon is quite complicated and probably a result of conduction through defects in MBE-grown NPN structures. Due to this problem, the dimension of the reported device is relatively small compared to traditional (~mm^2) devices.

I-V measurement of the device under standard solar spectrum couldn't be performed for the same reason. The measurement probe station was set up for large contact pads & devices. Due to these limitations the device I-V could only be measured in probe stations with micro probes. Our probe station has halogen light source which can be used to excite the device with an arbitrary photon flux. I-V measurement under these conditions was shown in Fig. 5.11b. It can be seen that device has some shut leakage which results a fill factor of 52%. This is an intrinsic problem of MBE-grown diodes especially LEDs & solar cells.

While there are fundamental limitations in MBE-grown solar cells, these results demonstrate the first Nitride solar cell with a thin top spreading layer using an InGaN TJ.

5.4.2 Investigation of cascading dual junction InGaN solar cells

As discussed in the previous section, cascading multiple active regions of either identical or varying bandgap of InGaN is the fundamental motivation behind this study. Since conventional InGaN solar cells can only incorporate limited thickness of InGaN layer due to the large lattice mismatch between GaN and InGaN, full absorption of the corresponding solar spectrum is not possible. To the best of our knowledge, there has been no report of an InGaN solar cell with high (>15%) In content and near full absorption.

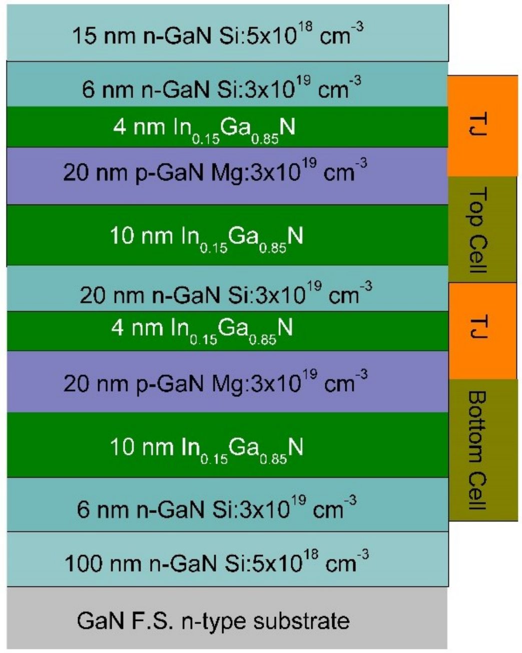

Figure 5.12: The epitaxial design of the dual junction solar cell with identical active regions.

The epitaxial design of the double active region device is shown in Fig. 5.12a. It is simply the dual junction version of the single cell device characterized in the previous section. PA-MBE was used to grow the structure under similar growth conditions as mentioned in previous section. It can be seen that the structure has two InGaN TJs, one to interconnect the top and bottom cell and other to invert the contact from p- to n-type.

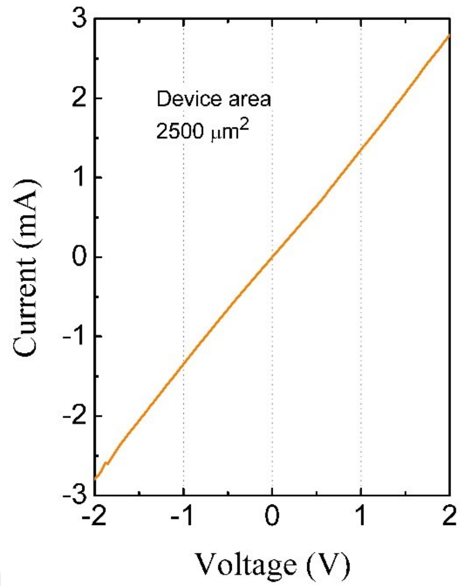

Figure 5.13: I-V measurement of the dual junction solar cell structure.

The device was fabricated with Al/Ni/Au metal contacts for both terminals and various device mesa area. I-V measurement was performed on those devices with varying mesa area. All the samples were found to have large shut leakage, thus no rectification was observed. A typical I-V is shown for a 50 x50 μm^2 structure in Fig. 5.13. It can be seen that the structure is completely shorted by shunt leakage paths.

The bottom cell works properly with NPN geometry. The layers grown on top of this cell leads to additional shunt paths. Even if the top cell is shorted by nucleation of additional defects or some other structural problems, it is expected to observe the I-V of the bottom cell with more resistive conduction upon measuring the whole structure which was the case for the cascaded LEDs [see section 3.4.4]. Thus, it can be concluded that the presence of thicker InGaN layer in cascaded solar cell device is responsible for this observation. The identification of this mechanism needs detailed further characterization which is ongoing and part of the future work.

In conclusion, unlike the single active region solar cell with TJ, the dual junction solar cell structures showed large leakage which dominates the device characteristics. We speculate that shunt paths related with thick InGaN active region is responsible for this observation. MBE growth optimization or application of other growth techniques, such as MOCVD might overcome this detrimental device problem.

Chapter 6

Conclusions and Future Work

6.1 Conclusions

In this thesis, various approaches were investigated to overcome long-lasting roadblocks of high efficiency Nitride light emitting diodes and solar cells using MBE growth.

The N-polar LED with green emission was demonstrated for the first time. After developing and optimizing the N-polar InGaN growth under N-rich conditions, LEDs were grown to investigate electron overflow mechanism for N-polar LEDs. Intrinsic electron blocking property of these LEDs was demonstrated experimentally. The devices emitted green ($\lambda \sim 535\text{-}550$ nm) light with a low turn-on voltage (~2.3 V). Relatively flat EQE curve was achieved up to 400 A/cm^2 from an EBL free DQW N-polar LED. However, overall efficiency of N-polar LEDs was shown to be lower than Ga-polar counterpart which may be related with inferior optical properties of N-polar InGaN. Thus, in the rest of the thesis, Ga-polar orientation was investigated. Modelling of Cascaded multiple nitride LEDs was shown to overcome efficiency droop by supplying electrical input power via increased voltage rather than current as in conventional LEDs. GaN PN diodes were successfully cascaded up to 4-junctions using GdN TJs. Then, the growth of cascaded LEDs was developed to achieve cascading of optically active junctions. World's first 3-junction blue LED was demonstrated with forward voltage operation at 9.1 V under 10 A/cm^2 which was in excellent agreement with an ideal device. The device was characterized to verify the contribution of the top LED to the overall optical output. However, the contribution of individual active regions was found to be non-uniform which may be related with intrinsic issues with MBE growth of emitters and needs further investigation.

GaN tunnel homo-junctions were investigated using very high Si and Mg doping. World's first Esaki-type GaN diodes were demonstrated with repeatable negative differential resistance with peak forward tunneling current of 350 A/cm^2. The junctions were then integrated with a conventional PN diode to form NPN structure for further analysis of Zener characteristics of the GaN TJs. The diode was shown to operate at 3 V under 20 A/cm^2 and reached a highest reported maximum operating current of 150 kA/cm^2 at forward voltage of 7.6 V with a total differential resistance of 9 x 10^{-3} ohm.cm^2 and 1 x 10^{-5} ohm.cm^2, respectively. Then these GaN TJs were integrated with GaN LEDs to fabricate p-side down LEDs. However, the LEDs were found have low emission power and high shunt leakage when grown on heavy SI/Mg doped GaN tunnel junctions, probably due to nucleation of defects under heavy Si/Mg doping.

In the last part, both simulation and experimental work on Nitride solar cells is shown. The simulation of the 2.3 eV InGaN pin homojunction solar cell was performed under varying carrier mobility and lifetime to study the effects of material properties on the optimum intrinsic region thickness. The efficiency can be enhanced as much as 36% over the PN junction design by optimizing the intrinsic layer thickness of PIN design.

Also, the intrinsic layer thickness has shown to be critical when carrier mobility and lifetime is relatively low. In the experimental part, an InGaN TJ was integrated with an InGaN/GaN heterojunction solar cell to convert top resistive p-GaN layer with conductive n-GaN. While there was high shut leakage and some limitations in MBE grown solar cells, the device demonstrates the first Nitride solar cell with a thin top n-type spreading layer using an InGaN TJ.

6.2 Future Work

The research was carried out using PA-MBE growth of cascaded LEDs, GaN TJs, p-down LEDs and TJ-solar cells. We have successfully demonstrated new devices experimentally for the first time and also achieved record high performance from some of those devices. However, using a single growth system (MBE), the performance of those complicated devices are limited. The opportunities to extend this work are discussed in the following.

6.2.1 MOCVD and MBE hybrid growth for a cascaded LED

High efficiency cascade LED requires low resistance TJs and stacking of high efficiency emitters. Low- resistance GaN/InGaN/GaN, GaN/GdN/GaN and GaN/GaN tunnel junctions have been established by MBE growth utilizing sharp doping profiles and high doping concentration of Si and Mg. However, the efficiency of MOCVD grown LEDs far exceeds the MBE grown LEDs. A hybrid growth of MBE and MOCVD may achieve high brightness cascaded LEDs as depicted in Figure 6.1. After the MOCVD growth of p-up geometry conventional LED, the sample needs to be annealed to activate the top p-GaN layer. Then it can be loaded in MBE for the growth of a TJ with n-GaN as the top epilayer. The sample then can be loaded in to MOCVD reactor for the growth of a 2^{nd} emitter junction. These MOCVD active LEDs can be identical to overcome efficiency droop as well as emit in various wavelength to realize multi-color or white emission.

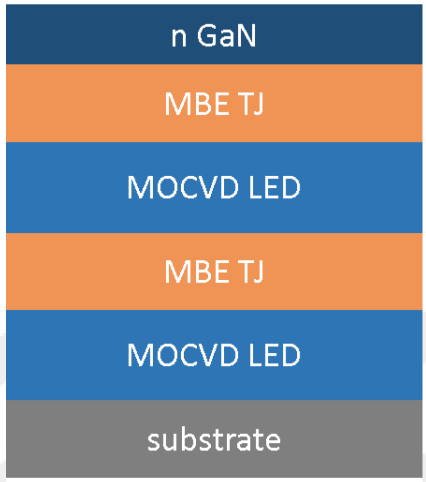

Figure 6.1: Schematic of a cascaded LED device using hybrid MBE and MOCVD growth techniques.

6.2.1 MOCVD and MBE hybrid growth of a p-down LED

6.2.1 MOCVD and MBE hybrid growth of a p-down LED

As discussed in chapter 5, fundamental limitation in efficiency of nitride solar cells is the limitation of growth thickness of high quality InGaN layer. Similar hybrid growth of MOCVD and MBE can also be applied to grow tandem solar cells either with identical active regions or to cascade active regions from various bandgap. The current match criteria of each cell can be controlled by the number of the periods of a specific active region. For example, a GaN top cell can be current matched with triple active regions of 2.8 eV InGaN cells. Since GaN TJs shown in chapter 4 is capable of operating under forward bias, it can readily be used in this device. Such device is very promising for future high efficiency solar cells as a window junction in a (III-As/P) tandem solar cell.

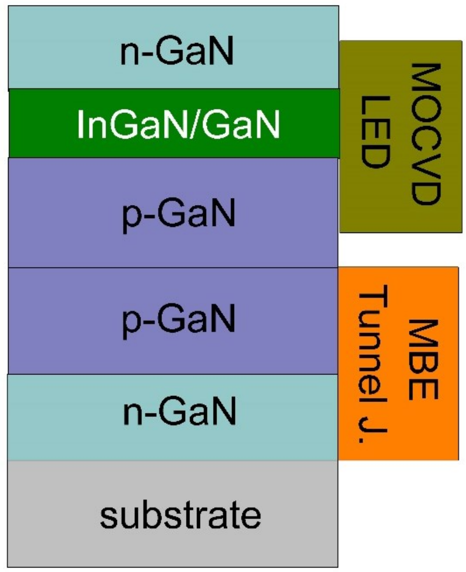

Figure 6.2: MBE & MOCVD hybrid growth of a p-down LED.

6.2.3 MOCVD and MBE hybrid growth for a cascaded solar cell

As discussed in chapter 5, fundamental limitation in efficiency of nitride solar cells is the limitation of growth thickness of high quality InGaN layer. Similar hybrid growth of MOCVD and MBE can also be applied to grow tandem solar cells either with identical active regions or to cascade active regions from various bandgap. The current match criteria of each cell can be controlled by the number of the periods of a specific active region. For example, a GaN top cell can be current matched with triple active regions of 2.8 eV InGaN cells. Since GaN TJs shown in chapter 4 is capable of operating under forward bias, it can readily be used in this device. Such device is very promising for future high efficiency solar cells as a window junction in a (III-As/P) tandem solar cell.

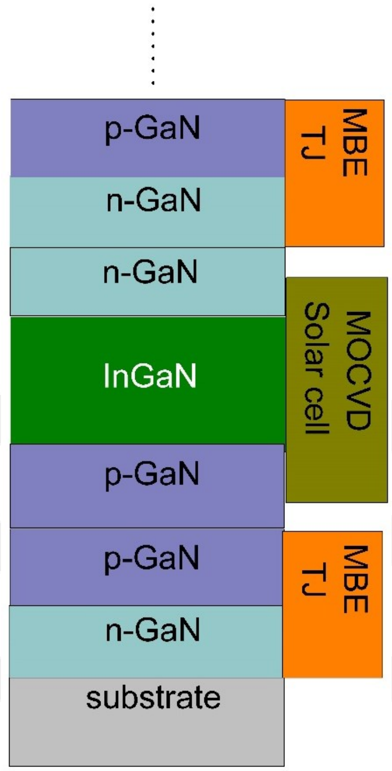

Figure 6.3: MOCVD & MBE hybrid growth of a nitride tandem solar cell.

6.2.4 Investigation of Band-tail states in Heavy Si & Mg Doped GaN

As discussed in chapter 4, the existence of band-tail states were hypothesized to enable boost the tunneling current and forward tunneling in the stand-alone GaN tunnel junctions. Further experiments on the stand-alone TJs or bulk heavy Mg or Si doped GaN can be performed to characterize band-tail states (if there is any).

Internal photon emission (IPE) measurements can be performed on the stand alone TJ devices which can measure the electrical current under varying wavelength of the photon excitation. Analyzing the photocurrent versus photon energy, it may be possible to characterize band-tail states.

PL or absorption spectra of heavy Si or Mg doped bulk GaN samples can be analyzed. If there are band-tail states, one may expect to see higher intensity from long wavelength emission spectrum. The absorption spectrum can reveal the change in the absorption edge which is a function of band-tail states.

Bibliography

1) S. Nakamura and G. Fasol, The Blue Laser Diode (Springer Verlag, 1997).

2) F. Bernardini, V. Fiorentini and D. Vanderbilt, Phys. Rev. B 56, R10024 (1997).

3) F. Bernardini and V. Fiorentini, Phys. Stat. Sol. (b) 216, 391, 1999.

4) Ibach and H. Lueth. Solid-State Physics. Springer Verlag, 2003.

5) Jonas Lähnemann, PhD dissertation Humboldt-Universität zu Berlin, 2013.

6) H. P. Maruska, J. J. Tietjen, Appl. Phys. Lett. 15, 327 (1969).

7) J. I. Pankove, E. A. Miller, J. E. Berkeyheiser, RCA Review 32, 383 (1971).

8) H. P. Maruska, L. J. Anderson, D. A. Stevenson, J. Electrochem. Soc., 121, 1202 (1974)

9) H. Amano, N. Sawaki, I. Akasaki, Y. Toyoda, Appl. Phys. Lett., 48 (1986) 353—355

10) 1991: S. Nakamura et al., Appl. Phys. Lett., 58 (1991) 2021—2023

11) I. Akasaki, H. Amano, M. Kito, and K. Hiramatsu, Journal of Luminescence, 48-49 Jan-Feb p.666 1991

12) S. Nakamura et al., Jpn. J. Appl. Phys., 31 (1992) L139—L142

13) S. Nakamura et al., Jpn. J. Appl. Phys., 31 (1992) L1457—L1459

14) S. Nakamura et al., Appl. Phys. Lett., 64 (1994) 1687—1689

15) US DOE Solid state lightening research and development multi-year program plan April 2014.

16) D Zhu, D J Wallis and C J Humphreys, Rep. Prog. Phys. 76 (2013) 106501

17) Lester et al., Appl. Phys. Lett., 66, (1995) 1249

18) F. Scholz, A. Sohmer, J. Off, V. Syganow, and H. Lakner, Mater. Sci. Eng. B50, 238-244 (1997).

19) V. Fiorentini, F.Bernardini, F. Della, A. Sala, P. Di Carlo, and Lugli, Phys. Rev. B 60, 8849-8858 (1999).

20) Chichibu, Nakamura et al., Appl. Phys. Lett., 69 (1996) 4188; Nakamura, Science, 281 (1998) 956.

21) www.superiorlighting.com/LED_Lamp_Components_Explained_s/2476.htm

22) S. Ling T. Lu, S. Chang, J. Chen, H. Kuo and S. Wang, Appl. Phy. Lett. 96, 231101 (2010),

23) K. J. Vampola, M. Iza, S. Keller, S. P. DenBaars and S. Nakamura, Apll. Phy. Let. 94, 061116 (2009)

24) D. F. Feezel, M. C. Schmidt, S. P. DenBars and S. Nakamura MRS bulletin 34, 318-323 (2009).

25) Y. C. Shen, G. O. Mueller, S. Wanabe, N. F. gardner, A. Munkholm and M. R. Krames, Appl. Phys. Lett. 91, 141101 (2007).

26) M. F. Schubert, S. Chhajed, J. K. Kim, E. F. Schubert, D. D. Koleske, M. H. Crawford, Appl. Phys. Lett. 91, 231114 (2007).

27) I. V. Rozhansky and D. A. Zakheim, Phys. Status Solidi A 204, 227 (2007).

28) X. Ni, Q. Fan R. Shimada, U. Ozgur and H. Markoc, Appl. Phys. Lett. 93, 171113 (2008).

29) J. P. Liu, J. H. Ryou, R. D. Dupuis, J. Han, G. D. Shen, and H. B. Wang, Appl. Phys. Lett. 93, 021102 (2008).

30) C. H. Wang, C. C. Ke, C. Y. Lee, S. P. Chang, J. C. Li, Z. Y. Li, H. C. Yang, H. C. Kuo, T. C. Lu and C.Wang, Appl. Phys. Lett. 97, 261103 (2010).

31) S. Choi, H. J. Kim, S. Kim, J. Liu, J. Kim, J. Ryou, R. D. Dupuis, A. M. Fischer, and F. A. Ponce, Appl. Phy. Lett. 96, 221105 (2010).

32) C. H. Wang, C. C. Ke, C. Y. Lee, S. P. Chang, W. T. Chang, L. C. Li, Z. Y. Li, H. C. Yang, H. C. Kuo, T. C. Lu, and S. C. Wang, Appl. Phys. Lett. 97, 261103 (2010).

33) S. J. Chang, W. C. Lai, Y. K. Su, J. F. Chen, C. H. Lim, and U. H. Liaw, IEEE J. Sel. Topics Quantum Electron., 8, 278 Mar./Apr. (2002).

34) S.-H. Han, D.-Y Lee, S.-J. Lee, C.-Y. Cho, M.-K Kwon, S. P. Lee, D. Y. Noh, D.-J Kim, and S.-J. Park, Appl. Phys. Lett. 94, 231123 (2009).

35) Richard Stevenson, IEEE Spectrum 47, 3, March (2010).

36) K. Xu and A. Yoshikawa, Appl. Phys. Lett. 83, 251 (2003).

37) H. Naoi, F. Matsuda, T. Araki, A. Suzuki and Y. Nanishi, J. Crys. Growth 269 (2004).

38) D Nath, E. Gur, S. Ringel and Siddharth Rajan,Appl. Phys. Lett. 97, 071903 (2010).

39) S. Rajan, A. Chini, M.H. Wong, J.S. Speck and U.K. Mishra, J. Appl. Phys.102, 044501 (2007).

40) Joshua Abell, Ph.D. Thesis, Boston University, 2008.

41) X.Q. Shen, T. Ide, M. Shimizu and H. Okumura, J. Crys. Growth 237-239 (2002).

42) H. Masui, S. Keller, N. Fellows, N.A. Fichtenbaum, M. Furukawa, S. Nakamura, U.K. Mishra, and S.P. DenBaars, Jpn. J. Appl. Phys. 48 071003 (2009)

43) M. Grundmann, BandEng, Available online: http://www.michaelgrundmann.com.

44) www.lumilog.com

45) P. Perlin, C. Kisielowski, V. Iota, B. A. Weinstein, L. Mattos, N. A. Shaprio, J. Kruger, E. R. Weber, and J. Yang, Appl. Phys. Lett. 73, 2778 (1998).

46) M. Funato, M. Ueda, Y. Kawakami, Y. Narukawa, T. Kosugi, M. Takahashi and T. Mukai, Jpn. J. Appl. Phys. 45, 659 (2006).

47) Y. D. Qi, H. Liang, D. Wang, Z. D. Lu, W. Tang, and K. M. Lau, Appl. Phys. Lett. 86, 101903 (2005).

48) B. L. VanMil, H. Guo, L. J. Hobert, K. Lee, T. H. Myers, T. Liu, and D. Korakadis, J. Vac. Sci. Technol. B 22, 2149 (2004).

49) C. Cheze, M. Sawicka, M. Siekacz, H. Turski, G. Cywiski, J. Smalc-Koziorowska, J. L. Weyher, M. Kryko, B. Uznik, M. Bokowski, and C. Skirbiszewski, Appl. Phys. Lett. 103, 071601 (2013).

50) G. Koblmüller, F. Wu, T. Mates, J. S. Speck, S. Fernández-Garrido and E. Calleja, Appl. Phys. Lett. 91, 221905 (2007).

51) S. V. Ivanov, V. N. Jmerik, T. V. Shubina, S. B. Listoshin, A. M. Mizerov, A. A. Sitnikova, M.-H. Kim, M. Koike, B.-J. Kim, P. S. Kopev, J. Cryst. Growth, 301-302 (2007) 465.

52) H. Chen, R. M. Feenstra, J. E. Northrup, T. Zywietz, J. Neugebauer, and D. W. Greve, J. Vac. Sci. Technol. B 18, 2284 (2000).

53) C. Adelmann, J. Simon, G. Feuilet, N. T. Pelekanos, B. Daudin and G. Fishman, Appl. Phys. Lett. 76, 1570 (2000).

54) D. N. Nath, E. Gur, S. A. Ringel, and S. Rajan, J. Vac. Sci. Technol. B 29, 021206 (2011).

55) V. N. Jmerik, A. M. Mizerov, T. V. Shubina, M. Yagovkina, V. B. Listoshin, A. A. Sitnikova, S. V. Ivanov, M. H. Kim, M. Koike, and B. J. Kim, J. Cryst. Growth 301, 469 (2007).

56) K. Hestroffer, C. Lund, H. Li, S, Keller, J, S. Speck and U, K. Mishra, Phys. Status Solidi B, 1–4 (2016).

57) T. L. Tansley and R. J. Egan, Phys. Rev. B. 45, 10942 (1992).

58) D. Doppalapudi, S. N. Basu, K.F. Ludwig, Jr. and T. D. Moustakas, J. Appl. Phys. 84 No:3 1 August (1988).

59) M. Pophristic, F. H. Long, C. Tran, I. T. Ferguson, and R. F. Karlicek Jr., Appl. Phys. Lett. 73, 3550 (1998).

60) S. Watanabe, N. Yamada, M. Nagashima, Y. Ueki, C. Sasaki, Y. Yamada, T. Taguchi, K. Tadatomo, H. Okagawa, and H. Kudo, Appl. Phys. Lett. 83, 24 (2003).

61) S. Keller, B. P. Keller, M. S. Minsky, J. E. Bowers, U. K. Mishra, S. P. Denbaars, W. Seifert, J. Cryst, Growth, 189/190 (1998) 29.

62) M. S. Minsky, S. B. Fisher, A. C. Abare, J. E. Bowers, E. L. Hu, S. Keller, and S. P. Denbaars, Appl. Phys. Lett. 72, 1066 (1998).

63) S. K. Sun, T. –L. Chiu, S. Keller, G. Wang, M. S. Minsky, S. P. Denbaars, and J. E. Bowers, Appl. Phys. Lett. 71, 425 (1997).

64) T. Li, A. M. Fischer, Q. Y. Wei, F. A. Ponce, T. Detchprohm, and C. Wetzel, Appl. Phys. Lett. 96, 031906 (2010).

65) S. Chichibu, T. Azuhata, T. Sota, S. Nakamura, Appl. Phys. Lett. 70 (1997) 2822.

66) H. Pyu, H. Kim and J. Shim, Appl. Phys. Lett. 95, 081114 (2009).

67) M. H. Kim, M. F. Schubert, Q. Dai, J. K. Kim, E. F. Schubert, J. Piprek, and Y. Park, Appl. Phys. Lett. 91 183507 (2007).

68) 15 J. Lee, X. Li X. Ni, U. Ozgur, H. Markoc, T. Paskova, G. Mulholland, and K. R. Evans, Appl. Phys. Lett.

69) X. Li, X. Ni, H. Y. Liu, F. Zhang, S. Liu, J. Lee, V. Avrutin,U. Ozgur, T. Paskova, G. Mulholland, K. R. Evans, and H. Morkoc, Phys. Status. Solidi C 8, 1560 (2010).

70) X. Li, X. Ni, H. Y. Liu, F. Zhang, S. Liu, J. Lee, V. Avrutin,U. Ozgur, T. Paskova, G. Mulholland, K. R. Evans, and H. Morkoc, Phys. Status. Solidi C 8, 1560 (2010).

71) S. -H. Yen and Y. –K. Kuo, J. Appl. Phys. 103, 103115 (2008).

72) F. Akyol, D. N. Nath, E. Gur, P. S. Park and S. Rajan, Jpn. J. Appl. Phys. 50, 052101 (2011).

73) C. –H. Ko, Y. –K. Su, S. –J. Chang, T. –M. Kuan, C. Chiang, W. –H. Lan, W. –J. Lin, and J. Webb, Jpn. J. Appl. Phys. 41, 2489 (2002).

74) www.silvaco.com

75) M. Zhang, P. Bhattacharya, J.Singh, and J. Hinckley, Appl. Phys. Lett. 95, 201108 (2009).

76) A. Dmitriev and A. Oruzheinikov, J. Appl. Phys. 86, 3241 (1999).

77) S. Krishnamoorty, D. N. Nath, F. Akyol, P. S. Park, M. Esposto, and S. Rajan, Appl. Phys. Lett. 97, 203502 (2010).

78) S. Krishnamoorthy, P. S. Park and S. Rajan, Appl. Phys. Lett. 99, 233504 (2011).

79) M. Funato, M. Ueda, Y. Kawakami, Y. Narukawa, T. Kosugi, M. Takahashi and T. Mukai: Jpn. J. Appl. Phys. 45, 659 (2006).

80) C. Thomidis, A. Y. Nikiforow, T. Xu, and T. D. Moustakas, Phys. Stat. Sol. (c) 5, 2309 (2008).

81) C. A. Schaake, N. A. Fichtenbaum, C. J. Neufeld, S. Keller, S. P. Denbaars, J. S. Speck, and U. K. Mishra, Phys. Stat. Sol. (c) 5, 2963 (2008).

82) M. –K. Kwon, I. –K Park, J. –Y. Kim, J. –O. Kim, B. Kim and S. –J. Park, IEEE Phot. Tech. Lett. 19, 23 (2007).

83) "Cree Sets New Record for White LED Efficiency", Tech-On, April 23, 2012.

84) S. Nakamura, M. Senoh, S. Nagahama, N. Iwasa, T. Yamada, T. Matsushita, Y. Sugimoto and H. Kiyoku, Appl. Phys. Lett., 1996, 69, 4056

85) S. Nakamura, M. Senoh, N. Iwasa, S. Nagahama, T. Yamada, and T. Mukai, Jpn. J. Appl. Phys. 34, L1332 (1995).

86) T. Mukai, H. Marimatsu, and S. Nakamura, Jpn. J. Appl. Phys. 37, L439 (1998).

87) M. J. Cich, R. I. Aldaz, A. Chakraborty, A. David, M. J. Grundman, A. Tyagi, M. Zhang, F. M. Steranka, and M. R. Krames, Appl. Phys. Lett. 201, 223509 (2012).

88) US DOE Solid state lightening research and development multi-year program plan, April 2013.

89) J. Iveland, L. Martinelli, J. Peretti, J. S. Speck, Phys. Rev. Lett. 110, 177406 (2013).

90) F. Akyol, D. N. Nath, S. Krishnamoorthy, P. S. Park and S. Rajan, Appl. Phys. Lett. 100, 111118 (2012).

91) T. F. Kent, J. Yang, L. Yang, M. J. Mills, and R. C. Myers, Appl. Phys. Lett. 100, 152111 (2012).

92) S. Krishnamoorthy, T. F. Kent, J. Yang, P. S. Park, R. C. Myers, and S. Rajan, Nano Lett., 2013, 13, 2570-2575.

93) A. H. Reading, J. J. Richardson, C. C. Pan, S. Nakamura, and S. P. Denbaars, Optics Express A13, vol. 20, no. S1 (2012).

94) T. Takeuchi, G. Hasnain, S. Corzine, M. Hueschen, R. P. Schneider, C. Kocot, M. Blomqvist, Y. Chang, D. Lefforge, M. R. Krames, L. W. Cook, and S. A. Stockman, Jpn. J. Appl. Phys. Part 2 40, L861 (2001).

95) S. –R Jeon, Y. –H Song, H. –J Jang, G. M. Yang, S. W. Hwang, S. J. Son, Appl. Phys. Lett., 78, 3265 (2001).

96) M. J. Grundmann and U. K. Mishra, Phys. Status Solidi C 4, 2830 (2007).

97) J. Simon, Z. Zhang, K. Goodman, H. Xing, T. Kosel, P. Fay, and D. Jena, Phys. Rev. Lett., 103, 026801 (2009).

98) M. F. Shubert, Phys. Rev. B 81, 035303 (2010).

99) Z. –H Zhang, S. T. Tan, Z. Kyaw, Y. Ji, W. Liu, Z. Ju, N. Hasanov, X. W. Sun, and H. V. Demir, Appl. Phys. Lett. 102, 193508 (2013).

100) F. Akyol, S. Krishnamoorthy, Y. Zhang, and S. Rajan, Appl. Phys. Express 8, 082103 (2015).

101) M. Malinverni, D. Martin, and N. Grandjean, Appl. Phys. Lett. 107, 051107 (2015).

102) J. T. Leonard, E. C. Young, B. P. Yonkee, D. A. Cohen, T. Margalith, S. P. DenBaars, J. S. Speck, and S. Nakamura, Appl. Phys. Lett. 107, 091105 (2015).

103) E. J. Tarsa, B. Heying, X. H. Wu, P. Fini, S. P. DenBaars, and J. S. Speck, J. Appl. Phys. 82, 5472 (1997).

104) Skierbiszewski C, Wasilewski Z, Siekacz M, Feduniewicz A, Pastuszka B, Grzegory I, Leszczynski M and Porowski S 2004 Phys. Status Solidi a 201 320.

105) Neugebauer J, Zywietz T K, Scheffler M, Northrup J E, Chen H and Feenstra R M 2003 Phys. Rev. Lett. 70 56101.

106) L. Wang, J. M. L. Figueiredo, C. N. Ironside, and E. Wasige, Trans. Elect. Dev. 58, 2 Feb 2011.

107) L. Wang, J. M. L. Figueiredo, C. N. Ironside, and E. Wasige, Trans. Elect. Dev. 58, 2 Feb 2011.

108) P. V. Mieghem Reviews of modern physics 64.3 (1992): 755.

109) E. O. Kane, Physical Review 131.1 (1963): 79.

110) B. Gunning, J. Lowder, M. Moseley, and W. A. Doolittle, Appl. Phys. Lett. 101, 082106 (2012).

111) G. Parish ; L. M. Watson, G. U. Membreno, and B. D. Nener, Proc. SPIE 5276 (April 2, 2004).

112) www.nrel.gov

113) www.ise.fraunhofer.de/en/press-and-media/press-releases/press-releases-2014.

114) D. J. Friedman, Curr. Opin. Solid State Mater. Sci. 14, 131 (2010).

115) N. G. Toledo, D. J. Friedman, R. M. Farrell, E. E. Perl, C. T. Lin, J. E. Bowers, J. S. Speck, and U. K. Mishra, J. Appl. Phys. 111, 054503 (2012).

116) S. P. Bremner, M. Y. Levy, and C. B. Honsberg, Prog. Photovoltaics 16, 225 (2008).

117) J. F. Muth, J. H. Lee, I. K. Shmagin, R. M. Kolbas, H. C. Casey Jr., B. P. Keller, U. K. Mishra and S. P. DenBaars, Appl. Phys. Lett., Vol. 71, No. 18, 3 November 1997.

118) Xiao-mei Cai, Sheng-wei Zeng, and Bao-ping Zhang, Appl. Phys. Lett. 95, 173504 2009.

119) O. Jani, I. Ferguson, C. Honsberg and S. Kurtz Appl. Phy. Lett. 91 132117 (2007).

120) Z. Q. Li, M. Lestradet, Y. G. Xiao andS. Li, Phys. Status Solidi A 208, No. 4 (2011).

121) C. J. Neufeld, S. C. Cruz, R. M. Farrell, M. Iza, J. R. Lang, S. Keller, S. Nakamura, S. P. DenBaars, J. S. Speck, and U. K. Mishra, Appl. Phys. Lett. 98, 243507 (2011).

122) Matioli et al. Appl. Phys. Lett. 98, 021102 (2011).

123) J. R. Lang, C. J. Neufeld, C. A. Hurni, S. C. Cruz, E. Matioli, U. K. Mishra, and J. S. Speck, Appl. Phys. Lett. 98, 131115 (2011).

124) J. R. Lang, N. G. Young, R. M. Farrell, Y.-R. Wu and J. S. Speck, Appl. Phys. Lett. 101, 181105 (2012).

125) N. G. Young, R. M. Farrell, Y. L. Hu, Y. Terao, M. Iza, S. Keller, S. P. DenBaars, S. Nakamura, and J. S. Speck, Appl. Phys. Lett. 103, 173903 (2013).

126) K. Kumakura, T. Makimoto, N. Kobayashi, T. Hashizume, T. Fukui and H. Hasegawa Appl. Phys. Lett. 86 052105 (2005)

127) T.T. Mnatsakanov, M.E. Levinshtein, L.I. Pmortseva, S.N. Yurkov, G.S. Simin, M.A. Khan Solid-State Electron. 47 (2003) 111–115.

128) L. Hsu, R.E. Jones, S.X. Li, K.M. Yu, W. Walukiewicz J. Appl. Phys. 102 (2007) 073705-1–6.

129) http://www.ioffe.ru/SVA/NSM/Semicond/

130) J. Wu and W. Walukiewicz Superlattices and Microstructures, 34 63-75 (2003).

131) R. Aleksiejunas, M. Sudzius, V. Gudelis, T. Malinauskas, K. Jarasiunas, Q. Fareed, R. Gaska, M.S. Shur, J. Yang, E. Kuokstis and M.A. Khan Phys. Ptat. Sol. (c) 0, No. 7, 2686–2690 (2003).

132) G.F. Brown, J.W. Ager, W. Walukiewicz and J. Wu Solar Energy Materials & Solar Cells 94 (2010) 478-483

133) Jenny Nelson ‘Physics of Solar Cells’ p.132,222,223

134) K. Saarinen, J. Nissila, J. Oila, V. Ranki, M. Hakala, M. J. Puska, P. Hautojarvi, J. Likonen, T. Suski, I. Grzegory, B. Lucznik and S. Porowski Physica B 273 (1999) 33-38

135) Cree: www.cree.com

136) X.A. Caoa,, J.A. Teetsova , F. Shahedipour-Sandvikb , S.D. Arthura, Journal of Crystal Growth 264 (2004) 172–177.